学位論文

Fabrication of Nanometer-Scale T-Shaped Quantum Wires and Their Optical Properties

（ナノメートル寸法のT型量子細線の作製と光学特性）

平成8年 12月

Takao Someya

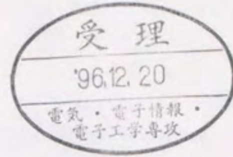

Fabrication of Nanometer-Scale T-Shaped Quantum Wires and Their Optical Properties

（ナノメートル寸法のＴ型量子細線の作製と光学特性）

A Thesis Presented to the Graduate School
of the University of Tokyo
in Partial Fulfillment of the Requirements
for the Degree of Doctor of Philosophy
in Electronic Engineering

by

Takao Someya

December 20, 1996

Dissertation Supervisor

Professor Hiroyuki Sakaki

Acknowledgments

This thesis presents a part of research work carried out at Research Center for Advanced Science and Technology and Institute of Industrial Science, University of Tokyo, under the direction of Professor H. Sakaki, while the author was a graduate student of the Department of Electronic Engineering, University of Tokyo, from April 1994 to March 1997.

The author wishes to express his sincere gratitude for the guidance and the encouragement received from the dissertation supervisor Professor H. Sakaki, Research Center for Advanced Science and Technology, University of Tokyo. This work could not have been accomplished without his invaluable supports.

The author acknowledges Professor H. Akiyama (University of Tokyo) for his enjoyable collaborations and plentiful efforts. The present work has been carried out with the help of his invaluable supports and fruitful discussions.

It is also his great pleasure to acknowledge Professor Y. Arakawa (University of Tokyo), Professor M. Gonokami (University of Tokyo), Professor S. Fukatsu (University of Tokyo), and Professor T. Takahashi (University of Tokyo) for stimulating discussions and constant encouragements.

Thanks are due to Dr. K. Wada (NTT LSI Laboratory) for cathodoluminescence measurement and discussions.

The author would like to thank all members in Sakaki laboratory, Arakawa laboratory, and Shiraki laboratory; the author thanks Professor J. Motohisa (Hokkaido University), Dr. Y. Kadoya (Hiroshima University), and Dr. Y. Ohno (Tohoku University) for supplying the in situ cleavage tools and discussions. The author is indebted to Dr. H. Noge (Hamamatsu Photonics), Dr. S. Koshiba (JST), Dr. I. Tanaka (JST), Dr. I. Kamiya (JST), Mr. T. Noda, Mr. Y. Nakamura (JST), Mr. G. Yusa, and Mr. T. Yoshida (Asahi Kasei) for their technical supports to maintain the MBE system and discussions

discussions in the experiment. Dr. H. Sugawara and Ms. M. Yamauchi (Mathematical Systems Institute) are greatly acknowledged for their theoretical contribution to the present study. The author is grateful to the technical staffs; Professor T. Matsusue (Chiba University), Dr. Y. Nagamune (Electrotechinical Laboratory), Mr. M. Yoshita. Thanks are due to Dr. T. Arakawa, Dr. K. Tanaka, Dr. T. Inoshita (JST), Dr. H. Noguchi (Sony), Dr. R. Sasagawa (Fujitsu), Dr. S. Tsujino (JST), Mr. M. Nishioka, Mr. S. Ishida, Mr. M. Narihiro, Mr. H. Nakajima, and Miss M. Matsuya for their encouragements.

The fellowship was generously supplied by the Japan Society for the Promotion of Science from April 1995 to March 1998. This work was partly supported by a Grant-in-Aid from the Ministry of Education, Science, Sports, and Culture, Japan.

Contents

Acknowledgments i

1 Introduction 1
- 1.1 Backgrounds 1
- 1.2 Objectives 3
- 1.3 Synopses of chapters 4

2 Fabrication of T-shaped quantum wires 8
- 2.1 Introduction 8
- 2.2 T-shaped quantum wires 9
- 2.3 Cleaved-edge overgrowth method 11
- 2.4 MBE growth of InGaAs on (110) 17
- 2.5 Summary 22

3 Spatially-resolved photoluminescence 25
- 3.1 Introduction 25
- 3.2 Characteriztion by spatially-resolved photoluminescence 26
- 3.3 Structure dependence of energy levels 36
- 3.4 Exciton binding energy 45
- 3.5 T-shaped InGaAs quantum wires 52
- 3.6 Summary 56

4 Polarization properties and oscillator strength 60
4.1 Introduction . . . 60
4.2 Optical anisotropy . . . 61
4.3 Structure dependence of optical anisotropy . . . 70
4.4 Oscillator strength . . . 75
4.5 Summary . . . 83

5 Magneto-photoluminesce 88
5.1 Introduction . . . 88
5.2 Lateral size of one-dimensional excitons . . . 89
5.3 Shape of one-dimensional excitons . . . 98
5.4 Summary . . . 105

6 Summary and conclusion 108
6.1 Summary . . . 108
6.2 Prospects in the future . . . 109

Appendix 110
A Sample list . . . 110
B Calculated energy levels in quantum wells . . . 111
C Optical anisotropy in quantum wells . . . 116
D Effective mass equation under a magnetic field . . . 122

Publication list 126

Chapter 1

Introduction

1.1 Backgrounds

Research on semiconductor superlattices and heterostructures was initiated with a proposal by Esaki and Tsu in 1969-1970 [1,2]. With the advancement of such fine epitaxial growth technologies as molecular beam epitaxy (MBE) and metal organic chemical vapor deposition (MOCVD), it becomes possible to confine electrons in ultra-thin films of semiconductors whose thicknesses are comparable to de Broglie wavelengths λ_e of electrons (~10 nm). In such structures, electron motion perpendicular to the layer is quantized, while electron motion within the layer remains free. Electrons confined in heterostrucutres show a variety of unique properties which have never been observed in bulk semiconductors. Transport properties of two-dimensional electron gases have been exploited to invent such novel devices as high-mobility transistors [3] and resonant tunneling diodes [4,5].

Two-dimensional carriers confined in quantum wells also give rise to various new optical properties. Optical absorption shows step-like density of states with strong exciton resonance, which can be observed even at room temperature [6–10]. In addition, large optical nonlinearity [11,12] and quantum-confined Stark effect (QCSE) [13–15] should be noted. These characteristics have been exploited to create such advanced optical devices as quantum well lasers [16,17], intersubband photodetectors [18,19], and optical modulators [20].

These activities on quantum effects were expanded into the study of semiconductor quantum wires, which was initiated by the proposal by Sakaki [21]. Quantum wires

are ultrafine semiconductor wires whose cross sectional dimensions are comparable to de Broglie wavelengths of electrons. In such wires, electron motions are allowed only along the wires and electron motions in the other two directions are quantized. It was theoretically predicted by Sakaki in 1980 that the ionized impurity scattering of electrons in quantum wires can be drastically suppressed [21]. This effect would lead to the ultrafast FET devices and new ballistic electron devices.

In contrast, the study of optical properties of quantum wires is motivated by two expectations. First, the concentrated electronic density of states should make optical transition highly efficient, which would lead to high differential gain in semiconductor laser [22]. Second, the Coulomb interaction should be very effective in quantum wires and create excitons with large binding energy and enhanced optical transition probability [23-27].

Much work has been done for the last two decade to realize prominent features of quantum wires and to apply them to electronic devices. At the first stage of such work [28-31], quantum wires of the order of 100 nm were fabricated with ultrafine lithography techniques such as electron beam lithography, and a part of the theoretical predictions was demonstrated at low temperature less than 1 K [32]. However, many difficulties were still left to fabricate smaller quantum wires under the quantum limit condition, since it was not trivial to prepare damage-free interfaces by the currently available lithography.

Several alternative approaches to fabricate 10-nm-scale quantum wires were proposed and intensively investigated. In such approaches, defects and roughness at heterointerfaces of quantum wires are avoided by making use of the advanced epitaxial growth technologies without resorting to the ultrafine lithography. For example, V-groove quantum wires were realized by selective growth with MOCVD [33-38], and ridge quantum wires were fabricated on patterned substrates with reverse-mesa structures by MBE [39, 40]. Tilted superlattices and their related structures were grown on vicinal substrates [41-45]. T-shaped quantum wires [46, 47] were formed by overgrowing a quantum well layer on the edge surface of multi-quantum well layer, which is exposed by *in situ* cleavage [48].

Then, the first demonstration of quantum wire lasers was done in 1989 by Kapon et al. [33] Although the confinement of carriers to one-dimensional states was observed in the optical emission spectra, the relatively large size (80-100 by 10 nm) of quantum wires

results in the occupation of many one-dimensional subbands. To achieve the peculiar features predicted by the theory, it is essential to fabricate 10-nm-scale quantum wires and to accommodate most carriers in the ground subbands of quantum wires. Wegscheider et al. have successfully made lasers with 10-nm-scale T-shaped quantum wires and observed stimulated optical emission from the lowest one-dimensional exciton states [47].

Compared with quantum wells, however, fabrication methods of quantum wires are still immature, and it is necessary to improve their uniformity, size, and purity. In addition, so as to gain an insight into one-dimensional effects, one has to develop adequate spectroscopic techniques to characterize quantum wires, in which a high spatial resolution, a high sensitivity, an analysis of polarization, an application of external fields, an experiment at low temperatures, and their combinations are important.

1.2 Objectives

The first objective of this study is "to fabricate high-quality quantum wires whose cross sectional dimensions are less than 10 nm". To demonstrate new features peculiar to one-dimensional systems, one has to realize strong lateral confinement in nanometer-scale quantum wires. In such wires, optical properties are strongly affected by hetero-interfaces. Thus, it is quite important to fabricate wires with smooth and damage-free interfaces. By modifying our MBE system, we will attempt to obtain high-quality T-shaped quantum wires with good controllability.

The second objective is "to demonstrate optical properties of quantum wires predicted by the theory and to explore their unpredicated properties". The first step for the device applications of quantum wires is to fabricate quantum wire samples and to certify theoretical predictions experimentally. Some predictions were so far confirmed with spectroscopic methods. In most of these works, however, the lateral confinement was so weak in quantum wires that one-dimensional effects might be easily obscured by the inhomogenious broadening and other factors. In this study, we will attempt to prepare a series of T-shaped quantum wires with far stronger lateral confinement and to investigate their optical properties systematically. Especially, the adequate comparison with reference quantum wells will be made to evaluate quantitatively effects of lateral confinement.

1.3 Synopses of chapters

In chapter 2, we describe the fabrication procedure of T-shaped quantum wires (T-QWRs) by the cleaved-edge overgrowth method. To obtain sharp and sufficient photoluminescence (PL) from T-QWRs, we refine the *in situ* cleavage process and the condition of overgrowth on (110) edge surfaces. We started from GaAs/AlGaAs material systems, whose epitaxial growth on (110) surfaces have been fairly established and thus favorable to obtain uniform T-QWRs. Then, we expand our efforts into various materials such as GaAs/AlAs and InGaAs/AlGaAs.

In chapter 3, T-QWRs are characterized with the spatially-resolved PL technique. To assign origins of PL peaks from T-QWR samples with such a technique, we design special sample structures. Then, by measuring PL spectra from a series of 5-nm-scale T-QWRs, we demonstrate the enhanced Coulomb interaction energy and other distinct features peculiar to one-dimensional excitons.

In chapter 4, we systematically investigated the polarization dependence of PL and PL excitation spectra on a series of 5-nm-scale T-QWRs. Comparing with a reference quantum well grown on (110) surface, we evaluated the optical anisotropy induced by the lateral confinement in T-QWRs. Then, by carefully comparing intensities of PL excitation spectra among three different T-QWRs, we have evaluated the integrated absorption of one-dimensional excitons, and found that the oscillator strength is concentrated into one-dimensional exciton states with increasing lateral confinement.

In chapter 5, we measured PL spectra from a series of T-QWRs in magnetic fields up to 12 T. Comparing energy shifts of T-QWRs with those of quantum wells, the effect of lateral confinement on exciton wave functions in quantum wires is clearly and quantitatively demonstrated.

Chapter 6 is the summary and the conclusions of this study.

Bibliography

[1] L. Esaki and R. Tsu, IBM Research Note RC-2418 (1969).

[2] L. Esaki and R. Tsu, IBM J. Res. Develop. **14**, 61 (1970).

[3] T. Mimura, S. Hiyamizu, T. Fujii, and K. Nanbu, Jap. J. Appl. Phys. **24**, L225 (1980).

[4] R. Tsu and L. Esaki, Appl. Phys. Lett. **22**, 562 (1973).

[5] L. L. Chang, L. Esaki, and R. Tsu, Appl. Phys. Lett. **24**, 593 (1974).

[6] R. Dingle, Festköperprobleme XV, Advances in Solid-State Physics, ed. by H. J. Queisser (1975).

[7] T. Ishibashi, S. Tarucha, and H. Okamoto, Inst. Phys. Conf. Ser. **63**, 587 (1982).

[8] S. W. Kirchoefer, N. Holonyak, N. Hess, D. A. Gulino, H. G. Drickamer, J. J. Coleman, and P. D. Dapkus, Appl. Phys. Lett. **40**, 821 (1982).

[9] D. A. B. Miller, D. S. Chemla, P. W. Smith, A. C. Gossard, and W. T. Tsang, Appl. Phys. B**28**, 96 (1982).

[10] D. A. B. Miller, D. S. Chemla, D. J. Eilenberger, P. W. Smith, A. C. Gossard, and W. T. Tsang, Appl. Phys. Lett. **41**, 679 (1982).

[11] D. A. B. Miller, D. S. Chemla, D. J. Eilenberger, P. W. Smith, A. C. Gossard, and W. Wiegmann, Appl. Phys. Lett. **42**, 925 (1983).

[12] D. S. Chemla, D. A. B. Miller, P. W. Smith, A. C. Gossard, and W. Wiegmann, IEEE J. Quantum Electron. QE-**20**, 265 (1984).

[13] D. S. Chemla, T. C. Damen, D. A. B. Miller, A. C. Gossard, and W. Wiegmann, Appl. Phys. Lett. **42**, 864 (1983).

[14] D. A. B. Miller, D. S. Chemla, T. C. Damen, A. C. Gossard, W. Wiegmann, T. H. Wood, and C. A. Brrus, Phys. Rev. Lett. **53**, 2173 (1984).

[15] D. A. B. Miller, D. S. Chemla, T. C. Damen, A. C. Gossard, W. Wiegmann, T. H. Wood, and C. A. Brrus, Phys. Rev. B**33**, 1043 (1985).

[16] J. P. van der Ziel, R. Dingle, R. C. Miller, W. Wiegmann, and W. A. Nordland Jr., Appl. Phys. Lett. **26**, 463 (1975).

[17] W. T. Tsang, Appl. Phys. Lett. **39**, 786 (1981).

[18] K. K. Choi, B. F. Levine, C. G. Bethea, J. Walker, and R. J. Malik, Appl. Phys. Lett. **50**, 1814 (1987).

[19] B. F. Levine, K. K. Choi, C. G. Bethea, and R. J. Malik, Appl. Phys. Lett. **51**, 934 (1976).

[20] T. H. Wood, C. A. Burrus, D. A. B. Miller, D. S. CHemla, T. C. Damen, A. C. Gossard, and W. Wiegmann, Appl. Phys. Lett. **44**, 16 (1984).

[21] H. Sakaki, Jpn. J. Appl. Phys. **19**, L735 (1980).

[22] Y. Arakawa and H. Sakaki, Appl. Phys. Lett. **40**, 939 (1982).

[23] R. Loudon, Am. J. Phys. **27**, 649 (1959).

[24] R. J. Elliott and R. Loudon, J. Phys. Chem, Solids **15**, 196 (1960).

[25] S. Abe, J. Phys. Soc. Jap. **58**, 62 (1989).

[26] T. Ogawa and T. Takagahara, Phys. Rev. B**43**, 14325 (1991).

[27] T. Ogawa and T. Takagahara, Phys. Rev. B**44**, 8138 (1991).

[28] P. M. Petroff, A. C. Gossard, R. A. Rogan, W. Wiegmann, Appl. Phys. Lett. **41**, 635 (1982).

[29] M. A. Reed, R. T. Beta, K. Bradshaw, W. M. Duncan, W. R. Frensely, J. W. Lee, and H. D. Shih, J. Vac. Sci. Technol. B**4**, 358 (1986).

[30] J. Chibert, P. M. Petroff, G. J. Dolan, S. J. Pearton, A. C. Gossard, and J. H. English, Appl. Phys. Lett. **49**, 1275 (1986).

[31] H. Temkin, G. J. Dolan, M. B. Panish, and S. N. G. Chu, Appl. Phys. Lett. **50**, 413 (1987).

[32] K.-F. Berggren, T. J. Thornton, D. J. Newson, and M. Pepper, Phys. Rev. Lett. **14**, 1769 (1986).

[33] E. Kapon, D. M. Hwang, and R. Bhat, Phys. Rev. Lett. **63**, 430 (1989).

[34] R. Bhat, E. Kapon, D. M. Hwang, M. A. Koza, and C. P. Yun, J. Cryst. Grwoth **93**, 850 (1988).

[35] E. Kapon, Epitaxial Microstructures, edited by A. C. Gossard, Semicond. and Semimetals **40**, 259 (1994).

[36] E. Kapon, G. Biasiol, D. M. Hwang, M. Walther, and E. Colas, Solid State Electron. **40**, 815 (1996).

[37] S. Tsukamoto, Y. Nagamune, M. Nishioka, and Y. Arakawa, J. Appl. Phys. **71**, 533 (1992).

[38] S. Tsukamoto, Y. Nagamune, M. Nishioka, and Y. Arakawa, Appl. Phys. Lett. **63**, 310 (1993).

[39] S. Koshiba, H. Noge, H. Akiyama, T. Inoshita, Y. Nakamura, A. Shimizu, Y. Nagamune, M. Tsuchiya, H. Kano, H. Sakaki, and K. Wada, Appl. Phys. Lett. **64**, 363 (1994).

[40] S. Koshiba, H. Noge, H. Ichinose, H. Akiyama, Y. Nakamura, T. Inoshita, T. Someya, K. Wada, A. Shimizu, and H. Sakaki, Solid State Electron. **37**, 729 (1994).

[41] M. Tanaka and H. Sakaki, Appl. Phys. Lett. **54**, 1326 (1989).

[42] M. S. Miller, H. Weman, C. E. Pryor, M. Krishnamurthy, P. M. Petroff, H. Kroemer, and J. L. Merz, Phys. Rev. Lett. **68**, 3464 (1992).

[43] J. Bloch, U. Bockelmann, and F. Laruelle, Solid State Elecron. **37**, 529 (1994).

[44] A. Lorke and P. M. Petroff, Solid State Elecron. **37**, 559 (1994).

[45] T. Fukui and H. Saito, Appl. Phys. Lett. **50**, 824 (1987).

[46] A. R. Goñi, L. N. Pfeiffer, K. W. West, A. Pinczuk, H. U. Baranger, H. L. Stormer, Appl. Phys. Lett. **61**, 1956 (1992).

[47] W. Wegscheider, L. N. Pfeiffer, M. M. Dignam, A. Pinczuk, K. West, S. L. McCall, and R. Hull, Phys. Rev. Lett. **71**, 4071 (1993).

[48] L. N. Pfeiffer, K. West, H. L. Stormer, J. P. Eisenstein, K. W. Baldwin, D. Gershoni, and J. Spector, Appl. Phys. Lett. **56**, 1697 (1990).

Chapter 2

Fabrication of T-shaped quantum wires

2.1 Introduction

Following the pioneering proposals by Sakaki and Arakawa [1, 2], a series of efforts have been made for the fabrication of quantum wires and remarkable developments have been witnessed. To realize predicated gains of quantum wires in device applications, quantum wires must satisfy the following three requirements. (1) **Size**: electrons and/or holes must be strongly confined in nanometer scale quantum wires in order to accommodate all the carriers in the ground subband. (2) **Uniformity**: hetero-interfaces of quantum wires must be smooth in the atomic scale, so as to keep the fluctuation of quantum levels far smaller than the thermal energy kT or Fermi energy. (3) **Purity**: dislocations and other defect-complexes as well as residual impurities should be sufficiently reduced to ensure efficient photoluminescence and good electron mobilities. These three requirements had been difficult to meet for a long time because of the lack of control of epitaxial growth and/or damages induced during processing.

However, recent advances in the epitaxial growth technology have provided several new ways to fabricate quantum wires which are about to meet the three requirements. Such activities were briefly reviewed in chapter 1. Especially, T-shaped quantum wires (T-QWRs) [3, 4] fabricated by intersecting two quantum well layers with the cleaved-edge overgrowth method [5] have recently attracted wide attentions, since they exceed the other wires in the several points; structural uniformity, purity, and controllability of structural size.

In this chapter, we describe the method of cleavage and overgrowth, by which high-quality T-QWRs having sharp and efficient photoluminescence were obtained. First, we will introduce T-QWRs in the next section, where the mechanism of two-dimensional confinement in T-QWRs and unique features of T-QWRs are addressed. Next, we will present the fundamental scheme of the cleaved-edge overgrowth method, and then report our attempt to refine *in situ* cleavage process as well as to optimize the condition of overgrowth on (110) cleaved edge surfaces.

2.2 T-shaped quantum wires

T-shaped quantum wires (T-QWRs) which are schematically shown in Fig. 2.1 have been proposed for some years [1, 6] and their fabrications have become possible either by the cleaved edge overgrowth [5] or the facet edge overgrowth method [7, 8]. Using the cleaved-edge overgrowth method, it is possible to fabricate nanometer-scale T-QWRs with the atomic scale precision and good controllability. Indeed, high-quality T-QWRs were successfully formed, and photoluminescence with small energy broadening comparable with that of quantum wells was obtained [4]. For later argument, two quantum wells in Fig. 2.1 are defined as QW1 and QW2, since QW1 and QW2 are formed in the first and the second growth in the cleaved-edge overgrowth method, respectively.

The two-dimensional confinement in T-QWRs is realized by locally modifying the effective thickness of quantum wells in the T-junction part of the structures. The contours of constant probability for electrons confined at the T-QWR state are shown in Fig. 2.1. Similarly, holes are also confined at T-shaped intersections. The wave functions of wire states spread along the direction of weaker confinement, that is, along one of the quantum wells, QW1 or QW2, which has the lower energy level. Therefore, we define the confinement along this quantum well with lower energy as the lateral confinement of T-QWRs.

It is quite important to precisely determine the energy spacing between the lowest energy level of quantum wires and that of the adjacent quantum wells. We denote this quantity as the lateral confinement energy E_{1D-2D}, which is a key parameter to characterize the lateral confinement of T-QWRs. For excitons or electron-hole pairs, we denote it as the effective lateral confinement energy E^*_{1D-2D}. Note that E^*_{1D-2D}

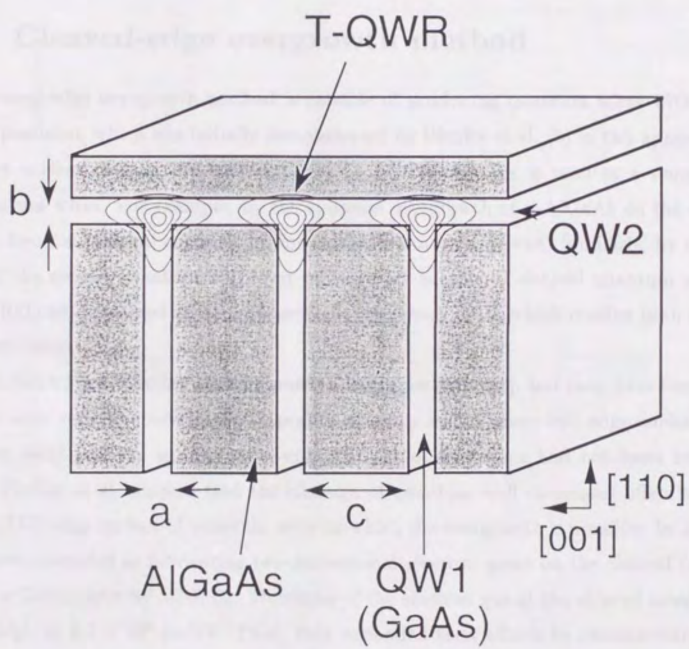

Figure 2.1: The schematic diagram of T-shaped quantum wires (T-QWRs), where QW1 and QW2 are defined. We denote the well thickness of QW1 by a, the well thickness of QW2 by b, the barrier thickness of QW1 by c.

is the energy difference between the one-dimensional exciton state in quantum wires and the two-dimensional exciton state in neighboring quantum wells and is, therefore, a key parameter to represent the stability and the one-dimensional nature of the excitons confined in T-QWRs. It has been pointed out that the lateral confinement of most of T-QWRs is weak. Hence, it is important to precisely characterize E^*_{1D-2D} and to enhance it. We will describe in chapter 3 how to characterize E^*_{1D-2D} and how to optimize E^*_{1D-2D}.

2.3 Cleaved-edge overgrowth method

The cleaved-edge overgrowth method is capable of producing quantum wires with the atomic precision, which was initially demonstrated by Pfeiffer et al. [5] In this approach, the edge surface of quantum wells exposed by *in situ* cleavage is used as a template for quantum wires. For example, by the epitaxial overgrowth of n-AlGaAs on the edge surface, two-dimensional confinement for electrons can be achieved. Similarly, by overgrowing the second quantum well layer on the edge surface, T-shaped quantum wires (T-QWRs) can be formed at the intersection of quantum wells, which confine both electrons and holes.

Such fabrication schemes were proposed a long time ago [1, 6], but they have become possible only recently because the exposure of clean and damage-free edge surface of quantum wells and the subsequent overgrown high-quality films had not been trivial issues. Pfeiffer et al. showed that the cleavage of quantum well structures offers high-quality (110) edge surface of quantum wells on which the overgrowth is possible. In 1990, they have succeeded in fabricating two-dimensional electron gases on the cleaved (110) edge of a GaAs wafer by MBE [5]. Mobilities of the electron gas at the cleaved interface was as high as 6.1×10^5 cm^2/V. Then, they expanded their efforts to demonstrate the capabilities of the cleaved-edge overgrowth method, developing several novel electronic devices. Namely, (1) two-dimensional electron gas subjected to a lateral Kronig-Penney potential of 10 nm periodicity [9], (2) a field effect transistor with an ultra-thin gate of 20 nm length [10], and (3) a 25-nm-wide single quantum wire with a measured transport mean free path exceeding 10 μm [11].

The scheme of T-QWRs was firstly demonstrated by Gõni et al. in 1992 [3]. Then, Wegscheider et al. demonstrated laser action in T-QWRs by optical pumping in 1993

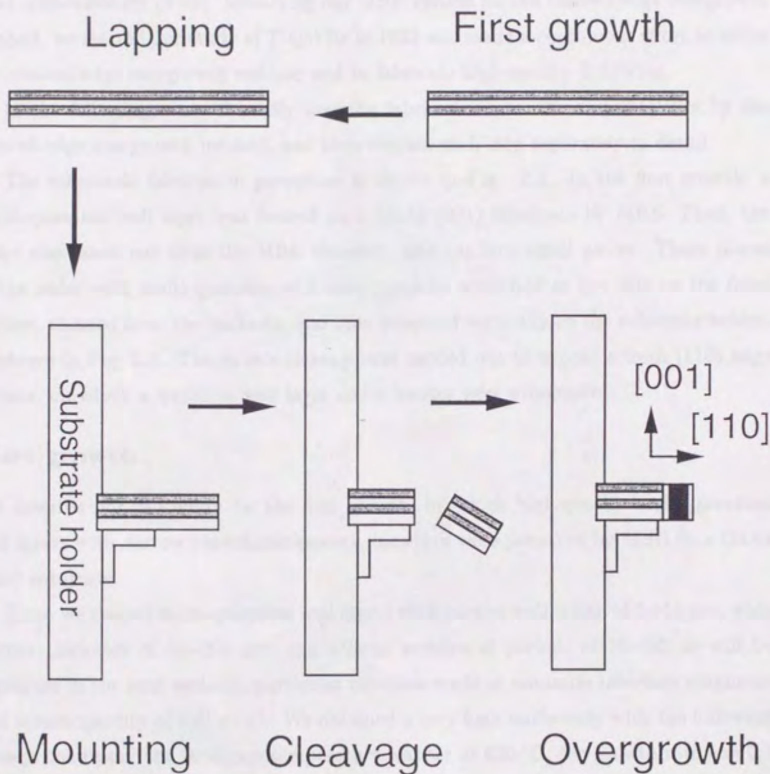

Figure 2.2: The principle of cleaved edge overgrowth method developed originally by Pfeiffer et al. After mounting the wafer with multi-quantum wells vertically on the special substrate holder, in situ cleavage of the wafer is carried out. Then GaAs/AlGaAs hetero-structures are overgrown on the (110) cleaved surface.

[4] and by current injection in 1994 [12]. Now the cleaved-edge overgrowth method is widely recognized as a useful technique to produce high-quality quantum wires with good controllability [9–19]. Modifying our MBE system for the cleaved-edge overgrowth method, we started our study of T-QWRs in 1993 and made a continuous effort to refine the cleaved-edge overgrowth method and to fabricate high-quality T-QWRs.

In the following, we will briefly describe fabrication procedure of T-QWRs by the cleaved-edge overgrowth method, and then explain each step separately in detail.

The schematic fabrication procedure is shown in Fig. 2.2. In the first growth, a multi-quantum well layer was formed on a GaAs (001) substrate by MBE. Then, the wafer was taken out from the MBE chamber, and cut into small pieces. These pieces of the wafer with multi-quantum well were carefully scratched at one side on the front surface, thinned from the backside, and then mounted vertically on the substrate holder, as shown in Fig. 2.3. The *in situ* cleavage was carried out to expose a fresh (110) edge surface, on which a quantum well layer and a barrier were overgrown.

Fisrt growth

We describe our procedure for the first growth, by which high-quality multi-quantum well layers with narrow photoluminescence linewidth were prepared by MBE on a GaAs (001) substrate.

Since we needed multi-quantum well layers with narrow well width of 5∼10 nm, wide barrier thickness of 50∼200 nm, and a large number of periods of 10∼50, as will be explained in the next sections, particular care was made to minimize interface roughness and inhomogeneity of well width. We obtained a very high uniformity with the following growth condition: the substrate temperature was set at 620 °C; the growth rate was 0.7 μm/hr for GaAs; the arsenic pressure was kept low with the V/III flux ratio being about 2; the substrate was rotated at about 10 rpm. The growth was interrupted for 90 sec after the growth of each GaAs layer and for 20 sec after the growth of each AlGaAs layer, to reduce the interface roughness significantly and to sharpen the photoluminescence lines.

In addition, we sandwiched multi-quantum well layers with about 2 μm-thick GaAs cap and buffer layers in the first growth. The thick cap layer was introduced to reduce the edge effects and, therefore, to ensure the uniform overgrowth at T-QWR and QW2 regions.

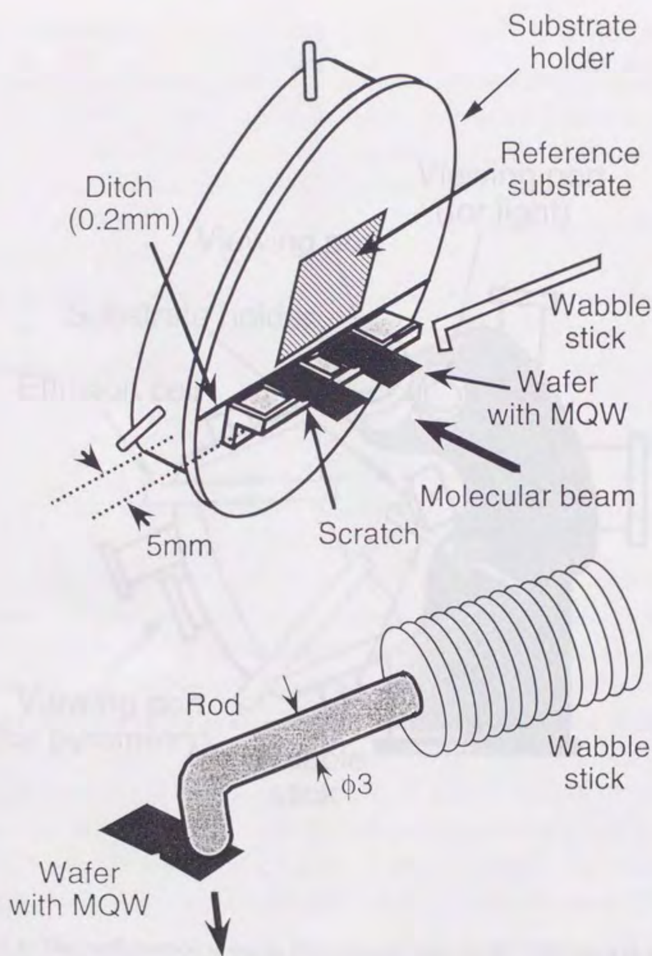

Figure 2.3: The schematic illustration of our substrate holder. Two 90 μm-thick pieces of the wafer with multi-quantum wells are mounted vertically on the substrate holder. Each piece is cleaved one after another by a wabble stick and then overgrown within a few seconds after the cleavage.

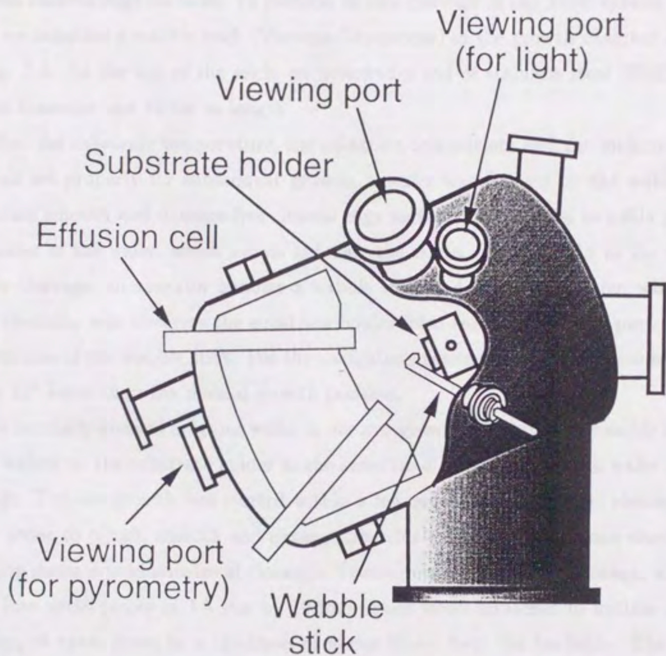

Figure 2.4: The configuration of our in situ cleavage tools in the MBE growth chamber.

In situ cleavage

In the cleaved-edge overgrowth method, edge surfaces of multi-quantum well wafer should be exposed by *in situ* cleavage, which enables one to minimize contaminations adsorbed on fresh cleaved-edge surfaces. To perform *in situ* cleavage in our MBE system (Anelva-831), we installed a wabble stick (Vacuum Generators) in the growth chamber as shown in Fig. 2.4. At the top of the stick, we attached a rod of stainless steel (SUS304) of 3 mm in diameter and 10 cm in length.

After the substrate temperature, the substrate orientation, and the molecular fluxes were all set properly for subsequent growth, a wafer was cleaved by the wabble stick. To obtain smooth and damage-free cleaved edge surfaces, it is crucial to softly push just the center of the wafer, which avoids inducing the stress into the wafer at the cleavage. At the cleavage, an operator handles a wabble stick and pushes the wafer, whereas the other operator who observes the substrate holder from the front viewing port navigates the position of the wabble stick. For the navigator's convenience, a substrate holder was set by $15°$ lower than the normal growth position.

We normally cleaved only one wafer in one overgrowth run, but it is possible to mount a few wafers on the substrate holder at the same time and to cleave each wafer one after another. The overgrowth was started within a few seconds after the last cleavage.

In order to obtain smooth and damage-free cleaved edge reliably, one should avoid inducing stress into substrates at cleavage. To minimize the force for cleavage, we cut the wafer into small pieces of 3.5 mm by 10 mm, made small scratches to initiate cleavage, and lapped them down to a thickness of about $90\mu m$ from the backside. The samples were mounted vertically straight up on the L-shaped part of the substrate holder as shown in Fig. 2.3. To prevent the sliding and inclination of the sample, each piece of the sample was placed side-by-side with additional pieces of clean GaAs wafer chip.

Overgrowth on cleaved edge

We will present the overgrowth of high-quality films on edge surfaces. The epitaxial growth of AlGaAs/GaAs heterostructures on the (110) GaAs was previously investigated by Zhou et al. [20] and Pfeiffer et al. [21] They found that increasing As flux intensity and lowering the substrate temperature are quite effective to obtain high-quality films

with uniform and flat hetero-interfaces and low densities of defects or dislocations. We have grown on (110) substrates under the similar growth condition and found that slower growth rates are desirable to reduce the photoluminescence linewidth. The overgrowth of Al(Ga)As/GaAs heterostructures was carried out at the growth rate of $0.3 \sim 0.5$ μm/hr for GaAs at the substrate temperature of 500 °C and the V/III flux ratio of 30. For In(Ga)As films on (110) GaAs, we will describe the growth condition in the next section.

A particular care was taken to reproduce precisely the temperature on the cleaved edge plane. Since we can not directly measure the temperature of cleaved edges, a (001) GaAs substrate was attached at the center of the substrate holder as shown in Fig. 2.3 and its temperature was monitored using infrared pyrometry. We calibrated the temperature of (001) substrate by watching the oxide desorption process, which is known to take place at 580 °C. The temperature difference between the (110) cleaved edge position and the reference (001) substrate was kept constant by introducing the small scratches on the front side of a wafer piece so that the cleavage takes place at the same position within the accuracy of 0.1 mm. The cleaved surface stood out by 0.4 mm from the top of the substrate holder. In this case, the temperature of the cleaved edge position was lower by about 40 °C than the monitored (001) substrate. Since the temperature difference changed after several growth runs, we often checked it in the test growth runs; the (110) edge surfaces cleaved in the air were mounted at exactly the same position on the same substrate holder, and the oxide desorption process was monitored on (110) edge surfaces. In this way, the overgrowth was carried out at a substrate temperature of 500 °C, which corresponded to the reference substrate temperature of about 540 °C.

2.4 MBE growth of InGaAs on (110)

Heterostructures consisting of GaAs and AlGaAs have been grown on (110) GaAs, as described in §2.3. However, the growth of high-quality In(Ga)As films on (110) GaAs, which will provide new possibilities for T-QWRs, has not been established. In this section, we describe the MBE growth of InGaAs/AlGaAs quantum wells on (110) GaAs. To optimize the growth condition, we changed systematically the substrate temperature T_{sub} for the growth of InGaAs layers. We have found that T_{sub} of 430 °C is optimum to

achieve the good surface morphology and sharp photoluminescence linewidths of InGaAs quantum wells. Under this condition, surface was almost free from facet structures, and photoluminescence linewidth of a 7-nm-thick InGaAs quantum well was as small as 25 meV at 77 K.

Sample preparation

Six samples of $In_{0.15}Ga_{0.85}As/Al_{0.3}Ga_{0.7}As$ quantum wells grown at different substrate temperatures were studied. We first describe the growth procedures. We prepared fresh (110) GaAs surfaces of identical quality by cleaving CrO-doped semi-insulating (001) GaAs substrates in air, which were mounted vertically on a substrate holder shown in Fig. 2.3. After being transferred to the MBE growth chamber, the (110) surface was thermally cleaned at T_{sub} of 580 °C. The temperature of (110) surface is calibrated accurately as described in §2.3. Then, the substrate was cooled down to 500 °C, at which a 150-nm-thick GaAs buffer layer was grown. The growth rate of GaAs was 0.5 μm/hr, and the V/III flux ratio was 30. We then grew a 10-nm-thick $Al_{0.3}Ga_{0.7}As$ layer and 2-monolayer-thick GaAs as a barrier layer. Next, the (110) samples were cooled to temperatures between 390 and 500 °C, at which a 7-nm-thick $In_{0.15}Ga_{0.85}As$ well layer and a 2-monolayer-thick GaAs layer were grown. The role of the 2-monolayer-thick GaAs layers will be discussed later. Finally, the sample was heated up to 500 °C for deposition of a 10-nm-thick $Al_{0.3}Ga_{0.7}As$ barrier layer and a 10-nm-thick GaAs cap layer.

Surface morphology

We examine by optical microscope the surface morphology of six samples. Their Nomarski micrographs are shown in Fig. 2.5. Note that very smooth surfaces with negligibly low density of facet structures were obtained, when InGaAs layer was grown at 430 °C. When grown at temperatures other than 430 °C, the density of facets increased. The surface of samples grown at 500 °C has arrow-like facet structures pointing along the [001] direction, whereas those grown at 390 °C have very large mound-like structures. Although similar arrow-like facets were reported on the surfaces of AlGaAs/GaAs heterostrucutres grown on (110) substrates at 640 °C [22], the mechanism of facet formation has not been clarified yet.

(a) 500°C ⟷ 20μm

(b) 445°C

(c) 430°C

(d) 415°C

(e) 405°C

(f) 390°C

Figure 2.5: Nomarski micrographs showing the surface morphology of six $In_{0.15}Ga_{0.85}As/Al_{0.3}Ga_{0.7}As$ heterostrucutres. The substrate temperature at which the $In_{0.15}Ga_{0.85}As$ well layer was grown is indicated.

Photoluminescence study

We measured the photoluminescence from six InGaAs quantum wells at 77K. Photoluminescence was excited by the blue-green lines (488, 514 nm, etc.) of an Ar^+ laser with an excitation intensity of 30 W/cm^2 and detected by a GaAs photomultiplier. The excitation and the detection were performed on the (110) surface in a backward scattering geometry.

We show in Fig. 2.6 the photoluminescence spectra from six samples. The photoluminescence peak in each curve is from the single 7-nm-thick InGaAs quantum well with barrier layers that consisted of 2-monolayer-thick GaAs and 10-nm-thick AlGaAs. The maximum photoluminescence intensity and the minimum photoluminescence linewidth of 25 meV were obtained in the sample grown at 430 °C. Samples grown at other temperatures show much weaker photoluminescence with the increased linewidth, including additional side peaks in lower energy of the main peak. We speculate that the side peak in quantum well samples grown at 405 and 390 °C is related to acceptor impurities, since its energy is close to binding energies of acceptor in quantum wells [24]. The origin of broad photoluminescence spectrum of sample grown at 500 °C is not specified, but might be related not only with impurities but also with local variation of indium content in the quantum well layer, as the incorporation rate of indium and gallium may be disturbed by the presence of arrow-like facet structures. Therefore, we conclude that the optimum substrate temperature for the growth of InGaAs quantum well on (110) GaAs is 430 °C, at which the best surface morphology and the sharp and intense photoluminescence can be obtained.

Discussion

We should note here that the difference in surface morphologies and photoluminescence spectra of these samples is caused by the difference of substrate temperature during the deposition of 7-nm-thick InGaAs layers, since the growth condition for AlGaAs/GaAs heterostructures is identical. As described earlier, the optimum substrate temperature for obtaining high quality InGaAs layers is 430 °C, whereas the substrate temperature for the growth of AlGaAs/GaAs heterostructures on (110) GaAs is 500 °C [5]. This difference of optimum condition results from the fact that the desorption, surface migration, and/or

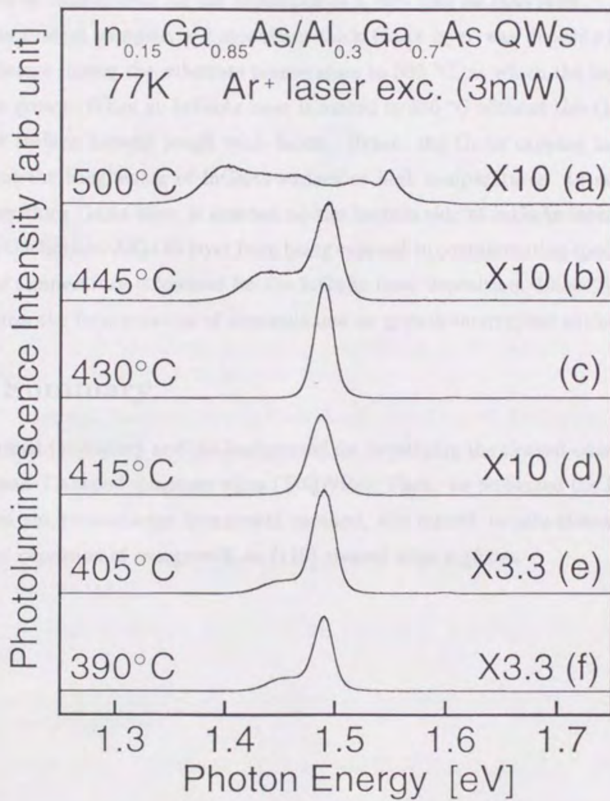

Figure 2.6: Photoluminescence spectra of 7-nm-thick $In_{0.15}Ga_{0.85}As$ quantum wells grown at various substrate temperatures. Spectra were measured at 77 K with an Ar^{+} laser.

segregation processes of indium atoms are different from those of gallium or aluminum atoms. Indeed, the surface becomes quite rough and the photoluminescence broadens when 7-nm-thick InGaAs is deposited at 500 °C. Therefore, the growth condition should be always optimized even for the deposition of a very thin InGaAs layer.

In the present samples, a 2-monolayer-thick GaAs layer was deposited on InGaAs surface before raising the substrate temperature to 500 °C, at which the top of AlGaAs layer was grown. When an InGaAs layer is heated to 500 °C without this GaAs capping layer, its surface became rough with facets. Hence, the GaAs capping layer is found to prevent the roughening of InGaAs surface at high temperatures. In addition, a 2-monolayer-thick GaAs layer is inserted on the bottom side of InGaAs layer. This layer prevents the bottom AlGaAs layer from being exposed to contaminating species while the substrate temperature is lowered for the InGaAs layer deposition. Hence, it is effective to minimize the incorporation of contaminants on growth-interrupted surfaces [25].

2.5 Summary

We described the history and the background for developing the cleaved-edge overgrowth method and T-shaped quantum wires (T-QWRs). Then, we presented the fundamental scheme of the cleaved-edge overgrowth method, the refined *in situ* cleavage, and the optimized condition of overgrowth on (110) cleaved edge surfaces.

Bibliography

[1] H. Sakaki, Jpn. J. Appl. Phys. **19**, L735 (1980).

[2] Y. Arakawa and H. Sakaki, Appl. Phys. Lett. **40**, 939 (1982).

[3] A. R. Goñi, L. N. Pfeiffer, K. W. West, A. Pinczuk, H. U. Baranger, H. L. Stormer, Appl. Phys. Lett. **61**, 1956 (1992).

[4] W. Wegscheider, L. N. Pfeiffer, M. M. Dignam, A. Pinczuk, K. West, S. L. McCall, and R. Hull, Phys. Rev. Lett. **71**, 4071 (1993).

[5] L. N. Pfeiffer, K. West, H. L. Stormer, J. P. Eisenstein, K. W. Baldwin, D. Gershoni, and J. Spector, Appl. Phys. Lett. **56**, 1697 (1990).

[6] Y. C. Chang, L. L. Chang, and L. Esaki, Appl. Phys. Lett. **47**, 1324 (1985).

[7] S. Shinomura, K. Inoue, M. Tanaka, N. Tomita, A. Adachi, M. Fujii, T. Yamamoto, T. Watanabe, N. Sano, K. Murase, and S. Hiyamizu, Solid-States Electron. **37**, 597 (1994).

[8] M. Tanaka, J. Cryst. Growth **150**, 388 (1995).

[9] H. L. Stormer, L. N. Pfeiffer, K. W. Baldwin, K. W. West, and J. Spector Appl. Phys. Lett. **58**, 726 (1991).

[10] H. L. Stormer, K. W. Baldwin, L. N. Pfeiffer, and K. W. West, Appl. Phys. Lett. **59**, 1111 (1991).

[11] A. Yacoby, H. L. Stormer, K. W. Baldwin, L. N. Pfeiffer, and K. W. West, Phys. Rev. Lett. (to be published).

[12] W. Wegscheider, L. Pfeiffer, K. W. West, and R. E. Leibenguth, Appl. Phys. Lett. **65**, 2510 (1994).

[13] D. Gershoni, J. S. Weiner, S. N. G. Chu, G. A. Baraff, J. M. Vanderberg, L. N. Pfeiffer, K. W. West, R. A. Rogan, and T. Tanbun-Ek, Phys. Rev. Lett. **65**, 1631 (1990).

[14] L. N. Pfeiffer, H. L. Stormer, K. W. Baldwin, K. W. West, A. R. Goñi, A. Pinczuk, R. C. Ashoori, M. M. Dignam, W. Wegscheider, J. Cryst. Growth **127**, 849 (1993).

[15] J. Motohisa and H. Sakaki, Appl. Phys. Lett. **63**, 1786 (1993).

[16] W. Wegscheider, W. Kang, L. N. Pfeiffer, K. W. West, H. L. Stormer, and K. W. Baldwin, Solid-States Electronics, **37**, 547 (1994).

[17] M. M. Dignam, R. C. Ashoori, H. L. Stormer, L. N. Pfeiffer, K. W. Baldwin, and K. W. West, Phys. Rev. B**49**, 2269 (1994).

[18] C. Kurdak, D. C. Tsui, S. Parihar, M. B. Santos, H. C. Manoharan, S. A. Lyon, and M. Shayegan, Appl. Phys. Lett. **64**, 610 (1994).

[19] M. Grayson, C. Kurdak, D. C. Tsui, S. Parihar, S. A. Lyon, and M. Shayegan, Solid-States Electronics, **40**, 233 (1996).

[20] J. Zhou, Y. Huang, Y. Li, and W. Y. Jia, J. Cryst. Growth **81**, 221 (1987).

[21] L. N. Pfeiffer, H. L. Stormer, K. West, and K. W. Baldwin, J. Cryst. Growth **111**, 333 (1991).

[22] M. C. Holland, A. H. Kean, and C. R. Stanley, J. Cryst. Growth **150**, 455 (1995).

[23] K. Radhakrishnan, S. F. Yoon, H. M. Li, Z. Y. Han, and D. H. Zhang, J. Appl. Phys. **76**, 246 (1994).

[24] R. C. Miller, A. C. Gossard, W. T. Tsang, and O. Munteanu, Phys. Rev. B**25**, 3871 (1982).

[25] T. Someya, H. Akiyama, Y. Kadoya, T. Noda, T. Matsusue, H. Noge, and H. Sakaki, Appl. Phys. Lett. **63**, 1924 (1993).

Chapter 3

Spatially-resolved photoluminescence

3.1 Introduction

Optical spectroscopy is an important tool for the characterization of semiconductor microstructures. Before the detailed spectroscopy, the first step to characterize a quantum wire is to determine its structure and its energy level precisely. For this purpose, one exploits advanced instruments to characterize structures with the resolution of several atomic layers or less, such as transmission electron microscope (TEM), scanning electron microscope (SEM), scanning tunneling microscope (STM), and atomic force microscope (AFM). From the observation of the cross sectional views, structures (shape and size) of quantum wires, namely potential of quantum wires, can be determined. However, for the structural characterization of T-shaped quantum wires (T-QWRs) made by the cleaved-edge overgrowth method with high controllability, one needs only to determine energy levels of two adjacent quantum wells; QW1 formed in the first growth and QW2 formed in the second growth after cleavage. Hence, it is quite important to measure separately the energy levels of quantum wires and those of two adjacent quantum wells. In addition, measurement of these three energy levels is also essential to determine the effective lateral confinement energy E^{*}_{1D-2D}, as explained in chapter 2.

Spatially-resolved spectroscopy is suitable for such an optical characterization of quantum wires. Photoluminescence spectra from low-dimensional structures, containing quantum wires or quantum dots, sometimes show multiple peaks. In such a case, by picking up the local information with spatially-resolved spectroscopy, each peak can

be assigned to the corresponding structure. In addition, spatially-resolved spectroscopy makes measurements insensitive to the inhomogeneity of structures, and therefore, an accurate and detailed spectroscopy becomes possible. Up to now, cathodoluminescence [1], near-field optical microscope [2, 3], and micro-photoluminescence [4–6] are used for the spatially-resolved measurement of quantum confined structures. Especially, micro-photoluminescence have the following two advantages. (1) An experimental setup is simple, and a measurement is relatively easy even at low temperatures. (2) A variety of excitation laser source is available, which provides various feasibility for spectroscopy. In this measurement, spatial resolutions are limited by the refraction limit of wavelength. Therefore, it seems fairly larger than those of the other sophisticated spatially-resolved spectroscopies. However, as will be explained in the following sections, a spatial resolution of a few μm is sufficient in most cases, if sample structures are devised, and provides various and useful possibilities for spectroscopy.

In this chapter, we will present our specially-resolved photoluminescence measurements on various types of T-QWRs, which reveal their novel one-dimensional properties such as large lateral confinement and enhanced exciton binding energy E_b. First, we describe the characterization method of T-QWRs based on specially-resolved photoluminescence technique, where special sample structures were designed. Then, we fabricate a series of nanometer-scale T-QWR samples whose structural parameters are changed systematically, and characterize their structures and energy levels via spatially-resolved photoluminescence measurements.

3.2 Characteriztion by spatially-resolved photoluminescence

To characterize T-QWRs using the specially-resolved photoluminescence technique with a few μm resolution, the particular care should be made on sample structures. We first describe in this section the design principle for our special sample structures, by which all photoluminescence lines from T-QWRs, QW1, and QW2 can be detected and identified simply with spatially-resolved photoluminescence technique. Then, we prepare three types of T-QWR samples and present the results of spatially-resolved photoluminescence study.

Design of sample structures

To realize the strong lateral confinement in T-QWRs, that is, to maximize the effective lateral confinement energy of excitons E^*_{1D-2D}, the thickness a of QW1 and the thickness b of QW2 must be sufficiently small (< 10 nm) and set close to each other [7,8]. Then, the interwire interval c, or the barrier thickness of QW1, must be carefully chosen. To prevent the quantum coupling of T-QWRs completely, c must be sufficiently thick and typically larger than 50 nm. Otherwise, T-QWR states and the continuum state corresponding to QW2 tend to merge or mix, which modifies the quantized energy of T-QWR and QW2 states.

If we prepare T-QWR samples with these parameters, photoluminescence spectra from the T-QWR and QW1 can be easily detected. However, the photoluminescence from QW2 is still difficult to observe because of the fast carrier diffusion from the QW2 region to the T-QWR [2]. This situation is analogous to the familiar fact that photoluminescence spectra from multi-quantum well structures are usually dominated by those from quantum wells since carriers generated in the barrier region are efficiently collected by the quantum well region. As a result, special sample structures are required to detect photoluminescence from QW2. In the following, we will introduce two sample structures to allow the photoluminescence measurement of QW2 with the help of spatially-resolved photoluminescence spectroscopy.

The first approach is to simply form in the first growth a very thick AlGaAs barrier layer ($\gg$1 μm) after the multiple QW1 layers as shown in Fig. 3.1 (a); when we form the QW2 layer by the cleaved-edge overgrowth on the edge surface of such a wafer, a large QW2 region is formed as denoted by QW2-s in Fig. 3.1 (a) and allows the detection of photoluminescence from QW2.

The second approach is to deposit in the second growth a special structure which consists of not only the QW2 layer to form T-QWRs but also an additional QW2 layer (denoted as QW2-u) as shown in Fig. 3.1 (b). Of course, in this approach, the thickness of the second QW2 layer is set to be equal to that of the first QW2 layer. As photogenerated carriers do not migrate to T-QWRs, photoluminescence signal from QW2-u layer serves as a reference, as will be discussed later.

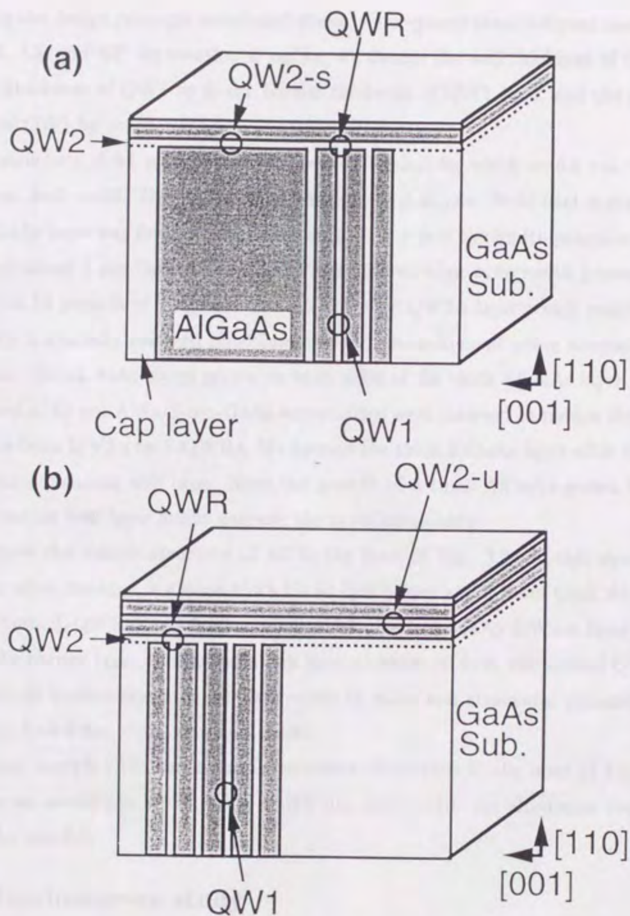

Figure 3.1: The structures of our samples specially designed for the present work. QW2-s or QW2-u is prepared in the sample to determine the quantized energy of QW2.

Sample preparation

Following the design principle mentioned above, we prepared three different sample structures A1, A2, and A3. As mentioned earlier, we denote the well thickness of QW1 by a, the well thickness of QW2 by b, the barrier thickness of QW1 by c, and the number of periods of QW1 by n.

The structure of A1 is shown in the inset of Fig. 3.2, for which a=6.0 nm, b=6.4 nm, c=100 nm, and n=50. The barrier layers are of $Al_{0.3}Ga_{0.7}As$. Note that a very thick (5 μm) AlGaAs layer was formed in the first growth on top of the multi-quantum well layer (QW1) of about 5 μm thick. Hence, after the cleaved-edge overgrowth process, we got an array of 50 periods of T-QWRs and a 5-μm-wide QW2-s layer which could be easily studied by a spatially-resolved photoluminescence measurement using normal objective lens optics. Extra AlAs layers grown on both sides of the thick AlGaAs layer consisting of 5-period of 10-nm-AlAs/1-nm-GaAs superlattice were inserted to reduce the diffusion of carriers from QW2-s to T-QWRs. We formed the thick AlGaAs layer after the growth of the multi-quantum well layer, since the growth of a thick AlGaAs grown before the multi-quantum well layer might degrade the interface quality.

We show the sample structure of A2 in the inset of Fig. 3.3. In this structure, we overgrew, after cleavage, a 4.8-nm-thick GaAs QW2 layer and a 8-nm-thick AlAs barrier layer to form T-QWRs, and further grew a 4.8-nm-thick GaAs QW2-u layer, a 8-nm-thick AlAs barrier layer, and a GaAs cap layer in order to form the second QW2 layer. Note that all barrier layers of A2 were made of AlAs and structural parameters were a=5.3 nm, b=4.8 nm, c=50 nm, and n=50.

The last sample (A3) had a simple structure illustrated in the inset of Fig. 3.4, for which we set a=9.8 nm, b=11.6 nm, c=200 nm, and n=10. An aluminum composition in AlGaAs was 0.3.

Photoluminescence study

We measured photoluminescence spectra from these three samples with a conventional micro-photoluminescence setup using a long-working-distance objective lens. The photoluminescence was detected via the (110) surface in the backward scattering geometry. The signal was measured with the lock-in detection technique with a GaAs

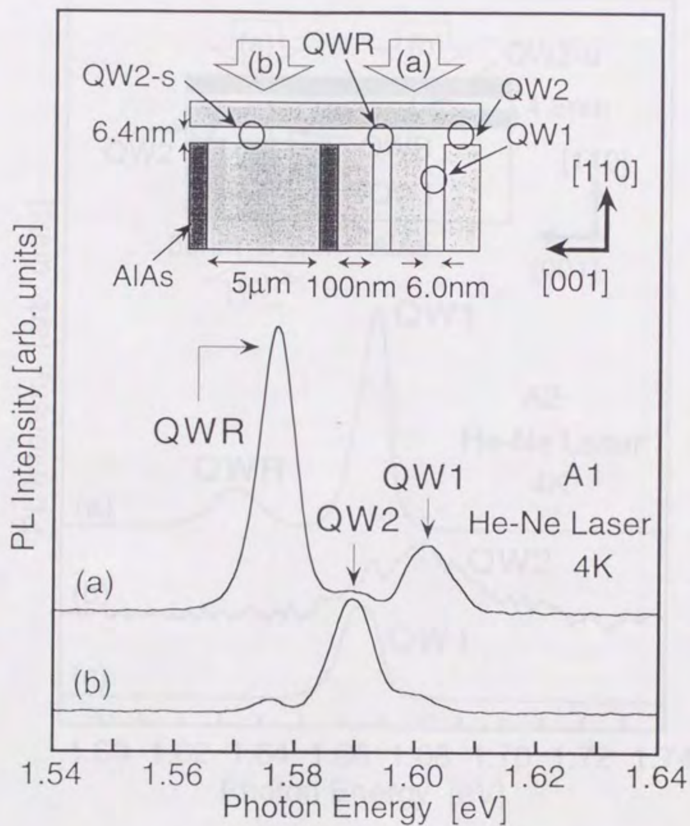

Figure 3.2: The schematic structure and photoluminescence spectra of A1 measured at 4 K. QW2-s was formed simultaneously in the overgrowth. AlAs layers work as the diffusion barrier of carriers. The excitation source was a He-Ne laser with a spot diameter of 2 μm. Curves a and b were obtained when the excitation beam was aligned on the quantum wire region (spot a) and the QW2-s region (spot b), respectively.

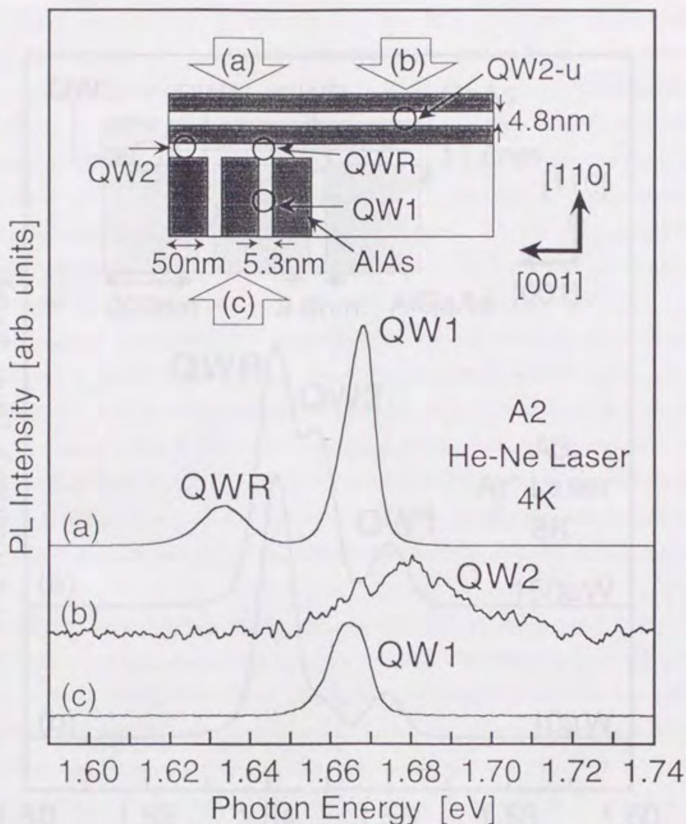

Figure 3.3: Photoluminescence spectra of A2 at 4 K. The excitation source was a He-Ne laser with a spot diameter of 2 μm. Curves a and b were obtained when the excitation beam was aligned on the region (spot a) of wire arrays and the substrate (spot b), respectively. Curve c was measured when the excitation laser beam was moved to the QW1 region without overgrowth. The schematic structure of A2 is also shown in the inset.

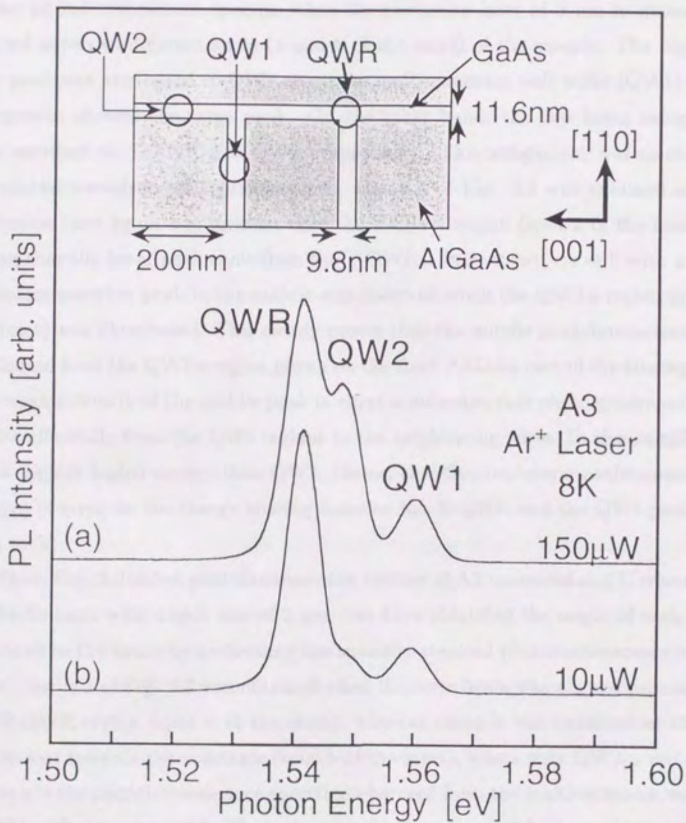

Figure 3.4: Photoluminescence spectra of A3 measured at 4K with Ar^+ laser with different excitation intensities. Three peaks were clearly observed and assigned as indicated. The structure of A3 is also shown in the inset.

photo-multiplier. Detailed description of the experimental setup will be given in §4.2

First, photoluminescence spectra of A1 were studied at 4 K using He-Ne laser (λ=633 nm) as an excitation source. As shown in Fig. 3.2, three peaks were clearly observed in two photoluminescence spectra, when the excitation laser of 2 μm in diameter was focused onto two different spots (a and b of the inset) of the sample. The highest energy peak was attributed to QW1, since the multi-quantum well wafer (QW1) without overgrowth showed the same peak. On the other hand, the two lower energy peaks were ascribed to T-QWR and QW2, respectively. This assignment was confirmed by the spatially-resolved photoluminescence. Curve a of Fig. 3.2 was obtained when the excitation laser beam was incident onto the T-QWR region (spot a of the inset), indicating that the lower peak came from the T-QWRs. In contrast, curve b with a distinct photoluminescence peak in the middle was observed when the QW2-s region (spot b in the inset) was illuminated. This clearly proves that the middle photoluminescence peak originated from the QW2-s region grown on the thick AlGaAs part of the cleavage plane. The weak intensity of the middle peak in curve a indicates that photo-generated carriers diffuse efficiently from the QW2 regions to the neighboring wires. In this sample, QW1 has a slightly higher energy than QW2. Hence, the effective lateral confinement energy E^{*}_{1D-2D} is given by the energy spacing between the T-QWR and the QW2 peak, which is 11 meV.

Then, Fig. 3.3 shows photoluminescence spectra of A2 measured at 4 K when excited by He-Ne laser with a spot size of 2 μm. We have identified the origin of each peak as indicated in the figure by performing the spatially-resolved photoluminescence measurement. Curve a of Fig. 3.3 was obtained when the laser beam was aligned primarily onto the T-QWR region (spot a of the inset), whereas curve b was obtained as the beam was moved towards the substrate (spot b of the inset), where only QW2-u was excited. Curve c is the photoluminescence spectrum observed from the multi-quantum well wafer (QW1) without overgrowth. Thus, the photoluminescence peak of curve b is attributed to QW2-u, whereas the peak of curve c is to QW1. The higher energy peak of curve a is similar to the peak in curve c and, therefore, is attributed to QW1. The lowest energy peak is finally ascribed to T-QWR. Since QW2 has a slightly higher energy than QW1, the effective lateral confinement energy E^{*}_{1D-2D} is equal to the energy spacing between the T-QWR and the QW1 peak. Note that the value of E^{*}_{1D-2D} in this sample is as large

as 35 meV.

Finally, we studied photoluminescence from A3 at 4 K using the blue-green lines (488 nm, 514 nm, etc) of an Ar^+ laser. Three photoluminescence lines were clearly observed as shown in Fig. 3.4. We have assigned the highest energy peak as the photoluminescence originating from QW1 as it coincides with the photoluminescence spectrum coming from the multi-quantum well sample before cleaved-edge overgrowth. The middle peak and the lowest peak were found to come from QW2 and T-QWRs, respectively, which will be discussed in detail later. Since QW1 is slightly thinner than QW2, photoluminescence from QW1 has higher energy than that from QW2. Hence, the effective lateral confinement energy E^*_{1D-2D} of T-QWR is equal to the energy spacing between the T-QWR and the QW2 peak, and is found to be 6 meV in this sample.

Note that photoluminescence from QW2 was detected in spite of the fact that the wire-to-wire distance c was much less than the diffusion length L_D of excitons along QW2 plane. Since E^*_{1D-2D} of this T-QWR is as small as 6 meV, carriers are activated from T-QWR to QW2 and contribute to photoluminescence from QW2 states.

The validity of our assignment of two photoluminescence peaks from QW2 and T-QWRs has been checked by performing several independent experiments, such as the dependence of photoluminescence spectra on magnetic fields and excitation density and also by the comparison with photoluminescence data of other samples. For example, the relative intensity of middle peak in Fig. 3.4 increases when the excitation intensity increases by a factor of 15, as shown by curves a and b. This is because the increase of excitation enhances carrier density, carrier temperature, and carrier-carrier scattering, which activates excitons from T-QWR to QW2. Note that the spatial resolution of luminescence study with local excitation is generally limited by the diffusion length L_D, and is not enough to resolve the luminescence from such a structure with the wire-to-wire distance c=200 nm. In fact, a cathodoluminescence measurement could not resolve the middle luminescence peak from the rest for this sample structure.

Discussion

We discuss both advantages and disadvantages of three sample structures (A1~A3). Despite its simplicity, the sample structure of A3 has several drawbacks for spectroscopic studies. In T-QWRs with large E^*_{1D-2D}, the wire-to-wire distance c must be set larger

than the diffusion length L_D along QW2 plane, which is typically 500 nm when L_z=7 nm and T=4 K [2]. Otherwise, photoluminescence from QW2 can hardly be detected, since carriers generated in the QW2 region will be lost by the diffusion of carriers into T-QWRs and hardly activated from T-QWR to QW2. If c is set larger than the diffusion length L_D, the spatially-resolved detection of photoluminescence spectra from T-QWR and QW2 becomes, in principle, possible. Even in such a case, however, one must still use advanced luminescence spectroscopy with very high spatial resolution better than c; for example, cathodoluminescence or near-field optical microscope is desirable. In addition, one must note that the growth of high-quality QW1 layers with c larger than 100 nm is not usually easy since the interface roughness tends to develop when we prepare thick AlGaAs layers.

In contrast, sample structures of A1 and A2 are free from these problems as discussed earlier, and the identification of photoluminescence peaks can be made even with objective-lens-based photoluminescence setup having a moderate spatial resolution. Although the structures of A1 and A2 are attractive, each has its own advantage and drawback. For example, in order to fabricate GaAs T-QWRs with AlGaAs barriers, the structure of A1 is more preferable than that of A2. It is because the aluminum compositions in AlGaAs layers prepared in the first growth and those formed in the overgrowth may not be exactly the same. If such an error occurs, the quantized energy of QW2 may be slightly different from that of QW2-u, which causes an error in the evaluation of E^{*}_{1D-2D}. Of course, an error can be automatically avoided in A1.

When it comes to T-QWRs with AlAs barriers, structure of A2 is preferred over A1. It is because, to observe photoluminescence from QW2, a very thick AlAs layer must be grown on the top of multi-quantum well layer in the first growth, which is known to be very unstable and may lead to the degradation of the sample quality. Hence sample structures like A2 are more favorable for the fabrication of GaAs T-QWRs with AlAs barriers.

We stress again the importance of detecting and identifying all photoluminescence lines from QW1, QW2, and T-QWRs. As we mentioned earlier, these identifications are indispensable to precisely determine E^{*}_{1D-2D}, which is the key parameter to present the lateral confinement in T-QWRs. In addition, the photoluminescence signal from QW2 is important to evaluate precisely the rate of the second growth and the thickness of

QW2. Furthermore, photoluminescence signal from QW2 is quite valuable as a reference signal, especially, when we investigate novel properties of one-dimensional excitons in T-QWRs. For example, unique properties of one-dimensional excitons such as optical anisotropy of absorption [9], diamagnetic shifts [10], radiative lifetime of one-dimensional excitons [11–13], two-photon absorption [14–16] has been established unambiguously only by comparing them with two-dimensional natures of quantum well samples.

3.3 Structure dependence of energy levels

Using the cleaved edge overgrowth method, it is possible to change structural parameters of T-QWRs with high controllability. In addition, the shape of T-QWRs is quite simple and described by two parameters; the thickness a of QW1 and the thickness b of QW2. As a result, by changing a and b systematically, a series of samples with quantum wires are obtained, which enables one to gain an insight into the structure dependence of optical properties in one-dimensional systems.

In this section, we fabricate a series of T-QWR samples whose structural parameters are changed systematically, and then characterize their structures and energy levels via spatially-resolved photoluminescence measurements. Especially, we prepare 5-nm-scale T-QWRs, since our interest is to magnify optical effects inherent to quantum wires. We should note that their structural size is set smaller than Bohr radius of excitons in bulk (12 nm).

Sample preparation

We have fabricated two series of T-QWRs (S1 and S2). Both series were specially designed for the subsequent spatially-resolved photoluminescence measurement. The structure of S1 is shown in the inset of Fig. 3.5 (a). A multi-quantum well (QW1) layer and a 5-μm-thick $Al_{0.3}Ga_{0.7}As$ layer were formed in the first growth; The QW1 layer contains 50 periods of GaAs quantum wells with thickness a=5.4 nm separated by $Al_{0.3}Ga_{0.7}As$ barriers with thickness c=100 nm. After cleavage, a GaAs quantum well layer (QW2) with various thickness b and a 20-nm-thick $Al_{0.3}Ga_{0.7}As$ barrier layer were deposited in the second growth onto a cleaved (110) surface. In this way, we got an array of 50 periods of T-QWRs and a 5-μm-wide QW2 layer. Extra AlAs layers, which

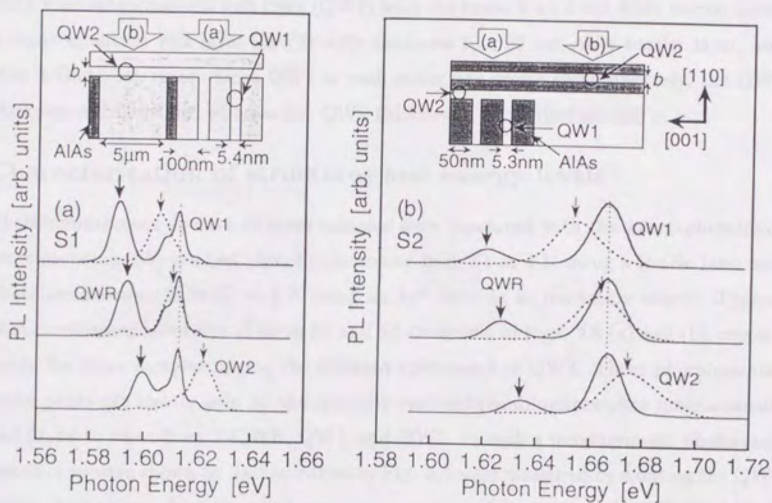

Figure 3.5: Typical spatially-resolved photoluminescence spectra from quantum wells (QW1 and QW2) and T-QWRs of two series of samples with various thickness b of QW2. The data for series S1 are given in (a) and those of series S2 are in (b). Photoluminescence spectra shown by dashed curves were measured by exciting the QW2 region, while those shown by solid curves were measured by exciting the T-QWR region.

consisted of 5 periods of 10-nm-AlAs/1-nm-GaAs superlattice, were inserted on both sides of the 5 μm AlGaAs layer to reduce the diffusion of photo-generated carriers from QW2 to T-QWRs.

Next, we show the sample structure of S2 in the inset of Fig. 3.5 (b). In the first growth, we prepared a multi-quantum well layer, which consists of 10 periods of GaAs quantum wells (QW1) with thickness a=5.3 nm separated by AlAs barriers with thickness c=50 nm in between. After the cleavage, we overgrew on the (110) cleaved surface a GaAs quantum well layer (QW2) with thickness b, an 8 nm AlAs barrier layer, a GaAs quantum well layer (QW2) with thickness b, a 20 nm AlAs barrier layer, and then a GaAs cap layer. Since QW1 in each series was grown simultaneously, the QW1 thickness a is constant, whereas the QW2 thickness b is changed around a.

Characterization of structures and energy levels

Photoluminescence spectra of these samples were measured with the micro-photoluminescence setup. We studied photoluminescence from S1 at 4 K using a He-Ne laser and photoluminescence from S2 at 8 K using an Ar^+ laser as an excitation source. Typical photoluminescence spectra of series S1 and S2 are shown in Figs. 3.5 (a) and (b), respectively, for three samples having the different thickness b of QW2. Three photoluminescence peaks are clearly seen by the spatially-resolved photoluminescence measurement, and found to come from T-QWR, QW1, and QW2. In such a measurement, photoluminescence spectra shown by dashed curves in Fig. 3.5 were measured by exciting the QW2 region, while those shown by solid curves were measured by exciting the T-QWR region. As a result, we can precisely determine potential profiles and quantized energies of T-QWRs. All the photoluminescence peaks of S1 are sharp with linewidth of 5-10 meV, indicating the good uniformity of the structures. Although the photoluminescence peaks of S2 are broader due to the tighter confinement, photoluminescence from T-QWRs is still sharp with the linewidth of 14 meV.

We determined the energies of photoluminescence peaks from twenty samples in S1 and eleven samples in S2. They are plotted in Fig. 3.6 against the QW2 thickness b, in which photoluminescence energies of T-QWR are shown by solid circles, those of QW1 by blank squares, and those of QW2 by blank circles. Here, the QW2 thickness b is not nominal thickness, but is determined by comparing the observed photoluminescence

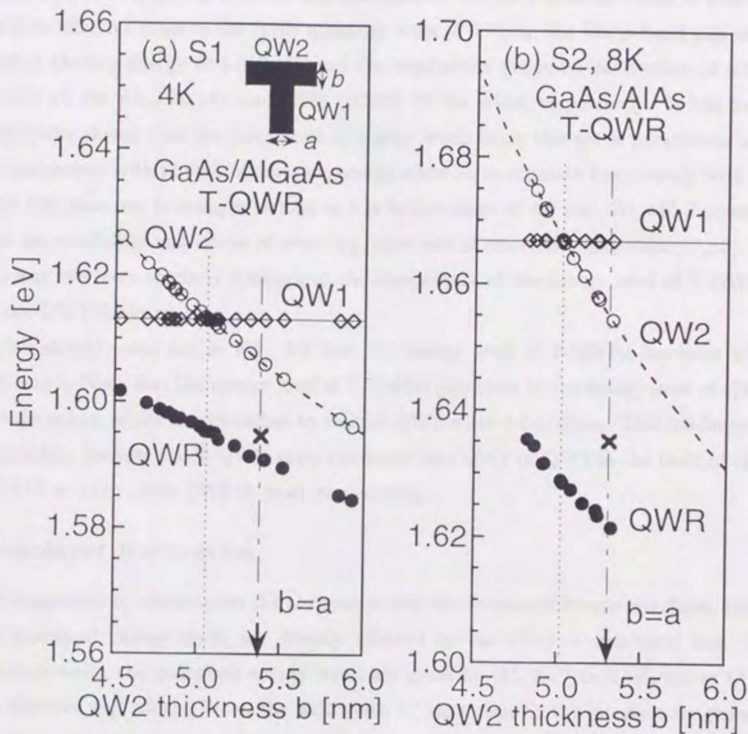

Figure 3.6: The energies of photoluminescence peaks are shown by solid circles for T-QWRs, by blank squares for QW1, and by blank circles for QW2 in S1 (a) and S2 (b) as a function of the QW2 thickness b. The broken curves show the energy level of QW2 calculated under the effective mass approximation. The dotted lines indicate the energy level when the levels of QW2 and QW1 are identical. The dash-dot lines indicate the identical thickness b with a.

peak of QW2 with the theoretical value; for this purpose, we calculated the energy level of QW2 under the effective mass approximation, and the result is shown by broken curves in Fig. 3.6. Here, we used the following conventional parameters; the electron effective mass of $0.067m_0$, the hole effective mass in the (001) quantum wells of $0.38m_0$, the hole effective mass in the (110) quantum wells of $0.71m_0$, the GaAs band gap with exciton binding energy of 1.519 eV, and the conduction (valence) band offset of 0.243 (0.131) eV for $Al_{0.3}Ga_{0.7}As$ and 1.036 (0.558) eV for AlAs, respectively. It has been empirically shown that the calculation of energy levels using this set of parameters and its comparison with photoluminescence energy allow us to estimate b accurately with an error less than one monolayer as long as b is in the range of 4-9 nm. We will discuss in §3.4 the possibility and effects of selecting other sets of material parameters [17, 18]. In this way, we have precisely determined the dependence of the energy level of T-QWRs on the QW2 thickness b.

We should point out in Fig. 3.6 that the energy level of T-QWRs increases with reducing b. Note that the energy level of T-QWRs gets close to the energy level of QW1 as b decreases, while it approaches to that of QW2 when b increases. This tendency is reasonable, because the T-QWR state converges into QW1 or QW2 in the limit of thin QW2 ($b \ll a$) or thick QW2 ($b \gg a$), respectively.

Monolayer fluctuation

It is important to characterize the abruptness and the flatness of hetero-interfaces, since the quantized energy levels are directly affected by the effective structural size. In quantum wells, the quantized energy levels are given by $(\hbar^2/2m)(n\pi/L^*)^2$, where L^* is the effective well width. When the well width L^* varies due to the interface roughness, the fluctuation in energy levels is given as

$$\begin{aligned} \Delta E &= \left(\frac{dE}{dL^*}\right)\Delta L^* \\ &= \frac{\hbar^2}{m}\left(\frac{\pi^2}{L^{*3}}\right)\Delta L^* \\ &= \frac{2\Delta L^*}{L^*}(E - Eg), \end{aligned}$$

where Eg is the band gap of GaAs. Thus, energy broadening ΔE induced by the fluctuation ΔL^* increases drastically when L^* decreases, leading to the degradation of

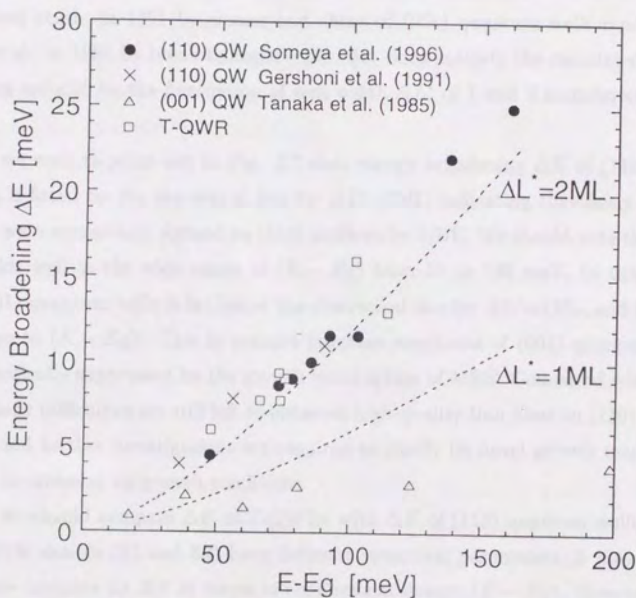

Figure 3.7: Energy broadening ΔE was plotted as a function of confinement energy $(E - Eg)$, where E is photoluminescence peak energy and Eg is the band gap of GaAs. Photoluminescence linewidths of QW2 are shown by solid circles, T-QWRs (S1 and S2) by blank squares, (110) quantum wells of Gershoni et al. by crosses, (001) quantum wells of Tanaka et al. by blank triangles, respectively. Two dot lines indicate the calculated energy broadening induced by the fluctuation of well width ΔL^{*} of 1 and 2 monolayers of GaAs.

photoluminescence linewidth.

To see such effects, we plot in Fig. 3.7 energy broadening ΔE as a function of confinement energy $(E - Eg)$, where photoluminescence linewidths of QW2 and those of T-QWRs (S1 and S2) are shown by solid circles and blank squares, respectively. For comparison, we also show photoluminescence linewidths of (110) quantum wells reported by Gershoni et al. in 1991 by crosses and those of (001) quantum wells reported by Tanaka et al. in 1985 by blank triangles. Two dot lines indicate the calculated energy broadening induced by the fluctuation of well width ΔL^* of 1 and 2 monolayers (MLs) of GaAs.

First, we wish to point out in Fig. 3.7 that energy broadening ΔE of (110) quantum wells is fitted by the theoretical line for ΔL^*=2ML, indicating that fairly smooth interfaces were successfully formed on (110) surfaces by MBE. We should note that such fitting holds well in the wide range of $(E - Eg)$ from 50 to 150 meV. In this range, ΔE of (001) quantum wells is far below the theoretical line for ΔL^*=1ML, and it is not so sensitive to $(E - Eg)$. This is because interface roughness of (001) quantum wells can be drastically suppressed by the growth interruption of MBE. Compared with (001) surface, many difficulties are still left to obtained high-quality thin films on (110) surface by MBE, and further investigations are required to clarify its novel growth mechanism as well as to optimize its growth conditions.

Then, we should compare ΔE of T-QWRs with ΔE of (110) quantum wells. Since each T-QWR sample (S1 and S2) have different structural parameters, it may not be adequate to compare its ΔE in terms of confinement energy $(E - Eg)$. However, it is interesting to point out in Fig. 3.7 that T-QWRs show almost the same ΔE as (110) quantum wells with the same confinement energy $(E - Eg)$.

Next, we will discuss energy broadening ΔE as a function of QW2 thickness b. In Fig. 3.6, the slope of the energy level of T-QWRs and that of QW2 against b give the energy broadening ΔE induced by the fluctuation of the QW2 thickness b. The slope of T-QWRs is smaller than that of QW2 with the same thickness b, showing that T-QWRs are less affected by b than QW2. Fitting the data points with a linear relation, we obtain the energy broadening of T-QWRs at $b = a$ to be 3.4 and 7.0 meV/ML (1 ML = 0.283 nm) for S1 and S2, respectively. These two values give the reasonable estimation that the observed photoluminescence linewidth of T-QWRs corresponds to about 2 monolayer

fluctuation of b.

Lateral confinement energy

The effective lateral confinement energy of excitons E^*_{1D-2D} is a key parameter to characterize lateral confinement of T-QWRs, as discussed in §2.2 and §3.1. Note that E^*_{1D-2D} represents the stability of excitons confined in T-QWRs. One can easily evaluate in Fig. 3.6 the effective lateral confinement energy of excitons E^*_{1D-2D} as the spacing between photoluminescence energy of T-QWRs and that of QW1 and QW2. In Fig. 3.8, we plot E^*_{1D-2D} as a function of the QW2 thickness b.

First, it is found in Fig. 3.8 that E^*_{1D-2D} of S1 reaches a maximum value of 18 meV at b=5.1 nm, where the energy levels of QW1 and QW2 are the same, indicating that a well-stabilized one-dimensional state is realized. Then, E^*_{1D-2D} decreases and approaches zero as the thickness b decreases or increases away from 5.1 nm. The decrease in E^*_{1D-2D} demonstrates how the T-QWR states become deviated from the well-stabilized one-dimensional state and takes on a two-dimensional character. When the energy difference between QW1 and QW2 is so large that E^*_{1D-2D} is close to zero, the influence of the higher energy quantum well can be regarded as a weak perturbation. In such regions, the T-QWR state is regarded as two-dimensional state. In this way, E^*_{1D-2D} represents the dimensionality of the excitons confined in T-QWRs. Hence, we conclude that the dimensional crossover from one-dimensional states to two-dimensional states is observed in Fig. 3.8 via the effective lateral confinement energy E^*_{1D-2D} for T-QWRs with various b.

Similar tendency is also observed in S2. When the energy levels of QW1 and QW2 coincide, E^*_{1D-2D} gets maximum and reaches as large as 38 meV, which is beyond the thermal energy kT at 300 K. This result indicates some possibilities that most electrons and holes may be accommodated in the ground state of T-QWRs even at room temperature. Comparing S2 with S1, it is clear that the increase of E^*_{1D-2D} in T-QWR is possible when one reduces the size of quantum wire and enlarges the barrier height at the same time. Thus, this large E^*_{1D-2D} is due to the introduction of high AlAs barriers and shows the feasibility of stable one-dimensional states at 300 K.

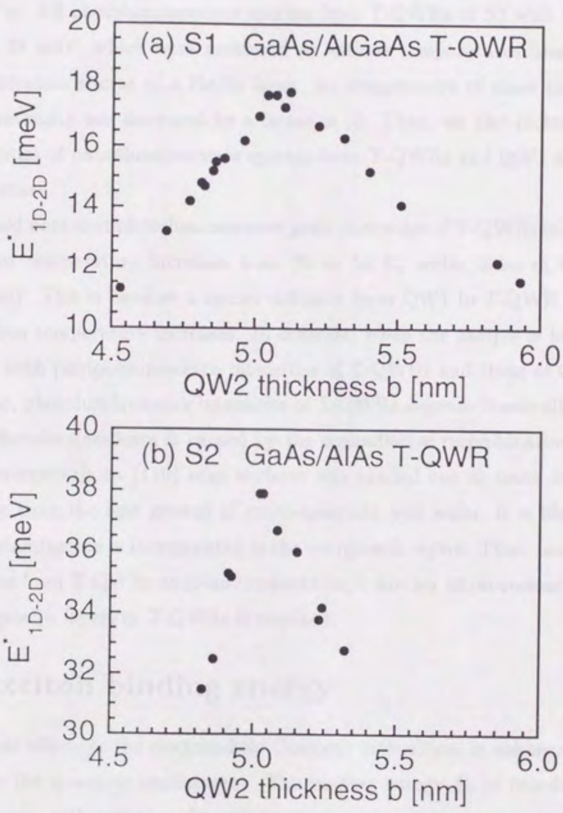

Figure 3.8: The effective lateral confinement energy E^{*}_{1D-2D}, defined as the energy difference between the lowest one-dimensional exciton energy in T-QWRs and the lowest two-dimensional exciton energy in QW1 and QW2, plotted against the QW2 thickness b.

Temperature dependence of photoluminescence

To discuss the stability of quantum wire states and the quality of quantum wire samples, we should present the temperature dependence of photoluminescence spectra. We have shown in Fig. 3.9 photoluminescence spectra from T-QWRs of S2 with the maximized E^*_{1D-2D} of 38 meV, which were measured at various temperatures from 10 to 240 K with an excitation source of a He-Ne laser. At temperature of more than 100 K, the excitation intensity was increased by a factor of 10. Then, we also plotted in Fig. 3.10 peak intensities of photoluminescence spectra from T-QWRs and QW1 as a function of the temperature.

We should note that photoluminescence peak intensities of T-QWRs increase monotonously when temperature increases from 10 to 50 K, while those of QW1 decrease monotonously. This is because a carrier diffusion from QW1 to T-QWR becomes quite effective when temperature increases. In contrast, when the sample is heated up more than 60 K, both photoluminescence intensities of T-QWRs and those of QW1 decrease. In particular, photoluminescence intensities of T-QWRs degrade drastically. Such degradation of photoluminescence is caused by the nonradiative recombination in T-QWRs. Since the overgrowth on (110) edge surfaces was carried out at much lower substrate temperature than the first growth of multi-quantum well wafer, it is likely that much residual contamination is incorporated in the overgrowth layers. Thus, to observe photoluminescence from T-QWRs at room temperature, a further improvement of the quality of the overgrowth layers in T-QWRs is required.

3.4 Exciton binding energy

The excitonic effect, or the electron-hole Coulomb interaction, is enhanced in quantum wells due to the quantum confinement. The binding energy E_b of two-dimensional excitons increases, with reducing the well thickness, up to four times as large as the bulk value (4.2 meV in GaAs) [19–23]. In quantum wires, the excitonic effect is potentially further enhanced [24] by laterally compressing wave functions into the nanometer-scale regime. Due to the good controllability of the cleaved-edge overgrowth method, we have fabricated a series of 5-nm-scale T-QWRs and precisely characterized their structures and energy levels, as shown in Fig. 3.6. Based on such a systematic study, we investigate

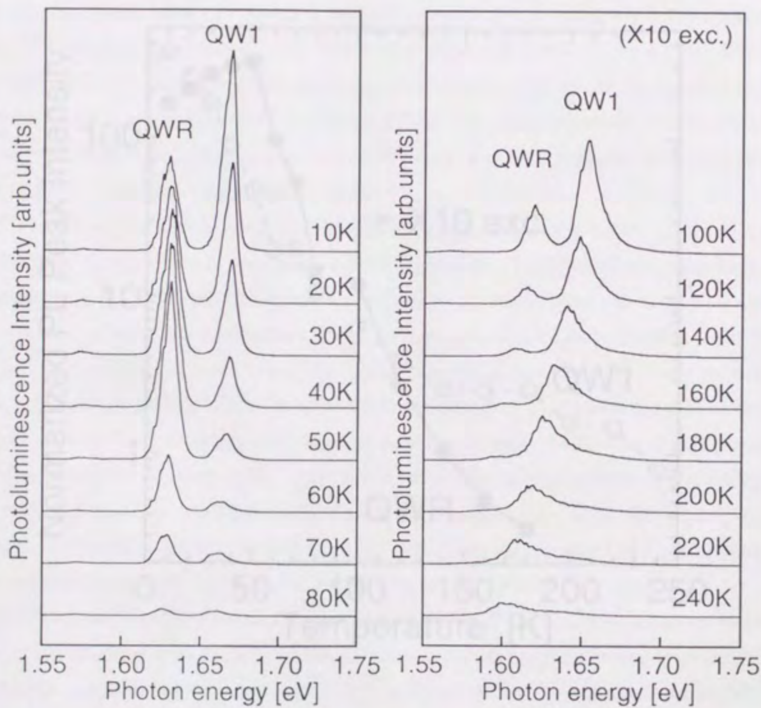

Figure 3.9: The temperature dependence of photoluminescence spectra from T-shaped GaAs quantum wires with AlAs barriers (S2).

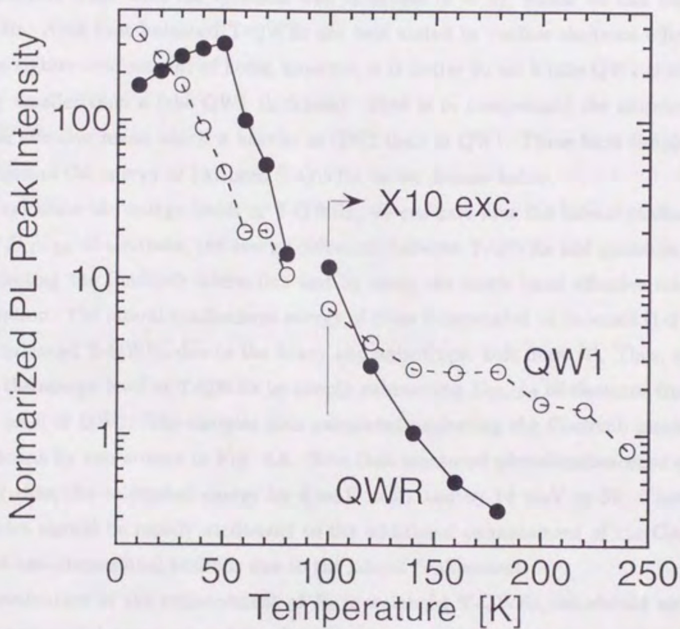

Figure 3.10: Peak intensities of photoluminescence from T-QWRs are plotted as a function of temperature. At temperature of more than 100 K, the excitation intensity was increased by a factor of 10.

in this section the enhanced Coulomb interaction in one-dimensional systems.

Evaluation of exciton binding energy

We will estimate the exciton binding energy E_b in T-QWRs by comparing experimental data in Fig. 3.6 with the calculation. For simplicity, we examine T-QWRs formed by two quantum wells with the identical well thickness ($b = a$), which we call balanced T-QWRs. Note that balanced T-QWRs are best suited to confine electrons efficiently. For the tighter confinement of holes, however, it is better to set b (the QW2 thickness) slightly smaller than a (the QW1 thickness). That is to compensate the anisotropy of the hole effective mass, which is heavier in QW2 than in QW1. These facts simplify the evaluation of the energy of balanced T-QWRs, as we discuss below.

To calculate the energy levels of T-QWRs, we evaluate first the lateral confinement energy E_{1D-2D} of electrons, the energy difference between T-QWRs and quantum wells, by neglecting the Coulomb interaction and by using the single band effective mass approximation. The lateral confinement energy of holes is estimated to be small (1-2 meV) in the balanced T-QWRs due to the heavy and anisotropic hole mass [7]. Thus, we can obtain the energy level of T-QWRs by simply subtracting E_{1D-2D} of electrons from the energy level of QW2. The energies thus calculated neglecting the Coulomb interaction are denoted by two crosses in Fig. 3.6. Note that measured photoluminescence energy is lower than the calculated energy by 4 meV in S1 and by 14 meV in S2. These discrepancies should be mostly attributed to the additional enhancement of the Coulomb effect of one-dimensional excitons due to the lateral confinement.

In evaluation of the enhancement of E_b in balanced T-QWRs, we should estimate that experimental errors caused by the broadening of photoluminescence spectra are about ± 2 meV and theoretical errors caused by the neglected contribution of holes are -1 ± 1 meV. Therefore, we conclude that the additional enhancement of E_b due to the lateral confinement are 3 ± 3 meV for S1 and 13 ± 3 meV for S2. If we assume E_b in 5-nm-thick GaAs quantum wells to be 14 meV as reported, the binding energy E_b of one-dimensional excitons in balanced T-QWRs is concluded to be 17 ± 3 meV for S1, and 27 ± 3 meV for S2. Note that E_b of S2 is about 6-7 times larger than the bulk value. We believe that this is the first clear demonstration of the enhanced Coulomb interaction in semiconductor quantum wires with the binding energy far exceeding that of quantum

wells.

Here, we examine the validity of our calculation to evaluate E_{1D-2D} of electrons on the basis of the present material parameters. It is possible to select other sets of material parameters and/or more sophisticated models, including the band non-parabolicity and other effects, for the estimation of well thickness with one monolayer accuracy and for the succeeding calculation of E_{1D-2D}. However, the evaluation of E_{1D-2D} of electrons is not sensitive to those variations of parameters. For example, E_{1D-2D} of electrons in S2 is changed only by less than 1 meV, when the electron mass changes from $0.067m_0$ to $0.070m_0$, the conduction band offset varies from 1.036 to 1.116 eV, or the well thickness is altered from 5.30 to 5.44 nm. Note that effects of the valence-band parameters such as masses, offsets, and band-nonparabolicity are counted in the estimation of E_{1D-2D} of electrons only implicitly through the well thickness, as we have already discussed. Hence, the calculation of E_{1D-2D} of electrons is sufficiently accurate and the comparison with experiment can be done with the ± 3 meV accuracy.

Enhancement of exciton binding energy

We should note that the additional enhancement of E_b due to the lateral confinement is significant (13 meV) in S2, whereas it is rather small (3 meV) in S1. Since S1 and S2 have almost the same well thickness ($a = b = 5.3 \sim 5.4$ nm), the difference in the enhancement of E_b is mainly due to the barrier height difference, indicating the importance of very tight confinement.

To explain this situation more clearly, we plot in Fig. 3.11 the lateral confinement energies as a function of the photoluminescence energy of QW2. Two solid circles represent the effective lateral confinement energies E^*_{1D-2D} measured in our balanced T-QWRs of series S1 and S2. For comparison, we have shown by solid or broken lines in Fig. 3.11 the theoretical lateral confinement energy E_{1D-2D} of electrons, which is calculated by Pfeiffer et al. for the barrier height of 245, 355, 500 meV [7], and infinity. We show also by crosses the theoretical values of E_{1D-2D} of electrons calculated for our samples. Note in Fig. 3.11 that calculated E_{1D-2D} of electrons increases linearly when the barrier height is infinite ($V_0 = \infty$), but it rises only sublinearly with the QW2 energy when V_0 is finite. The experimental data indicated by solid circles, however, show a superlinear dependence, which indicates that the Coulomb interaction becomes increasingly

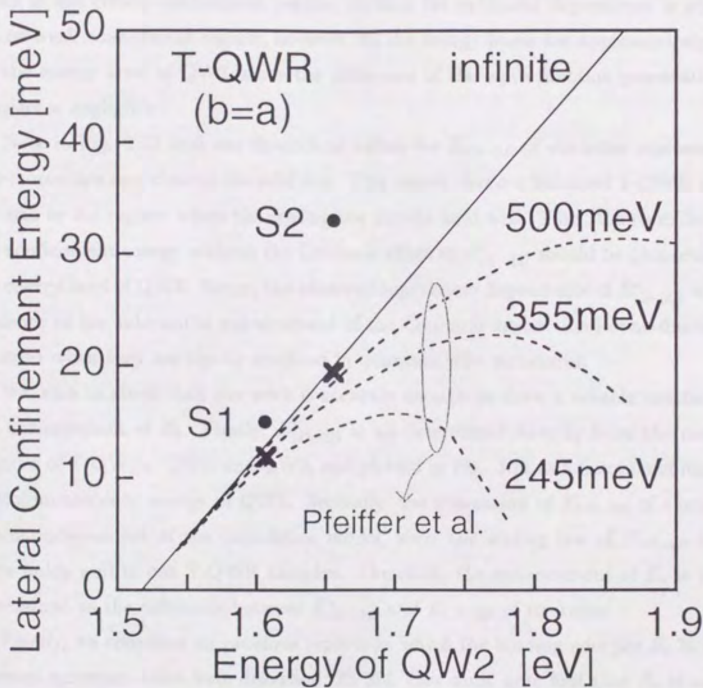

Figure 3.11: The lateral confinement energy in T-QWRs formed by two quantum wells with the identical well thickness is shown as a function of the energy of QW2. The effective lateral confinement energy of excitons (E^{*}_{1D-2D}) shown by solid circles is compared with the lateral confinement energy E_{1D-2D} of electrons (the broken or solid lines) for 245, 355, 500 meV, and infinite barriers, calculated by Pfeiffer et al.

important.

In the case of infinite barriers, both the energy level of balanced T-QWRs and that of QW2 are scaled by b^{-2}. As a result, E_{1D-2D} of electrons is scaled by the energy level of QW2, which gives the linear dependence as shown in Fig. 3.11. For finite barriers, the portion of wave function penetration into barriers becomes larger for T-QWR than for QW2 in the strong confinement regime, so that the sublinear dependence is obtained. In the weak confinement regime, however, all the energy levels are approximately scaled by the energy level of QW2, since the difference of the wave function penetration into barriers is negligible.

Note in Fig. 3.11 that our theoretical values for E_{1D-2D} of electrons represented by two crosses are very close to the solid line. This means that our balanced T-QWR samples are still in the regime where the scaling law should hold well. Thus, the contribution of the confinement energy without the Coulomb effect to E^*_{1D-2D} should be proportional to the energy level of QW2. Hence, the observed superlinear dependence of E^*_{1D-2D} is a clear evidence of the substantial enhancement of the Coulomb interaction in one-dimensional excitons when they are tightly confined in quantum wire structures.

We wish to stress that our work is accurate enough to draw a reliable conclusion on the enhancement of E_b. Firstly, E^*_{1D-2D} is all determined directly from the measured energies of T-QWRs, QW1, and QW2, and plotted in Fig. 3.11 as a function of measured photoluminescence energy of QW2. Secondly, the evaluation of E_{1D-2D} of electrons is almost independent of the calculation model, since the scaling law of E_{1D-2D} of electrons holds well in our T-QWR samples. Therefore, the enhancement of E_b is reliably determined as the difference between E^*_{1D-2D} and E_{1D-2D} of electrons.

Finally, we comment on previous reports in which the binding energies E_b in several different quantum wires were discussed [25–29]. One must note first that E_b of excitons in large quantum wires was reported to be almost the same as that of two-dimensional excitons in quantum wells [25–27]; this is consistent with our results on series S1 of T-QWRs with $Al_{0.3}Ga_{0.7}As$ barrier. In some work, the enhancement of E_b was said to be realized even when quantum wires are larger than our S1 samples. In these reports [28, 29], however, the reduced diamagnetic shifts of photoluminescence were analyzed on the basis of the hydrogen-like exciton model assuming anisotropic reduced mass. Such an analysis has attributed the squeezing of exciton wave function totally to the enhanced

Coulomb effect despite the importance of the lateral confinement, and has resulted in the overestimation of E_b. We emphasize here that tight one-dimensional confinement comparable with S2 is required to demonstrate the noticeable enhancement of E_b for one-dimensional excitons in semiconductor quantum wire structures.

3.5 T-shaped InGaAs quantum wires

So as to enhance the stability of one-dimensional states, it is essential to realize strong lateral confinement. We have shown in §3.3 that such strong confinement can be achieved in T-QWRs when one reduces the size of quantum wire and enlarges the barrier height at the same time. Indeed, tightly confined one-dimensional states were demonstrated in 5-nm-scale GaAs T-QWRs with AlAs barriers, in which the effective lateral confinement energy E^*_{1D-2D} reaches as large as 38 meV. One should note that this value goes beyond the thermal energy kT ($\sim$ 26 meV) at room temperature. However, to accommodate most electrons and holes in the ground state of T-QWRs even at room temperature, it is desirable to further enhance the lateral confinement energy E^*_{1D-2D} up to $2 \sim 3kT$. Furthermore, $Al_xGa_{1-x}As$ barriers with high aluminum composition x such as AlAs should be avoided for device applications. This is partly because thick AlAs layers tend to accumulate interface roughness and defects and mainly because AlAs has a low index of refraction. The active region of semiconductor laser is the narrow channel waveguide surrounded by a compositionally different material with a lower index of refraction. Therefore, T-QWRs with AlAs barriers make it difficult to design the index-guided active region of lasers. To avoid such problems, we fabricated T-QWRs with In(Ga)As/Al(Ga)As material systems and characterized the effective lateral confinement energy E^*_{1D-2D} with the spatially-resolve photoluminescence technique.

Sample preparation

We have prepared a set of three $In_{0.07}Ga_{0.93}As$ T-QWR samples (B1 $\sim$ B3) and an $In_{0.13}Ga_{0.87}As$ T-QWR sample (B4), whose schematic structures are shown in the insets of Fig. 3.12. Wafers with QW1 of B1, B2 , and B3 were grown simultaneously in the first growth, where we grew a 500 nm GaAs buffer layer, a 5 μm $Al_{0.3}Ga_{0.7}As$ layer, an InGaAs multi-quantum well layer (QW1) with $Al_{0.3}Ga_{0.7}As$ barriers, a 10 nm AlAs

layer, a 5 μm $Al_{0.3}Ga_{0.7}As$ layer, a 10 nm AlAs layer, and a 500 nm GaAs cap layer. A multi-quantum well layer (QW1) consisted of 10 periods of 100 nm $Al_{0.3}Ga_{0.7}As$ and 4.0 nm $In_{0.07}Ga_{0.93}As$. The thickness of quantum well is not nominal thickness, but is determined by comparing the observed photoluminescence peak with the calculation, whose details will be given in Appendix B.

Then, we carried out *in situ* cleavage and grew on the edge surface $In_{0.07}Ga_{0.93}As$ quantum well layer of thickness b and 2 monolayer $Al_{0.3}Ga_{0.7}As$ at the substrate temperature of 430 °C. The growth rate of InGaAs was 0.5 μm/hr, and the V/III flux ratio was 30. The QW2 thickness b is 4.5 nm for B1, 4.0 nm for B2, and 3.6 nm for B3. Finally, samples were heated up to 500 °C for deposition of a 10 nm $Al_{0.3}Ga_{0.7}As$ barrier layer and a 10 nm GaAs cap layer.

In this way, after the cleaved-edge overgrowth, we obtained an array of 10 periods of T-QWRs and two 5-μm-wide QW2 layers which can be easily studied by a spatially-resolved photoluminescence measurement. The 10 nm AlAs layers, which are indeed 5-nm-AlAs/1-nm-GaAs/5-nm-AlAs, were grown on both sides of the thick AlGaAs layer to reduce the carrier diffusion.

The fundamental sample structure of B4 is the same as B1, but T-QWRs of B4 were formed by 3.5-nm-thick $In_{0.13}Ga_{0.87}As$ QW1 and 3.5-nm-thick $In_{0.13}Ga_{0.87}As$ QW2.

Photoluminescence study

We performed spatially-resolved photoluminescence measurements. Photoluminescence from B1 was studied at 4 K using a He-Ne laser (λ=633 nm) as an excitation source. We obtained photoluminescence spectra as shown in Fig. 3.12 (a), when the excitation laser of 2 μm in diameter was scanned from on the surface (spot d of the inset) to on the substrate (spot c of the inset) of the sample with a step of 1 μm. Four photoluminescence peaks were clearly observed and their origins were determined as shown in Fig. 3.12 (a). The highest energy peak was attributed to QW1, since the multi-quantum well wafer (QW1) without overgrowth showed the same peak. The lowest energy peak comes from InGaAs quantum wells whose barrier layers consisted of an overgrown AlGaAs layer and a GaAs of the substrate (spot c of the inset). On the other hand, the two middle energy peaks were ascribed to T-QWR and QW2, respectively. Curve a of Fig. 3.12 (a) was obtained when the excitation laser beam was incident onto the T-QWR region (spot a of

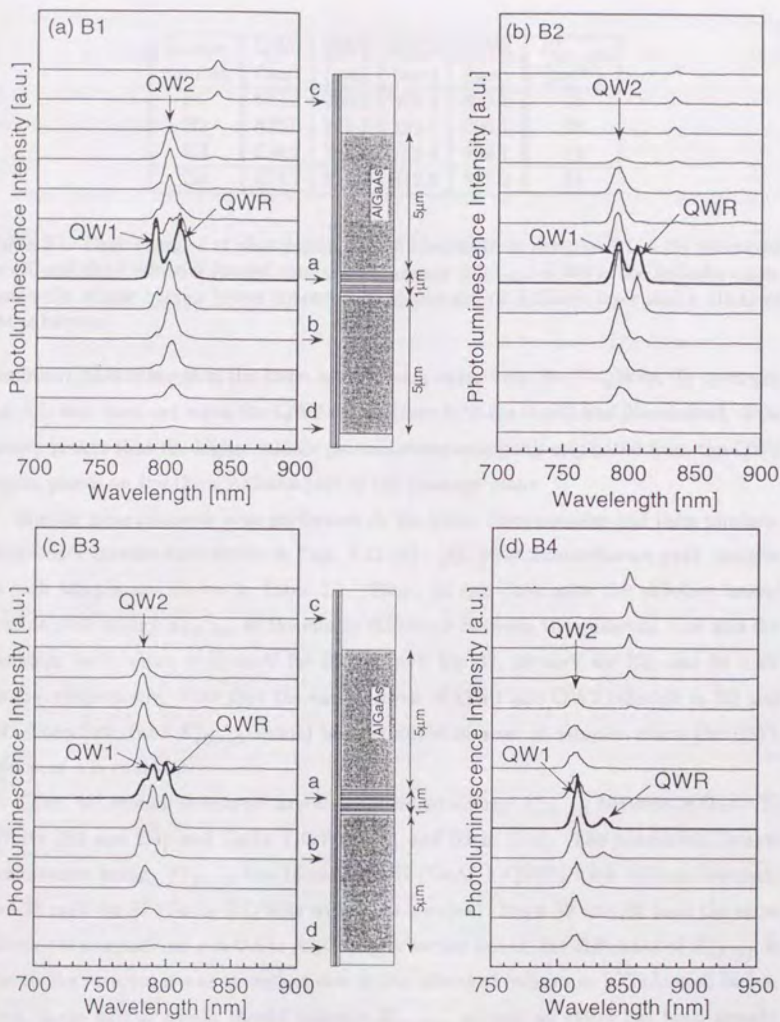

Figure 3.12: Spatially-resolved photoluminescence spectra from B1 (a), B2 (b), B3 (c), and B4 (d) measured at 4 K.

Sample number	QW0 (nm)	QW1 (nm)	QW2 (nm)	QWR (nm)	E^{*}_{1D-2D} (meV)
B1	837.3	790.3	801.4	809.7	15
B2	833.0	791.1	791.1	805.1	28
B3	828.7	788.9	782.4	799.1	19
B4	853.7	815.7	812.9	835.2	34

Table 3.1: Peak energies of photoluminescence spectra from samples B1 ~ B4 measured at 4K and their effective lateral confinement energy E^{*}_{1D-2D}. QW0 is the InGaAs quantum wells whose barrier layers consisted of an overgrown AlGaAs layer and a GaAs of the substrate.

the inset), indicating that the lower middle peak came from the T-QWRs. In contrast, curve b was observed when the QW2 region (spot b in the inset) was illuminated. This clearly proves that the higher middle photoluminescence peak originated from the QW2 region grown on the thick AlGaAs part of the cleavage plane.

Similar measurements were performed on the other three samples and their photoluminescence spectra were shown in Figs. 3.12 (b) - (d). Photoluminescence peak energies in each sample are shown in Table 3.1. Thus, we can determine the effective lateral confinement energy E^{*}_{1D-2D} as the energy difference between the quantum wire and the quantum well, which is 15 meV for B1, 28 meV for B2, 19 meV for B3, and 34 meV for B4, respectively. Note that the energy levels of QW1 and QW2 coincide in B2 and B4. Therefore, their E^{*}_{1D-2D} should be maximized in a set of samples where the QW1 thickness a is constant.

Then, we should compared lateral confinement energy E^{*}_{1D-2D} between InGaAs T-QWRs (B2 and B4) and GaAs T-QWRs (S1 and S2 in §3.3). The maximized lateral confinement energy E^{*}_{1D-2D} was 18 meV for S1 (GaAs T-QWRs with AlGaAs barriers) and 38 meV for S2 (GaAs T-QWRs with AlAs barriers). Since S2 and B2 have the same aluminum composition $x = 0.3$ in $Al_xGa_{1-x}As$ barrier layers, the difference of E^{*}_{1D-2D} is due to the structural size as well as due to the effects of indium in InGaAs well layers; First, large barrier height should enhance E^{*}_{1D-2D}, as such an effect has been already demonstrated in S1 and S2. Second, the strain effect is also considered to enhance E^{*}_{1D-2D}. Since the lattice constant of InGaAs is slightly larger than that of GaAs, bandgap of the overgrown InGaAs layer is smaller on the cleaved edge of InGaAs well

layers than on the cleaved edge of AlGaAs barrier layers. Such a local modulation due to the strain contributes to realize stronger lateral confinement. However, the quantitative analysis to separate the effect of barrier height and that of strain needs the sophisticated theoretical treatment of local strains, which should be the important subject of the future study.

Next point to be noted is that lateral confinement energy E^*_{1D-2D} of B4 (34 meV) is larger than E^*_{1D-2D} of B2 (28 meV). This enhancement is caused by reducing the structural size from a=4.0 to 3.5 nm as well as by increasing the indium composition x in $In_xGa_{1-x}As$ well layers from 0.07 to 0.13. In this way, we have successfully demonstrated large E^*_{1D-2D} beyond thermal energy at room temperature without AlAs barriers, which would make it possible to exploit the stable one-dimensional states for the advanced optical devices. However, lateral confinement energy E^*_{1D-2D} of 34 meV obtained in B4 is still comparable to E^*_{1D-2D} of S2 (38 meV). Thus, continuous efforts are required to further enhance E^*_{1D-2D} up to $2\sim3kT$.

3.6 Summary

We presented our spatially-resolved photoluminescence study of T-QWRs in this chapter. Especially, we emphasized the importance of characterizing photoluminescence spectra not only from T-QWRs but also from the adjacent quantum wells, QW1 and QW2.

First, novel sample structures were designed and fabricated to detect the photoluminescence from the overgrown quantum wells in spite of the efficient carrier diffusion from QW2 to T-QWRs. On two types of such samples, spatially-resolved photoluminescence measurements were performed, and the energy levels of QW1, QW2, and T-QWRs were precisely determined. As a result, we determined the effective lateral confinement energy of excitons E^*_{1D-2D} as energy difference between quantum wires and quantum wells.

Then, we prepared a series of 5-nm-scale T-QWRs and characterize them from spatially-resolved photoluminescence. It is demonstrated that the effective lateral confinement energy of excitons E^*_{1D-2D} becomes as large as 38 meV in T-QWRs with AlAs barriers. We have found that such a strong lateral confinement enhances the binding energy E_b of one-dimensional excitons up to 27$\pm$3 meV, which is far beyond the theoretical limit for two-dimensional excitons in GaAs quantum wells (17 meV), and becomes

6-7 times larger than the bulk value (4.2 meV).

Bibliography

[1] J. Christen, M. Grundmann, and D. Bimberg, J. Vac. Sci. Technol. **B9**, 2358 (1991), and references therein.

[2] R. D. Grober, T. D. Harris, J. K. Trautman, E. Benzig, W. Wegscheider, L. N. Pfeiffer, and K. W. West, Appl. Phys. Lett. **64**, 1421 (1994).

[3] T. D. Harris, D. Gershoni, R. D. Grober, W. Wegscheider, L. N. Pfeiffer, and N. Chand, Appl. Phys. Lett. **68**, 988 (1996).

[4] A. Zrenner, L. V. Butov, M. Hagn, G. Abstreiter, G. Böm, and G. Weimann, Phys. Rev. Lett, **72**, 3382 (1994).

[5] J.-Y. Marzin, J.-N. Gérard, A. Izraël, D. Barrier, and G. Bastard, Phys. Rev. Lett. **73**, 716 (1994).

[6] M. Grundmann, J. Christen, N. N. Ledenstov, J. Böhrer, D. Bimberg, S. S. Ruvimov, P. Werner, U. Richter, U. Gösele, J. Heydenreich, V. M. Ustinov, A. Yu. Egorov, A. E. Zhukov, P. S. Kop'ev, and Zh. I. Alferov, Phys. Rev. Lett. **74**, 4043 (1995).

[7] L. N. Pfeiffer, H. Baranger, D. Gershoni, K. Smith, and W. Wegscheider, in *Low Dimensional Structures Prepared by Epitaxial Growth or Regrowth on Patterned substrates*, edited by K. Eberl, et al., NATO ASI, Ser. E, Vol. 298 (Kluwer Academic Publishers, Dordrecht, 1995), p. 93.

[8] A. A. Kizelev and U. Rösssler, Semicond. Sci. Technol. **11**, 203 (1996).

[9] Chapter 3, and references therein.

[10] Chapter 4, and references therein.

[11] D. S. Citrin, Phys. Rev. Lett. **69**, 3393 (1992).

[12] H. Akiyama, S. Koshiba, T. Someya, K. Wada, H. Noge, Y. Nakamura, T. Inoshita, A. Shimizu, and H. Sakaki, Phys. Rev. Lett. **72**, 924 (1994).

[13] D. Gershoni, M. Katz, W. Wegscheider, L. N. Pfeiffer, R. A. Logan, and K. West, Phys. Rev. B**50**, 8930 (1994).

[14] A. Shimizu, T. Ogawa, and H. Sakaki, Phys. Rev. B**45**, 11338 (1992).

[15] R. Cingolani, M. Lepore, R. Tommasi, I. M.h Catalona, H. Lage, D. Heitmann, K. Ploog, A. Shimizu, H. Sakaki, and T. Ogawa, Phys. Rev. Lett. **69**, 1276 (1992).

[16] R. Cingolani, M. Lepore, R. Tommasi, I. M. Catalona, H. Lage, D. Heitmann, K. Ploog, A. Shimizu, H. Sakaki, and T. Ogawa, Superlattices and Microstruc. **13**, 71 (1993).

[17] R. Dingle, W. Wiegmann, and C. H. Henry, Phys. Rev. Lett. **33**, 827 (1974).

[18] R. C. Miller, D. A. Kleinman, and A. C. Gossard, Phys. Rev. B**29**, 7085 (1984).

[19] R. C. Miller, D. A. Kleinman, W. T. Tang, and A. C. Gossard, Phys. Rev. B**24**, 1134 (1981).

[20] G. Bastard, E. E. Mendez, L. L. Chang, and L. Esaki, Phys. Rev. B**26**, 1974 (1982).

[21] J. C. Maan, G. Belle, A. Fasolino, M. Altarelli, and K. Ploog, Phys. Rev. B**30**, 2253 (1984).

[22] S. Tarucha, H. Okamoto, Y. Iwasa, and N. Miura, Solid State Commun. **52**, 815 (1984).

[23] R. L. Greene, K. K. Bajaj, and D. E. Phelps, Phys. Rev. B**29**, 1807 (1984).

[24] T. Ogawa and T. Takagahara, Phys. Rev. B**43**, 14325 (1991); **44**, 8138 (1991).

[25] M. Kohl, D. Heitmann, P. Grambow, and K. Ploog, Phys. Rev. Lett. **63**, 2124 (1989).

[26] A. S. Plaut, H. Lage, P. Grambow, D. Heitmann, K. von Klitzing, and K. Ploog, Phys. Rev. Lett. **67**, 1642 (1991).

[27] R. Rinaldi, R. Cingolani, M. Lepore, M. Ferrara, I. M. Catalano, F. Rossi, L. Rota, E. Molinari, P. Lugli, U. Marti, D. Martin, F. Morier-Gemoud, P. Ruterana, and F. K. Reinhart, Phys. Rev. Lett. **73**, 2899 (1994).

[28] Y. Nagamune, Y. Arakawa, S. Tsukamoto, M. Nishioka, S. Sasaki, and N. Miura, Phys. Rev. Lett. **69**, 2963 (1992).

[29] Y. Nagamune, T. Tanaka, T. Kono, S. Tsukamoto, M. Nishioka, Y. Arakawa, K. Uchida, and N. Miura, Appl. Phys. Lett. **66**, 2502 (1995).

Chapter 4

Polarization properties and oscillator strength

4.1 Introduction

Polarization properties and oscillator strength of one-dimensional states have been important subjects in the optical properties of quantum wires. It is expected that such properties are drastically and favorably modulated by lateral confinement. Reflecting the anisotropic electronic states induced by lateral confinement, quantum wire states should be polarized more along the wire, which can be measured via the polarization dependence of optical absorption and/or emission. Oscillator strength of one-dimensional excitons should be concentrated into the lowest exciton state in quantum wires due to the one-dimensional electronic density-of-states.

We present, in this chapter, our detailed measurements of photoluminescence and photoluminescence excitation spectra, where polarization and relative intensities are carefully analyzed. First, the polarization dependence of photoluminescence and photoluminescence excitation spectra was measured on 5-nm-scale T-shaped quantum wires (T-QWRs) and a reference quantum well grown on a (110) surface. Comparing the observed optical anisotropy for the T-QWRs and the reference quantum well, we evaluated the optical anisotropy induced by the lateral confinement in T-QWRs. Next, measuring the polarization-dependent photoluminescence on a series of T-QWRs, we investigate how the optical anisotropy in T-QWRs changes when the lateral confinement is systematically changed. Then, we present the structure dependence of photoluminescence excitation spectra for three typical T-QWR samples, from which oscillator strength of

one-dimensional exciton states is evaluated.

4.2 Optical anisotropy

Optical anisotropy has been one of the main subjects in quantum wires and other modulated semiconductor structures, because it directly reflects the anisotropic electronic states inherent to each structure. In fact, for most types of GaAs quantum wires so far reported, the polarization dependence of photoluminescence and photoluminescence excitation spectra has been presented as a proof of the electronic states resulting from lateral confinement [1–9]. However, the optical anisotropy introduced purely by the lateral confinement in quantum wires has hardly been evaluated nor theoretically reproduced [10–12].

First, the valence band anisotropy is sensitive to many factors; warping distortion, uniaxial strain, and anisotropic perturbation potential of anisotropic interface roughness [13]. In some quantum wires grown on patterned substrates, the anisotropy in macroscopic sample geometry also induces additional polarization dependence of their photoluminescence and photoluminescence excitation spectra. Furthermore, the spectral peaks tend to broaden and overlap with other spectral structures in nanometer-scale quantum wires, which makes it difficult to quantify the optical anisotropy from the photoluminescence and photoluminescence excitation spectra. For quantitative analysis of the observed anisotropy, one must accurately characterize both the potential profile and the quantized energy levels of quantum wires, which is often difficult. For such reasons, the quantitative investigation of the optical anisotropy has never been accomplished completely in nanometer-scale quantum wires whose potential were characterized well.

We present in this section the optical anisotropy measured in terms of the polarization dependence of photoluminescence and photoluminescence excitation spectra in 5-nm-scale T-shaped quantum wires (T-QWRs) and a reference quantum well grown on a (110) surface. Clear optical anisotropy was observed for the T-QWRs as well as for the constituent adjacent quantum wells forming T-structures and the reference (110) quantum well. Comparing the T-QWRs with the reference quantum well, we evaluated the optical anisotropy induced by the lateral confinement in T-QWRs.

Theory

In the III-V compound semiconductors like GaAs, the optical anisotropy is caused mainly by the anisotropic electronic states at the top of valence bands, which have total angular momentum of j=3/2 [14]. In quantum wires and quantum wells, the j=3/2 hole states are separated into heavy hole (HH) and light hole (LH) states to give pair optical transition with different energy into a conduction electron state. We use the term heavy hole (light hole) in the sense that it has heavier (lighter) effective mass than the other in the direction of the confinement of quantum wells and quantum wires.

Neglecting spin indices, the conduction-band Bloch function is expressed as $|s\rangle$, whereas the valence-band Bloch function $|v\rangle$ is expressed as

$$|v\rangle = C_X|X\rangle + C_Y|Y\rangle + C_Z|Z\rangle,$$

where $|X\rangle$, $|Y\rangle$, and $|Z\rangle$ have p-orbital symmetry. The optical transition probability is given by

$$\begin{aligned} W &= \frac{2\pi}{\hbar}|\langle s|\frac{e}{m}\boldsymbol{A}\cdot\boldsymbol{p}|v\rangle|^2\delta\{E_c - E_v - \hbar\omega\} \\ &= \frac{\pi e^2}{2\hbar m^2}A_0^2|M|^2\delta\{E_c - E_v - \hbar\omega\}, \end{aligned} \quad (4.1)$$

where $\boldsymbol{A}$=$A_0\boldsymbol{e}$ is the vector potential, and $\boldsymbol{p}$ is the momentum operator. Thus, the squared optical matrix element for transition between conduction states and valence states, which takes the form

$$|M|^2 = |\langle s|\boldsymbol{e}\cdot\boldsymbol{p}|v\rangle|^2, \quad (4.2)$$

describes the optical anisotropy. For example, when the polarization is parallel to x-direction, the photoluminescence intensity I_x is proportional to $|\langle s|x|v\rangle|^2 = |C_X|^2$.

We will start to consider the optical anisotropy from the simplest model neglecting the crystal anisotropy. In a quantum well with confinement in z-direction, the heavy hole states are mainly of Bloch states

$$-\frac{1}{\sqrt{2}}|(X+iY)\uparrow\rangle$$

$$\frac{1}{\sqrt{2}}|(X-iY)\downarrow\rangle$$

with z-component of angular momentum $j_z = \pm 3/2$, while the light hole states are mainly of Bloch states

$$-\frac{1}{\sqrt{6}}|(X+iY)\downarrow\rangle + \sqrt{\frac{2}{3}}|Z\uparrow\rangle$$

$$\frac{1}{\sqrt{6}}|(X-iY)\uparrow\rangle + \sqrt{\frac{2}{3}}|Z\downarrow\rangle$$

with $j_z = \pm 1/2$. As a result, the relative optical transition intensities of heavy hole states in quantum wells are calculated as $0 : 3$ for $I_z : I_x$.

In an ideal quantum wire with axial symmetry along x-direction neglecting crystal band anisotropy and asymmetric shape of a quantum wire, the heavy hole state in a quantum wire is of Bloch states

$$\sqrt{\frac{2}{3}}|X\uparrow\rangle + \frac{1}{\sqrt{6}}|(Y+iZ)\downarrow\rangle$$

$$\sqrt{\frac{2}{3}}|X\downarrow\rangle - \frac{1}{\sqrt{6}}|(Y-iZ)\uparrow\rangle$$

with x-component of angular momentum $j_x = \pm 1/2$, which gives the relative optical transition intensities of $1 : 4$ for $I_z : I_x$, that is $I_z / I_x = 25\%$.

When crystallographic anisotropy is introduced, the other states are mixed, which modifies the optical anisotropy. To see such effect, the crystal band anisotropy should be taken into account. For this purpose, Yamaguchi et al. calculated optical anisotropy of cylindrical quantum wires with infinite barriers [15]. When the quantum wire has axial symmetry along the [1-10] direction, the optical anisotropy ratio $I_{[001]}/I_{[1-10]}$ is calculated to be 34%. In contrast, it is $I_{[001]}/I_{[1-10]} = 86\%$ for (110) quantum well, as will be given in Appendix C.

Experiment

To study optical anisotropy, we prepared two samples; a T-QWR sample and a reference quantum well sample. The T-QWR sample is A2 described in §3.2. The multi-quantum well layer consists of $n=50$ periods of GaAs quantum wells (QW1; thickness $a=5.3$ nm) and AlAs barriers (thickness $c=50$ nm). The overgrown quantum well is of a GaAs layer (QW2; thickness $b=4.8$ nm), covered by an AlAs barrier layer. From the microphotoluminescence measurements, the energy levels of those structures were well char-

acterized and precisely determined as photoluminescence photon energy of respective peaks; They were 1.633 eV for T-QWR, 1.668 eV for QW1, and 1.680 eV for QW2.

We also prepared a reference quantum well on a (110) surface, which was consisted of a 5.4-nm-thick GaAs well layer and an $Al_{0.3}Ga_{0.7}As$ barrier layer.

In this chapter, we define the [001] (the first growth direction) as the z-direction, the [110] (the overgrowth direction) as the y-direction, and the [1-10] (the quantum wire direction) as the x-direction. We also denote polarization along [1-10] ([001]) as $\|$ ($\perp$), since [1-10] ([001]) is parallel (perpendicular) to the T-QWRs and the QW1 layers.

Then, we present our experimental setup to measure polarization-dependent photoluminescence and photoluminescence excitation spectra with a cw titanium sapphire laser, as shown in Fig. 4.1. The photoluminescence was detected via the (110) surface in the backward scattering geometry. The output light of the titanium sapphire laser was horizontally or perpendicularly polarized with a Fresnel-rhomb half-wave retarder and a Glan-Thomson prism. It was then partly reflected by a beam-splitter placed at 45°, and focused, in the normal incidence configuration, into less-than-2μm spot on the sample at 4 K in a cryostat (Oxford Instruments CF2102), which was monitored by CCD camera system. An objective lens for near-infrared region (Mitsutoyo M Plan NIR 50x), with nominal magnification factor of 50, working distance of 17 mm, and numerical aperture of 0.42, was used. The photoluminescence was collected by the same objective lens, partly reflected by another beam-splitter placed at nearly 0°, and led to a 10-cm double monochromator with a GaAs photo-multiplier. The signal was measured with the lock-in detection technique. A polarizer and a depolarizer were placed in front of the monochromator to analyze the polarization of the photoluminescence. The polarization dependence of photoluminescence and photoluminescence excitation was measurable by the usage of the depolarizer, near-infrared broad-band optics for all the polarization-sensitive elements, and the normal incidence configuration both at the sample and the second beam-splitter.

Results

Figure 4.2 (a) shows photoluminescence spectra of the T-QWR sample measured at 4 K with the photon energy of the excitation laser of 1.72 eV and the excitation power of 0.2 mW. The solid (broken) curve shows photoluminescence with $\|$ ($\perp$), that is, polarization

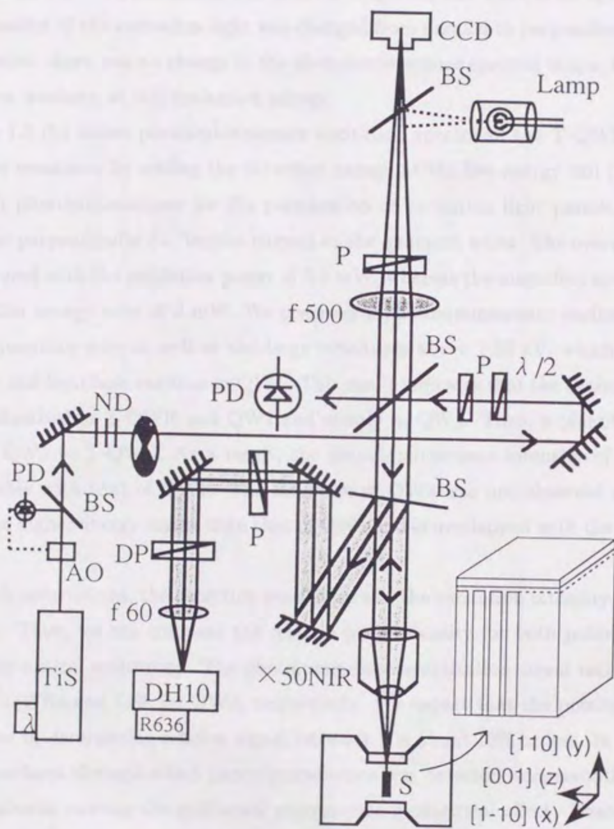

Figure 4.1: An experimental setup to measure spatially-resolved photoluminescence and photoluminescence excitation spectra in which polarization can be accurately analyzed.

parallel (perpendicular) to the T-QWRs and the QW1 layers. The two peaks are assigned to the lowest energy excitons in T-QWR and QW1. The photoluminescence signal ratio $I_{\perp}/I_{\parallel}$ between the two polarization was 20% for T-QWRs, and was 6% for QW1. When the polarization of the excitation light was changed from parallel to perpendicular to the quantum wire, there was no change in the photoluminescence spectral shape, that is, no polarization memory, at this excitation energy.

Figure 4.2 (b) shows photoluminescence excitation spectra of the T-QWR sample, which were measured by setting the detection energy at the low energy tail (1.625 eV) of T-QWR photoluminescence for the polarization of excitation light parallel ($\parallel$, solid curves) and perpendicular ($\perp$, broken curves) to the quantum wires. The overall spectra were measured with the excitation power of 0.2 mW, whereas the magnified spectra near the detection energy were of 2 mW. We observed a photoluminescence excitation peak from the quantum wire as well as the large structures above 1.66 eV, which were the heavy hole and light hole excitons in QW1. This result indicates that the excitation light is partly absorbed in T-QWR and QW2 and mostly in QW1. Then, a plentiful carrier flow from QW1 to T-QWR. As a result, the photoluminescence intensity of T-QWRs is comparable with that of QW1. The structure of QW2 was not observed since it is located at a higher energy region than that of QW1 and is overlapped with the structure of QW1.

For both polarization, the detection sensitivity and the excitation intensity were kept constant. Thus, we can compare the relative peak intensity for both polarization to evaluate the optical anisotropy. The photoluminescence excitation signal ratio $I_{\perp}/I_{\parallel}$ is 39% for T-QWRs and 14% for QW1, respectively. We expect that the possible experimental error in determining relative signal intensity I is about 10% or less. In addition, the (110) surfaces through which photoluminescence was detected were smooth and flat without patterns causing the additional macroscopic geometrical effect. Therefore, the signal ratio $I_{\perp}/I_{\parallel}$ shows the anisotropic electronic states in the lowest energy excitons in T-QWRs and in QW1, as will be discussed later.

Here, we should note the small Stokes shift and the sharp spectral linewidth. The values of the photoluminescence linewidth and the Stokes shift are 15 meV and 5 meV for T-QWRs, respectively, and 10 meV and 7 meV for QW1. These small values demonstrate the high quality of the sample, and thus support the reliability of the following

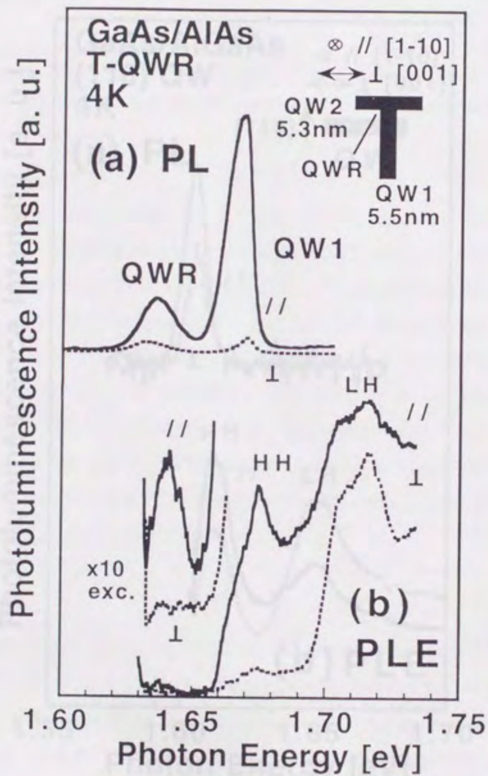

Figure 4.2: Photoluminescence and photoluminescence excitation spectra measured at 4 K for GaAs/AlAs T-QWRs.

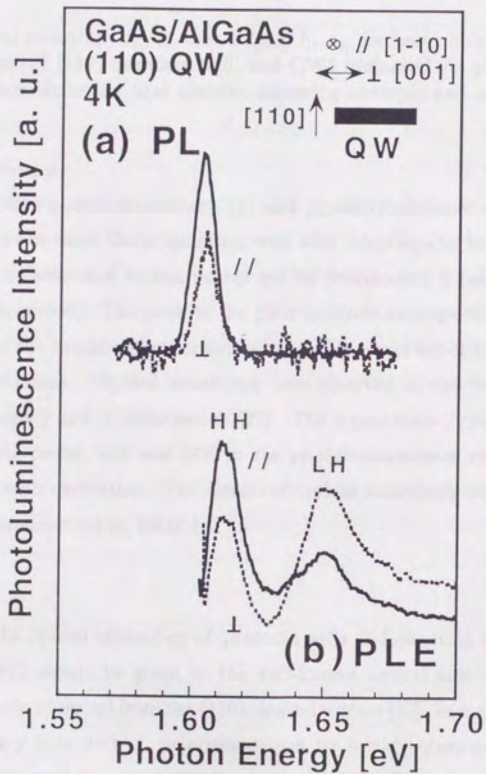

Figure 4.3: Photoluminescence and photoluminescence excitation spectra measured at 4 K for reference (110) quantum well.

sample	PLE (%)	PL (%)	theory1 (%) (isotropic)	theory2 (%) (anisotropic)
QWR	39	20	25	34
(110) QW	67	60	100	86
QW1	14	6	0	0

Table 4.1: Optical anisotropy $I_\perp/I_\parallel$, that is $I_{[001]}/I_{[1-10]}$, for heavy hole exciton transition in T-QWR, reference (110) quantum well, and QW1 evaluated via photoluminescence, photoluminescence excitation, and theories assuming isotropic and anisotropic valence band structures.

quantitative discussion.

Figure 4.3 shows photoluminescence (a) and photoluminescence excitation spectra (b) at 4 K of 5.4-nm-thick GaAs quantum well with $Al_{0.3}Ga_{0.7}As$ barrier formed on a (110) surface. The solid and broken curves are for polarization $\parallel$ (along [1-10]) and $\perp$ (along [001]), respectively. The peak in the photoluminescence spectra is of heavy hole excitons, whereas the two photoluminescence excitation peaks are of heavy hole excitons and light hole excitons. Optical anisotropy was observed in the heavy hole exciton transitions between $\parallel$ and $\perp$ polarization [17]. The signal ratio $I_\perp/I_\parallel$ was 60% in the photoluminescence peaks, and was 67% in the photoluminescence excitation, showing good agreement with each other. The results of optical anisotropy obtained from Figs. 4.2 and 4.3 are summarized in Table 4.1.

Discussion

We will discuss the optical anisotropy of quantum wells and quantum wires. The optical anisotropy of QW1 should be given by the well-known optical anisotropy of standard (001) quantum wells observed from the (110) cleaved surface [22]. In reality, the forbidden transition of heavy hole with $\perp$ polarization can be weakly observed. The observed photoluminescence excitation intensity $I_{HH,\perp}$ was about 14% of $I_{HH,\parallel}$, which is in fair agreement with the photoluminescence data of 6%. Reasonable agreement was obtained among the previous reports, the model calculation, and the present observation for the (001) quantum well, which supports the validity and the reliability of the following quantitative study on optical anisotropy in quantum wires.

T-QWRs shows the strong polarization dependence. As shown in Table 4.1, the photoluminescence excitation signal ratio $I_{\perp}/I_{\parallel}$ was 39%. Since there is some contribution of the smearing tail structures of the QW1 and the stray light, the estimation requires a proper extraction of these contribution. The value is obtained from the comparison of the peak intensity ratio, because peak heights are least affected by the additional contribution of the tail structures. The value is again in fair agreement with the photoluminescence data of 20%.

To look into the effect of the crystallographic anisotropy, we compare the optical anisotropy of quantum wires and that of quantum wells. As summarized in Table 4.1, though the values of $I_{\perp}/I_{\parallel}$ tend to be smaller for the photoluminescence data than for the photoluminescence excitation data, we found a clear difference between the results for the T-QWR and the reference (110) quantum well, which is ascribed to the optical anisotropy resulting purely from the lateral confinement in quantum wires.

Then, we compare experimental results with some model calculations in cylindrical quantum wires, which was given by Yamaüchi et al. [15] The optical anisotropy ratio $I_{\perp}/I_{\parallel}$ is expected to be 34% for the cylindrical quantum wire, whereas it is $I_{\perp}/I_{\parallel}(= I_{[001]}/I_{[1-10]})$=81% for the reference (110) quantum well. In spite of the obvious difference in the shape between cylindrical rods and the T-QWRs, we find a good agreement between the model calculation and the experiment. This may be because of a comparable confinement in y- and z-directions in the T-QWRs. To reproduce the optical anisotropy precisely, a more rigorous theory is required.

4.3 Structure dependence of optical anisotropy

We study systematically the polarization-dependent photoluminescence on a series of GaAs T-QWRs. We will present how the optical anisotropy in T-QWRs changes when the lateral confinement is gradually weakened from the quantum wire regime to the quantum well regime.

Experiment

A series of samples studied here are S1, whose details are described in §3.3. The inset of Fig. 4.4 shows the schematic structure of our T-QWR samples. The multiple quan-

tum well structure consists of n=50 periods of GaAs quantum wells (QW1; thickness a=5.4 nm) and $Al_{0.3}Ga_{0.7}As$ barriers (thickness c=50 nm), which is about 5-μm-thick all together. An additional 5-μm-thick $Al_{0.3}Ga_{0.7}As$ layer is formed in the first growth, which results in a 5-μm-wide area of QW2 after cleavage and overgrowth. The overgrown quantum well is of a GaAs layer (QW2; thickness b=4.6~8.3 nm), covered with an $Al_{0.3}Ga_{0.7}As$ barrier layer.

As mentioned earlier, we defined the [001] (the first growth direction) as the z-direction, the [110] (the overgrowth direction) as the y-direction, and the [1-10] (the quantum wire direction) as the x-direction. We also denoted polarization along [1-10] ([001]) as $\parallel$ ($\perp$), since [1-10] ([001]) is parallel (perpendicular) to the T-QWRs and the QW1 layers.

The spatially-resolved polarization-dependent photoluminescence spectra were measured at 4 K with a He-Ne laser. The spatial resolution was less than 2 μm. The photoluminescence was detected via the (110) surface in the backward scattering geometry under normal incidence. A polarizer and a depolarizer were placed in front of a monochromator to analyze the polarization.

Results

Figure 4.4 shows the spatially-resolved polarization-dependent photoluminescence spectra of four T-QWR samples with the different QW2 thickness b=4.8 nm, 5.3 nm, 5.9 nm, and 8.1 nm. Solid (dashed) curves show the photoluminescence intensity $I_{\parallel}$ ($I_{\perp}$) with polarization parallel (perpendicular) to the T-QWRs and the QW1 layers. Thick (thin) curves show the photoluminescence for the region with T-QWRs (5μm-wide QW2) indicated by a thick (thin) arrow in the inset. Then, we also measured the photoluminescence peak intensity ratio $I_{\perp}/I_{\parallel}$ for T-QWR, QW1, and QW2 in various samples with different b, and plotted it in Fig. 4.5.

Strong polarization anisotropy was observed in the photoluminescence from T-QWR, QW1, and QW2. The photoluminescence intensities with parallel polarization shown by solid curves in Fig. 4.4 were always larger than the photoluminescence intensities with perpendicular polarization shown by dashed curves. Although some data are scattered in Fig. 4.5, the optical anisotropy for QW1 and QW2 is close to the predicted values of 0% and 86%, respectively. On the other hand, the optical anisotropy $I_{\perp}/I_{\parallel}$ for T-QWR

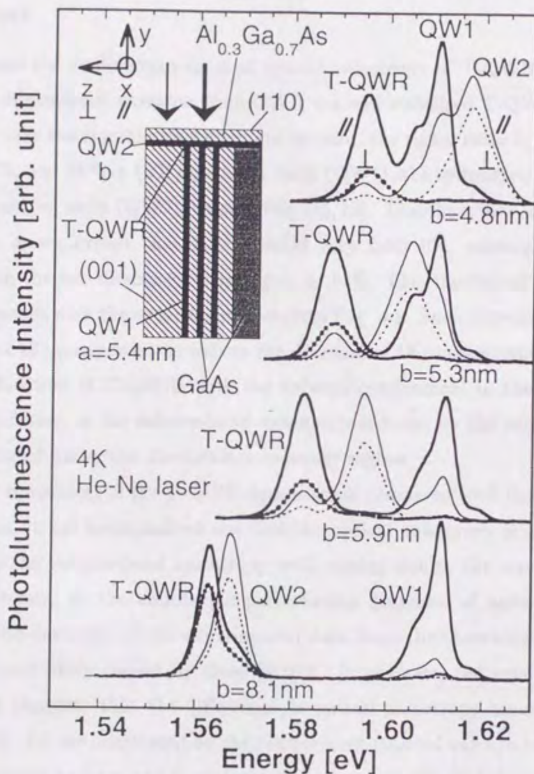

Figure 4.4: Spatially-resolved polarization-dependent photoluminescence spectra measured at 4 K for four kinds of GaAs/$Al_{0.3}Ga_{0.7}As$ T-QWR samples. The inset shows a schematic of the structure of the T-QWR samples. Solid (dashed) curves show the photoluminescence intensity with polarization parallel (perpendicular) to the T-QWRs and the QW1 layers. Thick (thin) curves show the photoluminescence for the region with T-QWRs (5 μm-wide QW2) indicated by a thick (thin) arrow in the inset.

increases from the value close to that of QW1 to the value identical to that of QW2 with increasing the QW2 thickness b.

Discussions

We will discuss the confinement-induced optical anisotropy of T-QWRs in Fig. 4.5 in terms of the dimensional crossover from QW1, via well-stabilized T-QWR, to QW2.

When we take the crystal anisotropy into account, the signal ratio $I_{\perp}/I_{\parallel}$ is calculated to be 0%, 34%, and 86% in (001) quantum wells (QW1), the symmetric quantum wires, and (110) quantum wells (QW2), respectively [15, 18]. Therefore, as b is increased from zero to $b \gg a$, we expect that $I_{\perp}/I_{\parallel}$ should vary from 0%, passing 34% when the confinement in the two directions is balanced, to 86%. This theoretical consideration is in good agreement with the experimental result in Fig. 4.5. Such increase of $I_{\perp}/I_{\parallel}$ shows the increase of $|Z\rangle$-component as well as the decrease of $|X\rangle$-component in the valence-band Bloch function of T-QWRs with the reduced confinement in the z-direction. In this way, the change in the valence-band anisotropy induced by the varied confinement was demonstrated under the dimensional crossover regime.

Note that the scatter of the T-QWR data is small compared with those of QW2. For quantum wells, it has been pointed out that the optical anisotropy is also caused very sensitively by the valence-band anisotropy with mixing due to the warping distortion, the uniaxial strain, or the anisotropic perturbation potential of anisotropic interface roughness. The deviation of the experimental data from the theoretical values of 86% for QW2 is most likely caused by these factors. In contrast, the small scatter of the T-QWR data supports that the differences in optical anisotropy among the series of samples in Fig. 4.5 are dominated by the confinement-induced valence-band anisotropy.

The next point to be noted is that the optical anisotropy of 34% corresponding to the symmetric confinement in quantum wire was achieved at around $b = a$ in Fig. 4.5. At $b = a$, the energy levels of the conduction electrons in QW1 and QW2 become equal due to the identical effective masses. Such structures are suitable to obtain a well-stabilized one-dimensional electron state is formed in the T-QWRs. On the other hand, the energy level of holes in QW2 is lower than that in QW1 at $b = a$. This is due to the different effective masses of the valence bands in QW1 on the (001) surface and in QW2 on the (110) surface, which are $0.38m_0$ (m_0; free-electron mass) and $0.71m_0$,

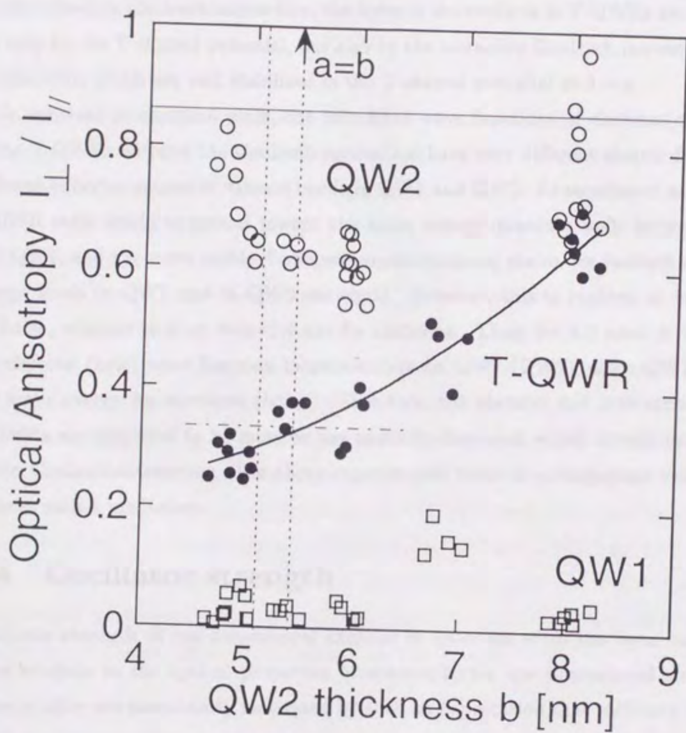

Figure 4.5: The optical anisotropy, defined as the photoluminescence peak intensity ratio $I_{\perp}/I_{\parallel}$ between the perpendicular and parallel polarizations, for T-QWR (solid circles), QW1 (open squares) , and QW2 (open circles) plotted against the QW2 thickness b. The solid curve is drawn to guide the eye. The results are to be compared with the theoretically predicted values of 0%, 86%, and 34% for QW1, QW2, and the symmetric quantum wires, respectively, which are shown by the horizontal lines.

respectively. Therefore, the hole state in T-QWRs should be close to that of QW2, and thus two-dimensional-like states. One should note that the symmetric confinement for holes in T-QWRs was achieved at around $b = a$, in spite of the fact that the optical anisotropy is sensitive to the valence-band anisotropy. We believe that this is caused by the electron-hole Coulomb interaction; the holes in the excitons in T-QWRs are confined not only by the T-shaped potential, but also by the attractive Coulomb interaction with the electrons which are well stabilized in the T-shaped potential at $b = a$.

In contrast to quantum wells, the calculated wave functions of electrons and holes in the T-QWRs without the Coulomb interaction have very different shapes due to the different effective masses of valence bands in QW1 and QW2. As mentioned earlier, the T-QWR state tends to spread toward the lower energy quantum wells between QW1 and QW2, and the most stable T-shaped one-dimensional states are realized when the energy levels in QW1 and in QW2 are equal. However, this is realized at b=4.0 nm for holes, whereas it is at b=a=5.4 nm for electrons. Thus, for 4.0 nm$< b <$5.4 nm, the electron (hole) wave function locates mainly on QW1 (QW2), since QW1 (QW2) has lower energy for electrons (holes). Therefore, the electron and hole states in the T-QWRs are supposed to be more or less spatially-displaced, which should be affected by the Coulomb interaction. The above experimental result is an important evidence to support such a prediction.

4.4 Oscillator strength

Oscillator strength of one-dimensional excitons in quantum wires has been one of the main subjects in the optical properties of semiconductor low dimensional structures. These studies are particularly motivated by such an expectation that oscillator strength might be concentrated into the lowest exciton state in quantum wires because of the one-dimensional electronic density-of-states [19] and the efficient Coulomb interaction among carriers [20, 21].

Oscillator strength can be directly evaluated by measuring absorption and/or reflection intensity of quantum wires, which are difficult due to the small volume of the quantum wires. In contrast, photoluminescence excitation spectroscopy provides us only relative intensities of the oscillator strength. Thus, to evaluate oscillator strength from

photoluminescence excitation spectra, careful comparison among systematic series of quantum wires is required. We present in this section the structure dependence of photoluminescence excitation spectra for three quantum wire samples, in which the lateral confinement is systematically changed. We have found the concentration of oscillator strength into one-dimensional exciton states with increasing lateral confinement.

Experiments

We prepared three T-QWR samples (C1 - C3) by the cleaved-edge overgrowth method. All the quantum well layers are of GaAs, while the barrier layers are of $Al_{0.3}Ga_{0.7}As$, which is shortly denoted as the GaAs/$Al_{0.3}Ga_{0.7}As$ structure. In making this series of samples, we performed the first growth simultaneously on one wafer and cut it into small pieces, on which three overgrowth runs were done changing the overgrown-quantum well thickness. Therefore, the three samples have the identical multi-quantum well layer, which consists of 200 periods of QW1 of thickness a=5.2 nm and barriers of thickness c=31 nm. On the other hand, the thickness b of the overgrown quantum wells (QW2) is changed as b=4.8 nm in C1, b=6.9 nm in C2, and b=10 nm in C3.

For these samples, we performed polarization-dependent photoluminescence and photoluminescence excitation measurements at 4K with a cw titanium sapphire laser and a conventional micro-photoluminescence setup. The photo-excitation and the detection was made along [110] direction via the (110) surface in the backward scattering geometry under the normal incidence condition. Note that the polarization of detected light was analyzed in the photoluminescence measurements, while that of excitation light was selected in the photoluminescence excitation measurements.

Results

Figures 4.6 - 4.8 show photoluminescence and photoluminescence excitation spectra of samples C1 - C3 with the different QW2 thickness b. In each figure, a pair of peaks shown by thin curves in the low energy region show the photoluminescence spectra of the one-dimensional excitons confined in T-QWRs, and a pair of thick curves in the higher energy region show their photoluminescence excitation spectra. The low energy part of the photoluminescence excitation spectra magnified by a factor of 20 are also shown. In each pair of spectra, the solid curve is obtained for the polarization parallel

to the T-QWRs, whereas the broken curve is for the polarization perpendicular to the T-QWRs. In the measurements for both polarizations, the detection sensitivity and the excitation intensity were kept constant. Furthermore, we set the scale of photoluminescence excitation spectra common among Figs. 4.6 - 4.8, as will be discussed later. Thus, we can compare all the photoluminescence excitation intensities among Figs. 4.6 - 4.8.

Figure 4.6 shows the photoluminescence and photoluminescence excitation spectra of C1 ($GaAs/Al_{0.3}Ga_{0.7}As$ T-QWRs, a=5.2 nm, b=4.8 nm). As indicated in the figure, the photoluminescence peaks at 1.602 eV and the lowest-energy photoluminescence excitation peaks at 1.606 eV are from the lowest exciton state at T-QWRs, while the larger photoluminescence excitation peaks at 1.627 eV and 1.651 eV are the heavy-hole (H-H) and light-hole (LH) exciton states in QW1, respectively. Such large contributions of QW1 to the photoluminescence excitation spectra of T-QWRs indicate a plentiful carrier flow from QW1 to T-QWRs. Structures associated with QW2 were not observed since they are located in the energy region higher than that of QW1 and are overshadowed by the much larger contributions of QW1. The polarization anisotropy in QW1 agrees with the well-known optical anisotropy in (001) quantum wells observed from the (110) cleaved surface [22].

Note here that such general features in Fig. 4.6 are similar to those of the GaAs/AlAs T-QWR sample (A2) in §4.2. This is because of the similarity in the parameters a and b, though the confinement is weaker due to the lower barriers in C1. Due to the better hetero-interface quality in C1, however, its spectral linewidths and the Stokes shift are smaller than A2. The photoluminescence linewidth (full width of half maximum) was 8.5 meV and the Stokes shift was 4 meV, representing the high quality of the sample. The effective lateral confinement energy of excitons E^{*}_{1D-2D}, the energy difference between T-QWRs and QW1, is found to be 21 meV in photoluminescence excitation spectra.

Figure 4.7 shows the photoluminescence and photoluminescence excitation spectra of C2 ($GaAs/Al_{0.3}Ga_{0.7}As$ T-QWRs, a=5.2 nm, b=6.9 nm). The photoluminescence peaks at 1.575 eV and the lowest-energy photoluminescence excitation peaks at 1.578 eV are from the heavy hole exciton state in T-QWRs, while the structure above 1.620 eV with two photoluminescence excitation peaks are from the heavy hole and light hole exciton states in QW1. The photoluminescence linewidth and the Stokes shift of T-QWRs are 6.2 meV and 3 meV, respectively, which are smaller than those of

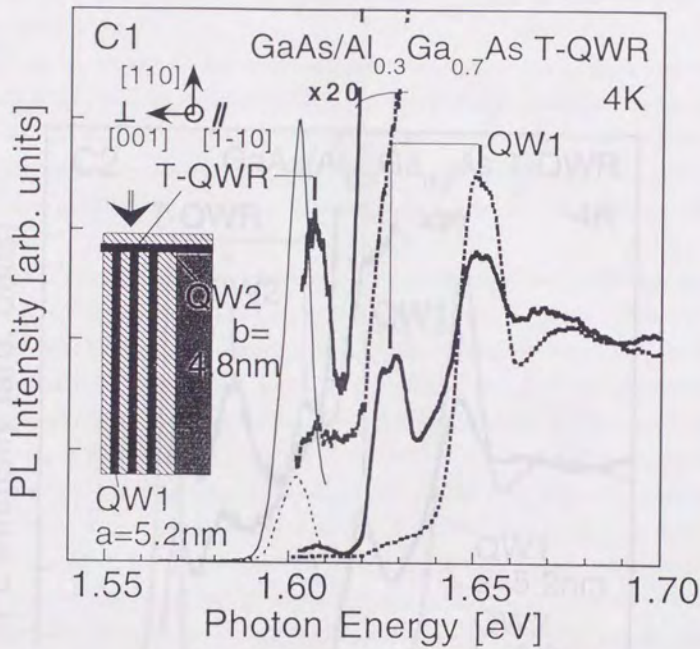

Figure 4.6: Photoluminescence (thin curves) and photoluminescence excitation (thick curves) spectra measured at 4 K for C1 ($GaAs/Al_{0.3}Ga_{0.7}As$ T-QWRs, a=5.2 nm, b=4.8 nm). The polarization of the light for detection in photoluminescence and excitation in photoluminescence excitation was parallel (‖, solid curves) or perpendicular (⊥, broken curves) to the T-QWRs. The magnified photoluminescence excitation spectra by a factor of 20 are shown for low energy region. The inset shows the schematic structure of the T-QWR sample.

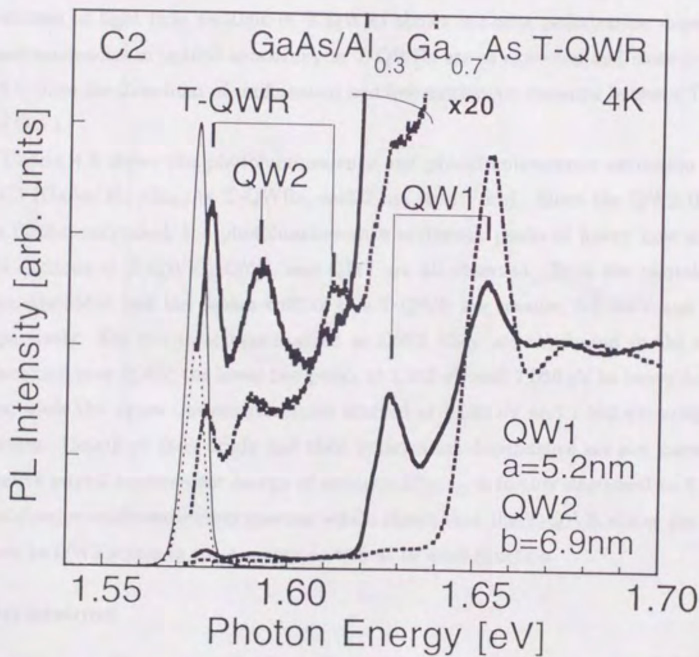

Figure 4.7: Photoluminescence (thin curves) and photoluminescence excitation (thick curves) spectra measured at 4 K for sample C2 ($GaAs/Al_{0.3}Ga_{0.7}As$ T-QWRs, a=5.2 nm, b=6.9 nm) for polarizations parallel (‖, solid curves) and perpendicular (⊥, broken curves) to the T-QWRs.

C1. The photoluminescence excitation peaks of heavy hole excitons in QW2 and the light hole excitons in T-QWRs are also observed in C2. Thus, the effective lateral confinement energy of excitons E^{*}_{1D-2D} is given by the energy distance between QW2 and T-QWRs, and decreases to be 14 meV, which shows that the T-QWR states take on two-dimensional character.

The photoluminescence and photoluminescence excitation intensities of heavy hole excitons in T-QWRs are stronger for the parallel polarization. The photoluminescence excitation of light hole excitons in T-QWRs shows opposite polarization dependence. These tendencies in optical anisotropy in T-QWRs are as expected and close to that in QW1, since the directions of confinement and free motion are common between T-QWRs and QW1.

Figure 4.8 shows the photoluminescence and photoluminescence excitation spectra of C3 (GaAs/$Al_{0.3}Ga_{0.7}As$ T-QWRs, a=5.2 nm, b=10 nm). Since the QW2 thickness b is further increased, the photoluminescence excitation peaks of heavy hole and light hole excitons in T-QWRs, QW2, and QW1 are all observed. Both the photoluminescence linewidth and the Stokes shift of this T-QWR are smaller, 5.1 meV and 3 meV, respectively. For the structures marked as QW2, they are attributed to the excitons delocalized over QW2; the lower two peaks at 1.563 eV and 1.566 eV to heavy hole excitons, while the upper unclear structures marked at 1.585 eV and 1.592 eV to light hole excitons. Details of their origin and their polarization dependence are not known. The effective lateral confinement energy of excitons E^{*}_{1D-2D} is further decreased to 6 meV in photoluminescence excitation spectra, which shows that the T-QWR states are getting closer to QW2 states in their energy as well as in wave function.

Discussions

We discuss oscillator strength of one-dimensional excitons from our detailed photoluminescence excitation measurements on three T-QWRs. We should first note in Fig. 4.7 that the photoluminescence excitation intensity of heavy hole excitons in T-QWRs is comparable with that of QW2, where their area-intensity ratio is about 1:2. This ratio is to be compared with the following geometrical factors. The period of quantum wires is given by $a+c$=36 nm, in which the wave functions of one-dimensional excitons in T-QWRs are bounded at the T-junction parts to have some reduced lateral size. On

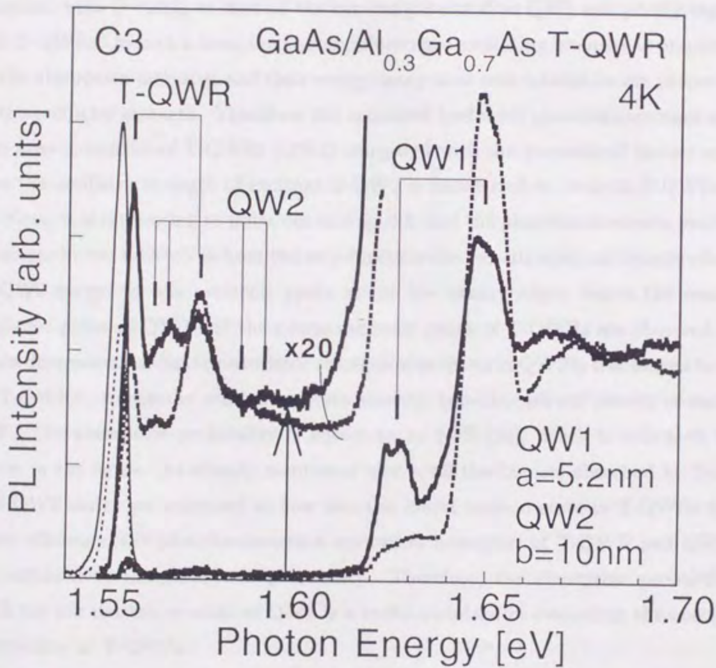

Figure 4.8: Photoluminescence (thin curves) and photoluminescence excitation (thick curves) spectra measured at 4K for sample C3 ($GaAs/Al_{0.3}Ga_{0.7}As$ T-QWRs, a=5.2 nm, b=10 nm) for polarizations parallel (∥, solid curves) and perpendicular (⊥, broken curves) to the T-QWRs. The photoluminescence excitation intensity for the continuum state of QW2 indicated by an arrow gives a measure of the absorption probability of 1.3%.

the other hand, the two-dimensional excitons denoted as QW2 are not bounded, but are extended over the period of 36 nm. Since the lateral size of one-dimensional exciton is less than 18 nm, the photoluminescence excitation area-intensity ratio of 1/2 is larger than the geometrical size ratio for the one-dimensional and two-dimensional excitons. Also note that the period of 36 nm is much smaller than the carrier diffusion length in quantum wells ($\sim \mu$m), so that all the carriers generated at QW2 are quickly captured into T-QWRs. In such a case, the photoluminescence excitation intensity is proportional to the absorption intensity, and their energy-integrated area-intensities are proportional to the oscillator strength. Therefore, the enhanced (reduced) photoluminescence excitation area-intensities of T-QWRs (QW2) compared with the geometrical factors suggest that the oscillator strength of excitons in QW2 is transferred to those in T-QWRs [23].

Next, it is interesting to point out in Fig. 4.8 that the photoluminescence excitation structure below 1.620 eV is from the step-function-like two-dimensional density-of-states of QW2 except for the excitonic peaks at the low energy edges, where the weakened excitonic peaks of QW2 and the strong excitonic peaks of T-QWRs are observed. This again demonstrates that the oscillator strength of excitons in QW2 is transferred to those in T-QWRs. As for the continuum state showing two-dimensional density-of-states of QW2, the absorption probability is known to be 1.3% [24], which is indicated by an arrow in the figure. As already mentioned above, all the carriers absorbed by T-QWR and QW2 states are supposed to flow into the lowest exciton state in T-QWRs by the same efficiency, the photoluminescence excitation intensities of T-QWR and QW2 are proportional to the absorption probability. Therefore, the absorption probability of 1.3% for the continuum state of QW2 is a useful standard in evaluating the absorption probability at T-QWRs.

Then, by comparing the photoluminescence excitation peak intensities of T-QWRs among the Figs. 4.6 - 4.8, we will evaluate absorption area-intensities of T-QWRs. Photoluminescence excitation signal intensities depend on so many factors; the absorption, energy relaxation, carrier migration processes, and the detection condition of photoluminescence, which may be different in the three figures. In the present case, however, the first growth parts with QW1 in C1 - C3 are cut from the same wafer and have identical properties, and hence that the carrier supply from QW1 to T-QWRs is identical for the three samples. Thus, we can compare the relative photoluminescence excitation

intensities of the overgrown parts in the three samples, by setting the scale of photoluminescence excitation spectra in Figs. 4.6 - 4.8 such that the photoluminescence excitation structures of QW1 have common amplitude. Then, the photoluminescence excitation intensity for the continuum state of QW2 indicated by an arrow in Fig. 4.8 gives the standard of the absorption probability of 1.3%. Therefore, we can evaluate absolute absorption probabilities at T-QWRs from the photoluminescence excitation intensities in Figs. 4.6 - 4.8.

The peak absorption probabilities of heavy hole excitons in T-QWRs in the three figures are evaluated to be 2.7%, 2.9%, and 3.0% for C1, C2, and C3, respectively. Multiplying the linewidth, we obtain the absorption area-intensities of three samples, which are 23 %meV, 18 %meV, and 15 %meV, respectively, and are plotted in Fig. 4.9. This shows that the oscillator strength is largest in C1, which has the strongest lateral confinement among the three samples. Note that the lateral size of the exciton wave function is smallest in C1, or that the cross sectional area for the incident light is smallest, which should contribute to reduce the photoluminescence excitation intensity. That is to say, if we normalize the obtained relative oscillator strength by the cross sectional area for the incident light, we obtain significant enhancement of the local oscillator strength in C1. We can conclude that the oscillator strength is not only enhanced, but also concentrated spatially at the T-junction part, when the lateral confinement is strong.

The lateral sizes of exciton wave functions in T-QWRs and QW2 in respective samples are not yet quantitatively evaluated. Thus, we are not able to normalize the observed oscillator strength with the sizes to quantify the local oscillator strength concentrated to the T-QWRs and to compare it with that of QW2. In addition, no theoretical model is currently available to quantitatively explain the increased oscillator strength with lateral confinement and the oscillator strength transfer from QW2 to T-QWRs. Hence, the quantitative analyses as well as the physical interpretation on the concentration of oscillator strength are the subject of future study.

4.5 Summary

Polarization and oscillator strength of one-dimensional states were systematically investigated from photoluminescence and photoluminescence excitation spectra from T-QWRs.

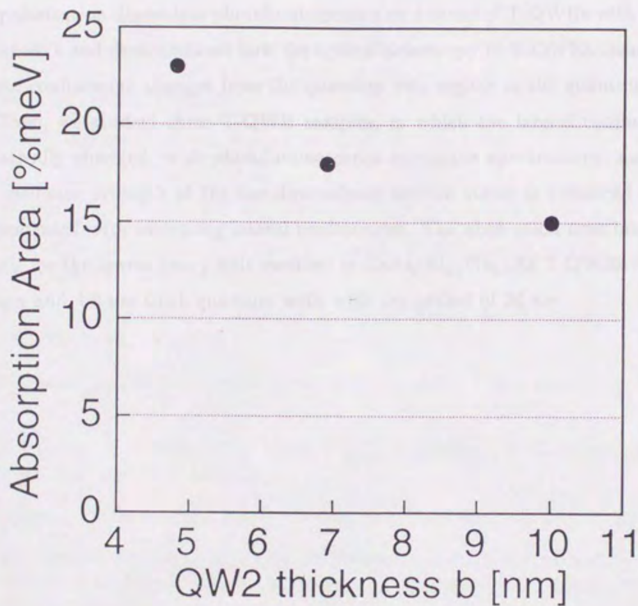

Figure 4.9: The enhancement of absorption area-intensity of heavy-hole excitons in T-QWRs with reduced QW2 thickness b, observed in samples C1, C2, and C3 (QW1 thickness a=5.2 nm, QWR period a+c=36 nm). Since lateral confinement is stronger for smaller b, the lateral size of the exciton wave function, and hence the cross sectional area for the incident light, are smaller for smaller b. Thus, the local oscillator strength obtained by normalizing each datum by the lateral size is to be significantly enhanced for smaller b.

First, we measured the optical anisotropy of the 5-nm-scale GaAs/AlAs T-QWR sample. The photoluminescence and photoluminescence excitation signals for T-QWRs were found to be more polarized along the T-QWRs. The optical anisotropy induced purely by the confinement potential in T-QWRs was evaluated via the comparison between the T-QWRs and the reference (110) quantum well. These results showed good agreement with a simple theory considering only the crystal band anisotropy. Next, we measured the polarization-dependent photoluminescence on a series of T-QWRs with various QW2 thickness b and demonstrated how the optical anisotropy in T-QWRs changes when the lateral confinement changes from the quantum wire regime to the quantum well regime.

Then, we studied three T-QWR samples, in which the lateral confinement is systematically changed, with photoluminescence excitation spectroscopy, and found that the oscillator strength of the one-dimensional exciton states is enhanced and spatially concentrated with increasing lateral confinement. The absorption area-intensity was 23 %meV for the lowest heavy hole excitons in $GaAs/Al_{0.3}Ga_{0.7}As$ T-QWRs formed by the 5.2-nm and 4.8-nm-thick quantum wells with the period of 36 nm.

Bibliography

[1] M. Tsuchiya, J. M. Gaines, R. H. Yan, R. J. Simes, P. O. Holtz, L. A. Coldren, and P. M. Petroff, Phys. Rev. Lett. **62**, 466 (1989); H. Weman, M. S. Miller, and J. L. Merz, Phys. Rev. Lett. **68**, 3656 (1992).

[2] M. Tanaka and H. Sakaki, Appl. Phys. Lett. **54**, 1326 (1989).

[3] D. Gershoni, J. S. Weiner, S. N. G. Chu, G. A. Baraff, J. M. Vandenberg, L. N. Pfeiffer, K. West, R. A. Logan, and T. Tanbun-Ek, Phys. Rev. Lett. **65**, 1631 (1990).

[4] A. R. Goñi, L. N. Pfeiffer, K. West, A. Pinczuk, H. U. Baranger, and H. L. Störmer, Appl. Phys. Lett. **61**, 1956 (1992).

[5] E. Kapon, K. Kash, E. M. Clausen, Jr., D. M. Hwang, and E. Colas, Appl. Phys. Lett. **60**, 477 (1992).

[6] H. Kanbe, A. Chavez-Pirson, H. Ando, H. Saito, and T. Fukui, Appl. Phys. Lett. **58**, 2969 (1991).

[7] H. Weman, M. S. Miller, C. E. Pryor, Y. J. Li, P. Bergman, P. M. Petroff, and J. L. Merz, Phys. Rev. B**48**, 8047 (1993).

[8] J. Bloch, U. Bockelmann, and F. Laruelle, Solid State Electron. 37, 529 (1994).

[9] E. Kapon, G. Biasiol, D. M. Hwang, M. Walther, and E. Colas, The 7th International Conference on Modulated Semiconductor Structures, (1995, Madrid, Spain); to be published in Solid-State Electronics.

[10] P. C. Sercal and K. J. Vahara, Appl. Phys. Lett. **57**, 545 (1990).

[11] D. S. Citrin and Y.-C. Chang, Phys. Rev. B**43**, 11703 (1991).

[12] H. Ando, S. Nojima, and H. Kanbe, J. Appl. Phys. **74**, 6383 (1993).

[13] G. E. W. Bauer and H. Sakaki, Surf. Sci. **267**, 442 (1992).

[14] G. Bastard, *Wave Mechanics Applied to Semiconductor Heterostructures* (Halsted Press, New York, 1988).

[15] A. A. Yamaguchi and A. Usui, J. Appl. Phys. **78**, 1361 (1995); A. A. Yamaguchi, K. Nishi, and A. Usui, Jpn. J. Appl. Phys. **33**, L912 (1994).

[16] J. S. Weiner, D. S. Chemla, D. A. B. Miller, H. A. Haus, A. C. Gossard, W. Wiegmann, and C. A. Burrus, Appl. Phys. Lett. **47**, 664 (1985).

[17] D. Gershoni, I. Brener, G. A. Baraff, S. N. G. Chu, L. N. Pfeiffer, and K. West, Phys. Rev. B**44**, 1930 (1991).

[18] C. R. McIntyre and L. J. Sham, Phys. Rev. B**45**, 9443 (1992).

[19] Y. Arakawa and H. Sakaki, Appl. Phys. Lett. **40**, 939 (1982).

[20] R. Loudon, Am. J. Phys. **27**, 649 (1959); R. J. Elliott, and R. Loudon, J. Phys. & Chem. Solids, **15**, 196 (1960).

[21] T. Ogawa, and T. Takagahara Phys. Rev. B15, **44**, 8138 (1991).

[22] J. S. Weiner, D. S. Chemla, D. A. B. Miller, H. A. Haus, A. C. Gossard, W. Wiegmann, and C. A. Burrus, Appl. Phys. Lett. **47**, 664 (1985).

[23] Similar effect has been recently demonstrated with near-field scanning optical microscopy in a strained quantum wire system; T. D. Harris, D. Gershoni, R. D. Grober, L. Pfeiffer, K. West, and N. Chand, Appl. Phys. Lett. **68**, 988 (1996).

[24] Y. Masumoto, M. Matsuura, S. Tarucha, and H. Okamoto, Phys. Rev. B**32**, 4275 (1985).

Chapter 5

Magneto-photoluminesce

5.1 Introduction

The spatial overlap of electron-hole wave functions is enhanced in quantum wells due to quantum confinement and enhanced electron-hole Coulomb interaction. The well-known room temperature excitonic absorption [1] and the enhancement of optical transition probability in quantum wells are caused by this enhanced overlap of wave functions. Quantum wires are attracting increasing interest since the wave functions can be further compressed by lateral confinement. Such compression of wave functions may lead to a substantial enhancement of the optical transition probability. Indeed, enhancement of binding energy of one-dimensional excitons was demonstrated in chapter 3 from the detailed photluminescence study on nanometer-scale T-shaped quantum wires (T-QWRs). Thus, it is very important to clarify the effect of lateral confinement on the effective size of exciton wave functions. In addition, such characterization of envelop parts of wave functions is complementary to the characterization of Bloch parts of wave functions via polarization properties described in chapter 4.

The effective size of excitons can be evaluated by studying the energy shift of photoluminescence under a magnetic field (diamagnetic shift). In this chapter, we present the systematic study on diamagnetic shifts of a series of high-quality nanometer-scale T-QWRs. We compared diamagnetic shifts among T-QWRs as well as between T-QWRs and reference quantum wells having the same thickness in the normal direction. As a result, the effect of lateral confinement on exciton wave functions in T-QWRs is quantitatively evaluated. In addition, since our T-QWRs were characterized by spatially-resolved

phtoluminescence before measuring diamagnetic shifts, it was possible to discuss the effective size of excitons in connection with the strucutral parameters.

5.2 Lateral size of one-dimensional excitons

To probe into the effect of lateral confinement in quantum wires, the effective size of exciton wave functions was evaluated from diamagnetic shifts. In such study, it is important to compare their diamagnetic shifts with those of quantum wells having the same normal thickness, since the Coulomb interaction enhanced by the confinement in the normal direction has already reduced the diamagnetic shift of two-dimensional excitons in quantum wells. We have to note that the Bohr radius of two-dimensional excitons decreases substantially, when the well thickness L_w is reduced, especially, down below 10 nm [2].

Although the diamagnetic shift was studied in several different quantum wires, this point was missing in the previous reports [3–7]. In some work [3–5], the lateral confinement is quite weak, and the measured diamagnetic shifts were almost the same as that of two-dimensional excitons in quantum wells. In other cases [6, 7], where the confinement was strong, the photoluminescence linewidth or the fluctuation of energy level was rather large (>10 meV), which made it difficult to examine small diamagnetic shifts with a sufficient accuracy less than 1 meV. Hence, for the quantitative evaluation of two-dimensional confinement, it is important to prepare very narrow quantum wires with good uniformity having the spectrum linewidth of less than 10 meV, and study their diamagnetic shifts in comparison with those of quantum wells.

In this chapter, we investigate photoluminescence properties of a series of T-QWRs in magnetic fields. We first show that their photoluminescence lines are always very sharp with the linewidths of 4∼7 meV, and then examine their diamagnetic shifts in magnetic fields up to 12 T, comparing them with those of reference quantum wells having the same thickness in the normal direction. The effect of lateral confinement on exciton wave functions in T-QWRs is quantitatively evaluated, separately from the enhanced two-dimensional excitonic effect caused by the confinement in the normal direction.

Experiment

We prepared four different T-QWRs (D1, D2, D3, and D4) by the cleaved-edge overgrowth method. As shown in the inset of Fig. 5.2, multi-quantum wells were prepared in the first growth; they contain n periods of GaAs quantum wells (QW1) of thickness a separated by $Al_{0.3}Ga_{0.7}As$ barriers of thickness c. After the cleavage, a GaAs quantum well layer (QW2) of thickness b and an $Al_{0.3}Ga_{0.7}As$ barrier were overgrown on the (110) cleaved surface to form the wire structures. Since QW1 is set to have higher energy than QW2, the confinement of quantum wire state is slightly stronger along the [110] (normal) direction than that along the [001] (lateral) direction. The geometry parameters of each sample are as follows; a=9.8 nm, b=11.6 nm, c=200 nm, and n=35 for D1, a=6.0 nm, b=6.4 nm, c=100 nm, and n=50 for D2, a=5.2 nm, b=5.3 nm, c=31 nm, and n=200 for D3, and a=5.2 nm, b=4.9 nm, c=31 nm, and n=200 for D4 [8].

Photoluminescence spectra of each sample were measured through an optical fiber with 100 μm core-diameter, which was attached to the (110) cleaved edge surface of the sample in the geometry shown in Fig. 5.1. The sample was directly immersed in liquid helium, and placed in the bore of a superconducting magnet to apply a magnetic field up to 12 T perpendicularly to the (110) surface. The sample mounted on the fiber was then excited by Ar^{+} laser. Photoluminescence from the sample was collected through the same fiber, and was dispersed into 0.32 m grating monochromator.

Results and analyses

The solid lines (a), (b), (c), and (d) in Fig. 5.2 are photoluminescence spectra of D1, D2, D3, and D4 measured at 0 T. For D1 and D2, three photoluminescence lines are clearly seen. Their origins are identified from the spatially-resolved photoluminescence, and found to come from T-QWR, QW1, and QW2, respectively. In D3 and D4, no photoluminescence peak was observed from QW2, because the inter-wire separation c (31 nm) is so small that most of the photo-generated carriers are efficiently collected by T-QWRs. Note that all the peaks are clearly observed with linewidths of 4$\sim$7 meV, indicating the good uniformity of the structures. From the photoluminescence spectra of Fig. 5.2 (a) and (b), we have found that the effective lateral confinement energy E^{*}_{1D-2D} of excitons for T-QWR is 6 meV for D1 and 11 meV for D2, respectively. Since the

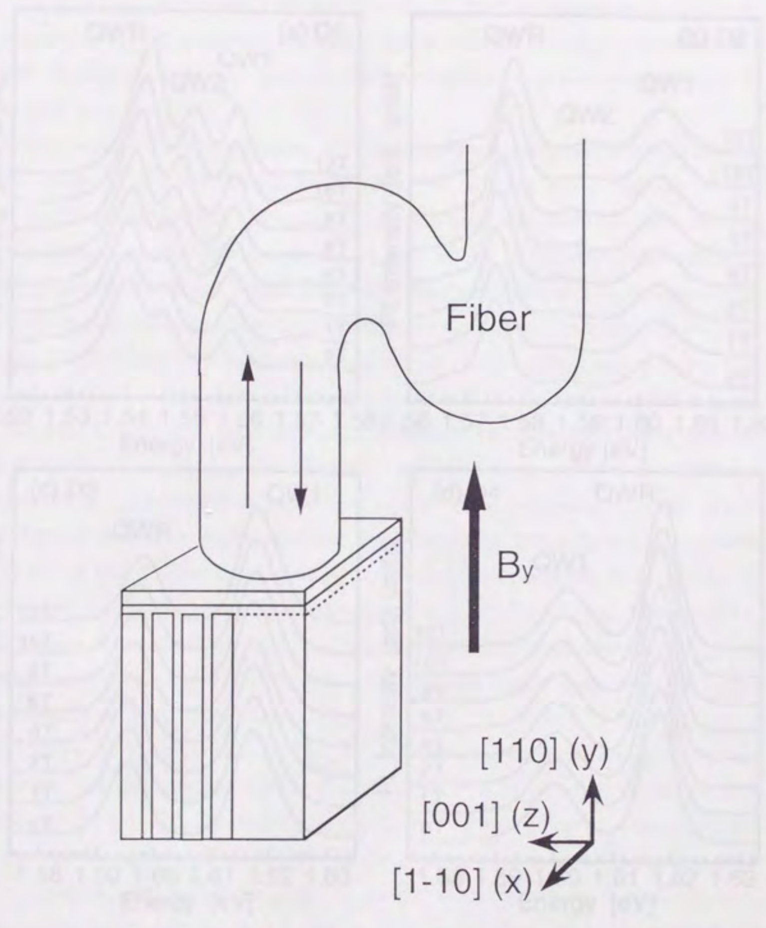

Figure 5.1: An experimental setup to measure photoluminescence in the magentic fields. For later argument, we define the z-direction as the first growth direction of [001], the y-direction as the second growth (overgrowth) direction of [110], and x-direction as [1-10] parallel to the T-QWRs.

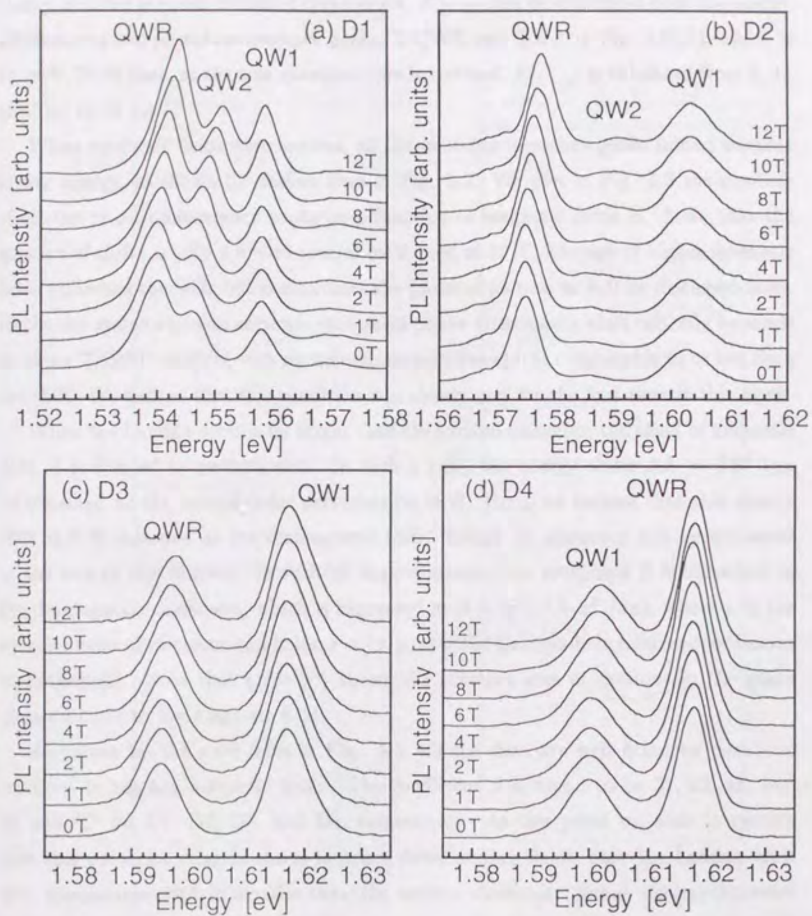

Figure 5.2: Photoluminescence spectra measured at 4.2K under magnetic fields up to 12 T from the quantum wells (QW1 and QW2) and T-QWR region of four samples: (a)D1, (b)D2, (c)D3, and (d)D4.

energy of QW1 is equal to that of QW2 in D4, E^{*}_{1D-2D} can be estimated from the energy difference of two photoluminescence peaks, T-QWR and QW1, in Fig. 5.2 (d), which is 16 meV. Note that, as the size quantum wire is reduced, E^{*}_{1D-2D} is enhanced from 6, 11 meV up to 16 meV.

When magnetic fields were applied, all the photoluminescence peaks shifted towards higher energy, as shown by dashed lines in Fig. 5.2. We plot in Fig. 5.3 the position of all the photoluminescence peaks as a function of magnetic fields B. Note that the amount of shifts is only a few to several meV even at 12 T. The use of higher magnetic fields enhances the shift but complicates the physical picture as will be discussed later. Hence the systematic and accurate evaluation of the diamagnetic shift can only be made on those T-QWR samples with photoluminescence linewidths comparable to or less than the shift. We believe that this condition was clearly met for the first time in this work.

When the Landau orbit is far larger than the exciton diameter, the effect of magnetic field B is treated as perturbation. In such a case, the energy shifts $\Delta E = \beta B^2$ can be obtained as the second order perturbation of B. Here, we assume that this energy shift ΔE is regarded as the diamagnetic shift, though its adequacy will be discussed at the end of this chapter. In such an approximation, the coefficient β is identified as the diamagnetic coefficient, which is expressed as $\beta = \langle e^2(z^2 + x^2)/8\mu \rangle$, where μ is the reduced mass of electrons and holes, $\mathbf{r} = (x, y, z)$ is the electron-hole relative coordinates in excitons[9]. Note that $\langle z^2 + x^2 \rangle$ shows the effective area of excitons in the plane perpendicular to the magnetic field.

As shown by the solid lines in Fig. 5.3, all the data are well fitted by parabolic relations in the low magnetic fields. The coefficient β is found to be 31, 23, 18, and 13 $\mu eV/T^2$ for D1, D2, D3, and D4, respectively. At this point we wish to remark that this parabolic relation starts to break down at high fields, once the Landau orbit gets comparable with or smaller than the exciton diameter. Hence the experimental determination of β must be carefully made using the data in the region of relatively low field. In most of the previous work, this point was overlooked, which seems to have resulted in a relatively wide spread of data points [10].

In Fig. 5.4, we have plotted by solid circles the diamagnetic coefficient β of four T-QWRs as a function of the well thickness b of QW2. For comparison, we collected the coefficients β of nine $GaAs/Al_{0.3}Ga_{0.7}As$ quantum wells having different well thicknesses

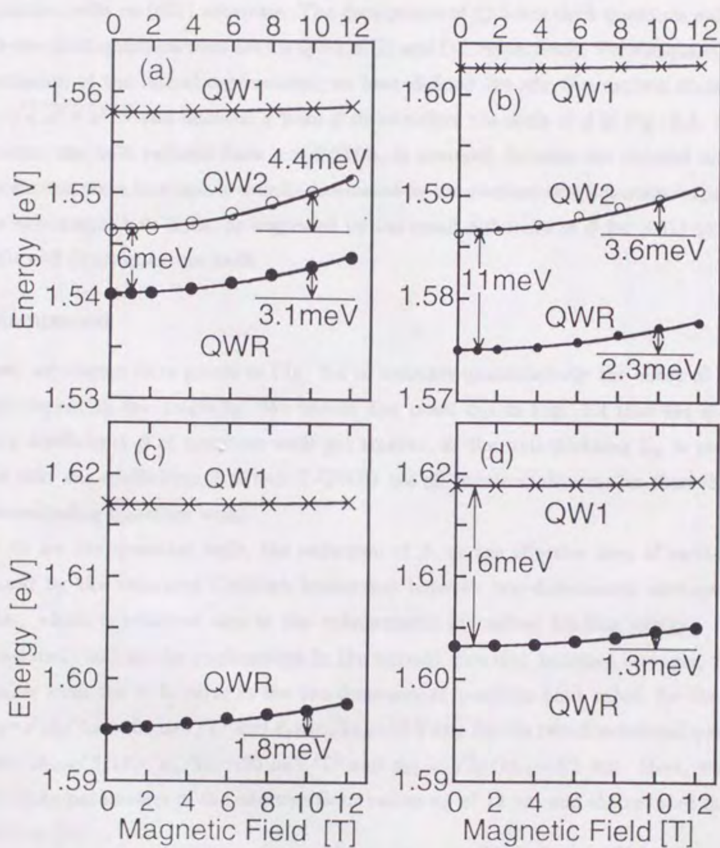

Figure 5.3: Diamagnetic shifts of various photoluminescence peaks from D1 (a), D2 (b), D3 (c), and D4 (d). We also show diamagnetic shifts at 10 T, which are determined by fitting the data points with a parabolic relation.

L_w, and have plotted them by blank circles and blank squares in Fig. 5.4. The blank circles are for quantum wells grown on (110) substrate, while blank squares are for quantum wells on (001) substrate. The data points of 12.5-nm-thick quantum wells and 6.8-nm-thick quantum wells are for QW2 of D1 and D2, respectively. For the quantitative discussion of the lateral confinement, we have defined the effective exciton diameter d as $\sqrt{< z^2 + x^2 >}$ and deduced d from β to introduce the scale of d in Fig. 5.4. In this process, the bulk reduced mass $\mu = 0.057m_0$ is assumed, because the reduced mass, or the exciton wave function, is usually dominated by the electron effective mass rather than the anisotropic hole mass, as suggested by the small difference of β for (001) quantum wells and (110) quantum wells.

Discussion

Now, we discuss data points in Fig. 5.4 to evaluate quantitatively the effect of lateral confinement in the T-QWRs. We should first point out in Fig. 5.4 that the diamagnetic coefficients β of quantum wells get smaller, as the well-thickness L_w is reduced, and that the coefficients β of four T-QWRs are all substantially smaller than those of corresponding quantum wells.

As for the quantum wells, the reduction of β, or the effective area of excitons, is caused by the enhanced Coulomb interaction between two-dimensional electrons and holes, which is reflected also in the enhancement of exciton binding energy. As L_w is reduced, and as the confinement in the normal direction becomes stronger, β gets smaller from the bulk value to the two-dimensional quantum limit value: for the bulk, $\beta_{3D}=e^2a_B^2/4\mu=107\ \mu\text{eV/T}^2$ and $d_{3D}=\sqrt{2}a_B=16.9$ nm; for the two-dimensional quantum limit, $\beta_{2D}=(3/16)e^2a_B^2/4\mu=20\ \mu\text{eV/T}^2$ and $d_{2D}=(\sqrt{3}/4)d_{3D}=7.3$ nm. Here, we used the GaAs parameters of the effective Bohr radius a_B of 12 nm and the reduced mass of $0.057m_0$ [11].

This decrease of β for two-dimensional excitons in quantum wells indicates that the reduction of β in T-QWRs below the level of its bulk value is caused partly by the confinement along the thickness direction and partly by lateral confinement. By comparing the values of β or d in T-QWRs with those of quantum wells with the same L_w, we can separate these contributions and evaluate the effect of lateral confinement separately from the confinement only along the normal direction which enhances two-

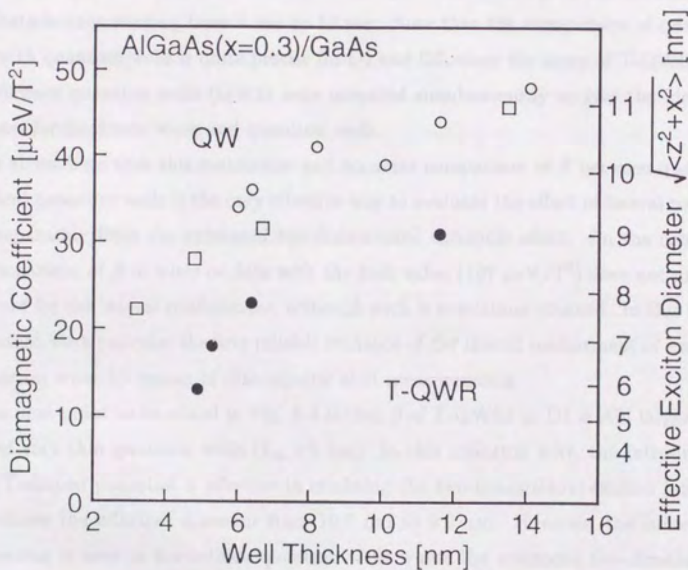

Figure 5.4: The diamagnetic coefficient of four T-QWRs (solid circles) and nine $Al_{0.3}Ga_{0.7}As/GaAs$ quantum wells. The blank circles are for quantum wells grown on (110) substrate, while blank squares are for quantum wells on (001) substrate.

dimensional excitonic effect. For example, in D1 where a=9.8 nm and b=11.6 nm, the effective exciton diameter d is 10.7 nm for quantum wells, but is slightly reduced to 9.0 nm in T-QWRs because of its lateral confinement. In D2 where a=6.0 nm and b=6.4nm, d in quantum wells is reduced to 9.7 nm whereas d in T-QWRs is further squeezed to 7.7 nm. In sample D4 where a=5.2 nm and b=4.9 nm, d in quantum wells is 8.6 nm but d in T-QWRs becomes as small as 5.8 nm. These data clearly show that excitons are all laterally squeezed by the T-shaped potential profile in these quantum wire samples with feature sizes ranging from 5 nm to 12 nm. Note that the comparison of quantum wires with quantum wells is quite precise for D1 and D2, since the array of T-QWRs and the reference quantum wells (QW2) were prepared simultaneously to give the identical thickness for quantum wires and quantum wells.

We stress here that this systematic and accurate comparison of β between quantum wires and quantum wells is the only effective way to evaluate the effect of lateral confinement separately from the enhanced two-dimensional excitonic effect. On the contrary, the comparison of β in wires or dots with the bulk value (107 μeV/T^2) does not provide any proof for the lateral confinement, although such is sometimes claimed. In this sense, the present work provides the first reliable evidence of the lateral confinement of excitons in quantum wires by means of diamagnetic shift measurements.

The next point to be noted in Fig. 5.4 is that β of T-QWRs in D1 is still larger than those of very thin quantum wells (L_w <5 nm). In this quantum wire, the introduction of the T-shaped potential is effective in confining the two-dimensional exciton laterally and reduces the effective diameter from 10.7 nm to 9.0 nm. However, the same level of squeezing is seen in 5-nm-thick quantum wells where the enhanced two-dimensional excitonic effect reduces the exciton diameter. This again shows that the simple reduction of β or d does not always provide as a proof for the lateral confinement.

The third point clarified by Fig. 5.4 is that the effective diameter of excitons in T-QWRs of D4 goes below that of two-dimensional quantum limit. Note in D4 that β is as small as 13 μeV/T^2 and d is squeezed to 5.8 nm. We must compare these values with those of two-dimensional excitons. In the limit of thin quantum wells (two-dimensional quantum limit), β_{2D} is predicted to get as small as 20 μeV/T^2 and d shrinks to 7.3 nm. In reality, as the thickness of wave function in GaAs quantum wells remains finite, one expects that β becomes saturated at around 22 μeV/T^2 and d=7.6 nm, which is

indeed demonstrated in 3-nm-thick quantum well. Therefore, we can conclude that the exciton wave function in the smallest T-QWR is squeezed more strongly than those of two-dimensional excitons in GaAs quantum wells under the two-dimensional quantum limit.

We wish to remark here the significance of the reduction in β, or the exciton diameter, in the context of optical device application. The optical transition probability of excitons is proportional to the squared amplitude $|\phi(0)|^2$ of the exciton wave function at the center position, which is the probability that an electron and a hole locate at the same position. Since $|\phi(0)|^2$ increases inversely proportional to the exciton effective area, and thus to the diamagnetic coefficient β, the observed reduction of β in T-QWRs indicates the possibility of enhancing an optical transition process to a level that has never been achieved in any GaAs quantum wells.

5.3 Shape of one-dimensional excitons

To gain an insight into lateral confinement effects, we evaluated in §5.2 the lateral size of one-dimensional excitons in T-QWRs by measuring diamagnetic shifts. However, such study clarified the spread of wave functions only along one direction (the lateral direction). Now our interest is to elucidate stereoscopic shapes of one-dimensional excitons in the three-dimensional space. For this purpose, applying magnetic fields in the three directions, we measured energy shifts of photoluminescence from a series of nanometer-scale T-QWRs, where lateral confinement was changed systematically. Based on the perturbation theory in the low magnetic field regime, the energy shifts were analyzed to evaluate the effective size of excitons. We have demonstrated that three-dimensional shapes of one-dimensional excitons are consistently deformed by changing lateral confinement. Short discussion will be given at the end of this section to examine adequacy of the simple perturbation theory used in the present study.

Experiment

We studied three different T-QWRs (E2 $\sim$ E4), which were selected from series S1 in §3.3, and a reference quantum well (E1). Figure 5.1 shows the schematic sample structure of T-QWRs. The multi-quantum well layer consists of GaAs quantum wells (QW1) and

$Al_{0.3}Ga_{0.7}As$ barriers. All T-QWR samples have the same QW1 thickness a=5.4 nm. The overgrown quantum well (QW2) is of a GaAs layer (thickness b), covered with an $Al_{0.3}Ga_{0.7}As$ barrier layer. We changed b as 5.0 nm for E2, 6.0 nm for E3, and 7.6 nm for E4. Sample E1 is QW1 in the first growth wafer without overgrowth, which will be referred as a T-QWR with b=0 nm. A more detailed description of sample design and preparation was given in §3.3. For later argument, we define the z-direction as the first growth direction of [001], the y-direction as the second growth (overgrowth) direction of [110], and x-direction as [1-10] parallel to the T-QWRs, as shown in Fig. 5.1.

To measure photoluminescence spectra under magnetic fields, we attached an optical fiber with 100 μm core-diameter to the (110) edge surface of the sample. Then, the sample was directly immersed in liquid helium, and placed in the bore of a superconducting magnet. The excitation and the detection of photoluminescence were performed through the same fiber.

Results and analyses

The solid lines (a) and (b) in Fig. 5.5 are typical photoluminescence spectra measured at 0 T for two T-QWR samples having the QW2 thickness b=5.0 nm in E2 and 6.0 nm in E3, respectively. Each photoluminescence peak was assigned with the spatially-resolved photoluminescence measurement, as described in chapter 3. The photoluminescence peaks of T-QWRs are sharp with linewidth of about 8-10 meV, indicating the good uniformity of the structures. The photoluminescence peaks of QW1 and QW2 are overlapped with each other, resulting in a broad peak shown in the solid line (a).

For these samples, we applied magnetic fields B up to 12.5 T in the x-, y-, and z-directions. As B increased, all the photoluminescence peaks shifted towards higher energy. The three fine lines in Fig. 5.5 show the photoluminescence spectra at B =12.5 T applied along the three directions. To investigate the amounts of shifts, we plot in Fig. 5.6 the positions of all the photoluminescence peaks of T-QWRs as a function of squares of magnetic fields B^2. In the present samples, the measurement error of photoluminescence peak energy is less than 1 meV.

Note that energy shifts ΔE are proportional to B^2 like $\Delta E = \beta B^2$ in the regime from 2 to 12.5 T, where the slopes β depend both on sample structures and directions of magnetic fields. Some data points in the low magnetic field regime below 2 T are

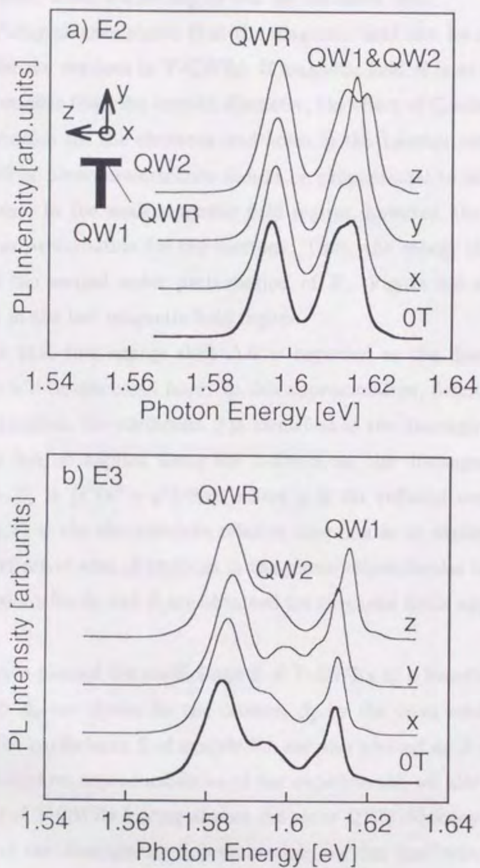

Figure 5.5: Photoluminescence spectra measured at 4.2K from two T-QWR samples (E2 and E3), where QW2 thickness b is 5.0 nm in E2 (a) and 6.0 nm in E3 (b). The solid lines are for zero magnetic field, while the fine lines are for the field of 12.5T. We defined the z-direction as the first growth direction of [001], the y-direction as the second growth (overgrowth) direction of [110], and x-direction as [1-10] parallel to the T-QWRs.

scattered from the fitted lines, whose origins will be discussed later.

The observed B^2-dependence shows that the magnetic field can be considered as a weak perturbation for the excitons in T-QWRs. If magnetic field B is so strong that the Landau orbit is far smaller than the exciton diameter, the effect of Coulomb interaction is treated as perturbation for the electrons and holes in the Landau orbits. In such a case, the energy shift of photoluminescence should be proportional to magnetic field B (Landau quantization). In the weak magnetic field regime, however, the magnetic field is in turn regarded as perturbation for the excitons. Then, the energy shift $\Delta E = \beta B^2$ can be obtained as the second order perturbation of B. Figure 5.6 shows that our measurement is still in the low magnetic field regime.

Here, we assume that this energy shift ΔE is regarded as the diamagnetic shift, though its adequacy will be discussed later. In this approximation, denoted hereafter as diamagnetic approximation, the coefficient β is identified as the diamagnetic coefficient. When the magnetic field is applied along the z-direction, the diamagnetic coefficient is expressed as, $\beta = \beta_z \equiv \langle e^2(x^2 + y^2)/8\mu \rangle$, where μ is the reduced mass of electrons and holes, $\mathbf{r} = (x, y, z)$ is the electron-hole relative coordinates in excitons. Note that $\langle x^2 + y^2 \rangle$ shows the effective area of excitons in the plane perpendicular to the magnetic field. Similar expressions for β_x and $\beta_y$are obtained for magnetic fields applied along the x- and y-directions.

In Fig. 5.7, we have plotted the coefficients β of T-QWRs as a function of the QW2 thickness b, in which β_x are shown by the crosses, β_y by the open circles, and β_z by the solid squares. The coefficients β of sample E1 are also plotted as β of T-QWRs at b=0. In addition, to confirm reproducibilities of our experiments, we also evaluated and plotted in Fig. 5.7 β of T-QWRs having almost the same QW2 thickness as E2 ($b \sim$5.0 nm). On the basis of the diamagnetic approximation, we can qualitatively considered that Fig. 5.7 represents the effective area of exciton wave functions projected along the three directions, and hence the shape of the wave functions, in the samples with systematically changed confinement.

Discussion

First, we will discuss data points of samples E1 and E4. In E4, the QW2 thickness $b \sim$7.6 nm is much larger than the QW1 thickness $a \sim$5.4 nm. Thus, the T-QWR states

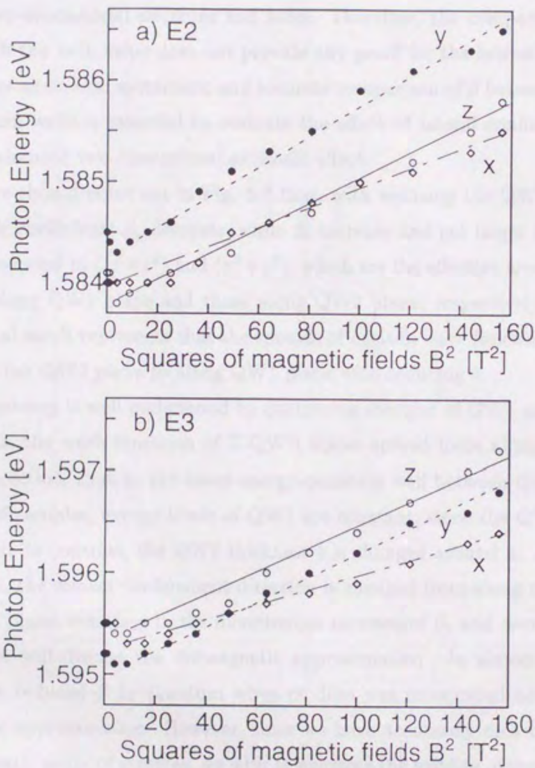

Figure 5.6: The diamagnetic shifts of PL peaks of two T-QWRs, where QW2 thickness b is 5.0 nm in E2 (a) and 6.0 nm in E3 (b), are plotted as a function of squares of magnetic fields B^2.

in E4 are close to the two-dimensional states of QW2 in wave functions. In Fig. 5.7, coefficients β of E1 and E4 in the three directions are much smaller than the bulk value of β (107 μeV/T^2). Such reduction of β is caused by the enhanced Coulomb interaction between two-dimensional electrons and holes. Therefore, the comparison of β in wires or dots with the bulk value does not provide any proof for the lateral confinement. We should stress again that systematic and accurate comparison of β between quantum wires and quantum wells is essential to evaluate the effect of lateral confinement separately from the enhanced two-dimensional excitonic effect.

Next, we should point out in Fig. 5.7 that, with reducing the QW2 thickness b, the diamagnetic coefficients β_y decrease, while β_z increase and get larger than β_y. Here, β_y and β_z correspond to $\langle z^2+x^2\rangle$ and $\langle x^2+y^2\rangle$, which are the effective areas of exciton wave functions along QW1 plane and those along QW2 plane, respectively. Therefore, this experimental result represents that the spreads of exciton wave functions are transferred from along the QW2 plane to along QW1 plane with reducing b.

This tendency is well understood by comparing energies of QW1 and those of QW2. In T-QWRs, the wave functions of T-QWR states spread more along the weaker confinement direction, that is, the lower-energy-quantum well between QW1 and QW2. In our series of samples, energy levels of QW1 are constant, since the QW1 thickness a is set constant. In contrast, the QW2 thickness b is changed around a. As a result, when b is reduced, the weaker confinement direction is changed from along the QW2 plane to along QW1 plane, resulting in the monotonous increase of β_z and decrease of β_y.

Here, we will discuss the diamagnetic approximation. In almost all the previous reports, the reduced β in quantum wires or dots was interpreted on the basis of the diamagnetic approximation. However, since we have accurately measured energy shifts on a systematic series of samples, we wish to examine the validity of such approximation.

First, we check that the low magnetic field approximation holds well in our experiment. In some previous work, energy shifts ΔE of quantum wells were analyzed beyond the range described by perturbation theory, which results in the serious discrepancy between measurements and theories. However, such discrepancy should be less in quantum wires because the extra confinement makes perturbation theory applicable to higher magnetic fields B. Indeed, the energy shifts ΔE of our T-QWRs were well fitted with the parabolic relations in the range from 2 to 12.5 T. Thus, we can conclude that our

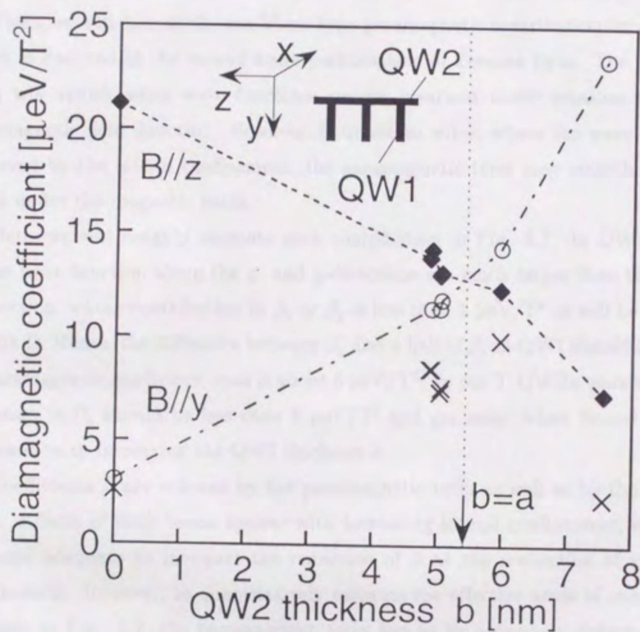

Figure 5.7: The diamagnetic coefficients β of T-QWRs are plotted as a function of the QW2 thickness b, in which β_x are shown by the crosses, β_y by the open circles, and β_z by the solid squares.

measurement is still in the low magnetic field regime.

Some data points in the low magnetic field regime less than 2 T are deviated from the fitted lines, as shown in Fig. 5.6. We speculate that it was caused by the effect of localization and/or the first order perturbation of Zeeman term. However, we should note that such discrepancy between our experimental data and the fitted lines is less than 0.5 meV, and therefore its effect on our evaluation of β should be quite small.

Then, we will discuss the van Vleck-type paramagnetic contribution for energy shifts, which is deduced as the second order perturbation of Zeeman term. The paramagnetic term will vanish when wave functions remain invariant under rotation as an axis of the magnetic field direction. However, in quantum wires, where the wave functions are squeezed by the lateral confinement, the paramagnetic term may contribute to energy shifts under the magnetic fields.

Here, we will roughly estimate such contribution in Fig. 5.7. In QW1, the spread of the wave function along the x- and y-directions are much larger than that along the z-direction, whose contribution to β_x or β_y is less than 1 μeV/T^2 as will be given in Appendix D. Hence, the difference between β_x and a half of β_z in QW1 should be attributed to paramagnetic coefficient, that is about 6 μeV/T^2. In our T-QWRs, paramagnetic contribution in β_z should be less than 6 μeV/T^2 and get small when lateral confinement decreases with increasing the QW2 thickness b.

Coefficients β are reduced by the paramagnetic term as well as by the diamagnetic term. Effects of both terms appear with increasing lateral confinement, and therefore it seems adequate to interpret the reduction of β as the realization of strong lateral confinement. However, to quantitatively evaluate the effective areas of one-dimensional excitons in Fig. 5.7, the paramagnetic term has to be accurately determined in each T-QWR sample. For this purpose, some model calculations may be useful.

5.4 Summary

Diamagnetic shifts have been studied on a series of high-quality nanometer-scale T-QWRs in careful comparison with reference quantum wells. It is demonstrated that diamagnetic coefficients β, which represent the lateral size of exciton wave function, are consistently smaller than those of two-dimensional excitons with the same thick-

ness, proving the effectiveness of lateral confinement in T-QWR structures. In T-QWRs formed by intersecting 5-nm-thick quantum wells, β is found to get as small as 13 μeV/T^2, which is below the theoretical limit for two-dimensional excitons in GaAs quantum wells.

Then, to clarify stereoscopic shapes of one-dimensional excitons, we measured diamagnetic shifts of T-QWRs by applying magnetic fields in the three directions. It is demonstrated that shapes of one-dimensional excitons are consistently and systematically deformed by changing lateral confinement.

Bibliography

[1] D. A. B. Miller, D. S. Chemla, D. J. Eilenberger, P. W. Smith, A. C. Gossard, and W. T. Tsang, Appl. Phys. Lett. **41**, 679 (1982).

[2] H. Sakaki, Y. Arakawa, M. Nishioka, J. Yoshino, H. Okamoto, and N. Miura, Appl. Phys. Lett. **46**, 83 (1985).

[3] M. Kohl, D. Heitmann, P. Grambow, and K. Ploog, Phys. Rev. Lett. **63**, 2124 (1989).

[4] A. S. Plaut, H. Lage, P. Grambow, D. Heitmann, K. von Klitzing, and K. Ploog, Phys. Rev. Lett. **67**, 1642 (1991).

[5] H. Weman, E. D. Jones, C. R. McIntyre, M. S. Miller, P. M. Petroff, and J. L. Merz, Superlattices and Microstruct. **13**, 5 (1993).

[6] Y. Nagamune, Y. Arakawa, S. Tsukamoto, M. Nishioka, S. Sasaki, and N. Miura, Phys. Rev. Lett. **69**, 2963 (1992).

[7] R. Rinaldi, R. Cingolani, M. Lepore, M. Ferrara, M. Catalano, F. Rossi, L. Rota, E. Molinari, P. Lugli, U. Marti, D. Martin, F. Morier-Gemound, P. Ruterana, and F. K. Reihart, Phys. Rev. Lett. **73**, 2889 (1994).

[8] The well thickness a and b are determined by comparing the photoluminescence data with calculated energy levels of quantum wells. See Appendix B.

[9] O. Akimoto and H. Hasegawa, J. Phys. Soc. Jpn. **22**, 181 (1967).

[10] G. E. W. Bauer and T. Ando, Phys. Rev. B**37**, 3130 (1988), and refernces therein.

[11] *Physics of Group IV Elements and III-V Compounds*, edited by O. Madelung, M. Schulz, and H. Weiss, Landort-Börnstein Numerical Data and Relationships, New Series, Group III, Vol. 17a (Springer, Berlin, 1982).

Chapter 6

Summary and conclusion

6.1 Summary

We summarize main results in the present work. First, we optimized the condition of the cleaved edge overgrowth method to produce high-quality T-shaped quantum wires (T-QWRs).

- We presented the refined method of *in-situ* cleavage, by which we can prepare smooth and damage-free edge surface with good reproducibility.
- We optimized the growth condition of GaAs, AlGaAs, AlAs, and InGaAs on (110) GaAs.

Next, based on such methods, we have fabricated various T-QWRs.

- We have made a series of 5-nm-scale T-QWRs with GaAs/AlGaAs, GaAs/AlAs, InGaAs/AlGaAs material systems.
- We have made T-QWRs with various structural sizes from 5 to 12 nm.

Then, we investigated optical properties on a series of T-QWRs. To comprehensively elucidate lateral confinement effects, the same series of T-QWRs were measured with various spectroscopic methods. All the experimental results proved consistently the effectiveness of lateral confinement in T-QWRs.

- We have characterized quantum wires with spatially-resolved photoluminescence technique and determined the structure dependence of energy levels in T-shaped quantum wires.

- In 5-nm-scale T-shaped GaAs quantum wires with AlAs barriers, the effective lateral confinement energy E^*_{1D-2D} becomes as large as 38 meV, which is beyond the thermal energy kT at 300 K.

- With increasing lateral confinement, binding energy of one-dimensional excitons increases and reaches 27 meV, which is 6-7 times as large as the bulk value.

- From a systematic measurement of optical anisotropy in quantum wires and quantum wells, we characterized quantitatively the effect of lateral confinement on valence band structures.

- We studied photoluminescence excitation spectra of T-QWR samples, in which the lateral confinement is systematically changed, and found that the oscillator strength of the one-dimensional exciton states is enhanced with increasing lateral confinement.

- We have demonstrated that diamagnetic coefficients β, which represent the lateral size of exciton wave function, are consistently smaller than those of two-dimensional excitons with the same thickness, proving the effectiveness of lateral confinement in T-QWRs.

6.2 Prospects in the future

We have realized strong lateral confinement in T-shaped quantum wires (T-QWRs) and demonstrated various novel properties of one-dimensional states. However, it is still very important to further enhance lateral confinement in quantum wires. We believe that such strong lateral confinement leads to discovery of new optical phenomena in quantum wires.

To exploit unique features of one-dimensional states for such device applications as quantum wire lasers, modulators, and intersubband detectors, it is important to realize optical waveguides where one-dimensional electronic states interact strongly with photon and to investigate effects of electric fields in doped quantum wires.

Appendix A

Sample list

Sample number	Well material	Barrier material	a (nm)	b (nm)	c (nm)	n (period)	Type
A1	GaAs	$Al_{0.3}Ga_{0.7}As$	6.0	6.4	100	50	–
A2	GaAs	AlAs	5.3	4.8	50	50	–
A3	GaAs	$Al_{0.3}Ga_{0.7}As$	9.8	11.6	200	20	–
S1	GaAs	$Al_{0.3}Ga_{0.7}As$	5.4	–	100	50	A1
S2	GaAs	AlAs	5.3	–	50	50	A2
B1	$In_{0.07}Ga_{0.93}As$	$Al_{0.3}Ga_{0.7}As$	4.0	4.5	100	10	A1
B2	$In_{0.07}Ga_{0.93}As$	$Al_{0.3}Ga_{0.7}As$	4.0	4.0	100	10	A1
B3	$In_{0.07}Ga_{0.93}As$	$Al_{0.3}Ga_{0.7}As$	4.0	3.6	100	10	A1
B4	$In_{0.13}Ga_{0.87}As$	$Al_{0.3}Ga_{0.7}As$	3.5	3.5	100	10	A1
C1	GaAs	$Al_{0.3}Ga_{0.7}As$	5.2	4.8	31	200	A3
C2	GaAs	$Al_{0.3}Ga_{0.7}As$	5.2	6.9	31	200	A3
C3	GaAs	$Al_{0.3}Ga_{0.7}As$	5.2	10	31	200	A3
D1	GaAs	$Al_{0.3}Ga_{0.7}As$	9.8	11.6	200	20	A3
D2	GaAs	$Al_{0.3}Ga_{0.7}As$	6.0	6.4	100	50	A1
D3	GaAs	$Al_{0.3}Ga_{0.7}As$	5.2	5.3	31	200	A3
D4	GaAs	$Al_{0.3}Ga_{0.7}As$	5.2	4.9	31	200	A3
E1	GaAs	$Al_{0.3}Ga_{0.7}As$	5.4	–	100	50	–
E2	GaAs	$Al_{0.3}Ga_{0.7}As$	5.4	5.0	100	50	A1
E3	GaAs	$Al_{0.3}Ga_{0.7}As$	5.4	6.0	100	50	A1
E4	GaAs	$Al_{0.3}Ga_{0.7}As$	5.4	7.6	100	50	A1

Table A.1: Sample list studied in the present work. We denoted the well thickness of QW1 by a, the well thickness of QW2 by b, the barrier thickness of QW1 by c, and the number of periods of QW1 by n. Samples E2~E4 are selected from series S1.

Appendix B

Calculated energy levels in quantum wells

In the present study, the QW1 thickness a and the QW2 thickness b were determined by comparing the observed photoluminescence peak of quantum wells with the theoretical value. For this purpose, we calculated the energy level of quantum well under the effective mass approximation.

GaAs quantum wells

We summarize the material parameters used in our calculation in Table B.1 and show the calculated energy levels in GaAs quantum wells in Fig. B.1. Using the Luttinger parameters of GaAs, the heavy hole effective mass and light hole effective mass in (001) quantum wells were detemined as

$$\begin{aligned} m_{hh}^{(001)} &= \frac{m_0}{\gamma_1 - 2\gamma_2}, \\ m_{lh}^{(001)} &= \frac{m_0}{\gamma_1 + 2\gamma_2}, \end{aligned}$$

while those in (110) quantum wells were give by

$$\begin{aligned} m_{hh}^{(110)} &= \frac{m_0}{\gamma_1 - \sqrt{\gamma_2^2 + 3\gamma_3^2}}, \\ m_{lh}^{(001)} &= \frac{m_0}{\gamma_1 + \sqrt{\gamma_2^2 + 3\gamma_3^2}}, \end{aligned}$$

respectively. We used the same effective masses in $Al_{0.3}Ga_{0.7}As$ and AlAs as those in GaAs in our calculation.

Parameteres	GaAs	$Al_{0.3}Ga_{0.7}As$	AlAs
Electron effective mass	$0.067m_0$	–	–
HH effective mass in (001) QWs	$0.38m_0$	–	–
HH effective mass in (110) QWs	$0.71m_0$	–	–
Conduction band offsets (eV)	–	0.243	1.036
Valence band offsets (eV)	–	0.131	0.558
Band gap at 4K (eV)	1.519	1.893	3.113
γ_1	6.85	–	–
γ_2	2.10	–	–
γ_3	2.90	–	–

Table B.1: The material parameters of III-V semiconductors used in our calculation. The free-electron mass is represented by m_0 and Luttinger parameters are given by $\gamma_1 \sim \gamma_3$. The band gap includes exciton binding energy in the bulk.

For the band gap of GaAs and $Al_xGa_{1-x}As$, we use the experimantal equations of

$$\begin{aligned} Eg(GaAs) &= 1.519 - \frac{0.0005405T^2}{T+204}, \\ Eg(Al_xGa_{1-x}As) &= Eg(GaAs) + 1.247x, \end{aligned}$$

respectively. Then, the conduction band offset ΔE_c and the valence band offset ΔE_v are determined by

$$\begin{aligned} \Delta E_c &= 0.65\Delta E\text{g}, \\ \Delta E_v &= 0.35\Delta E\text{g}, \end{aligned}$$

where $\Delta E\text{g} = E\text{g}(AlGaAs) - E\text{g}(GaAs)$.

InGaAs quantum wells

We calculated the energy levels of $In_xGa_{1-x}As$ quantum wells under the effective mass approximation. In Fig. B.2, the energy levels in $In_{0.07}Ga_{0.93}As/Al_{0.3}Ga_{0.7}As$ quantum wells and $In_{0.13}Ga_{0.87}As/Al_{0.3}Ga_{0.7}As$ quantum wells were plotted as a function of well thickness.

The electron effective mass m_e and the heavy hole effective mass m_{hh} were given by

$$\begin{aligned} m_e &= 0.0665 - 0.044x, \\ m_{hh} &= 0.45 - 0.07x, \end{aligned}$$

which were used for the calculation in (110) quantum well as well as in (001) quantum wells. The band gap of $In_xGa_{1-x}As$ was determined as

$$Eg(In_xGa_{1-x}As) = Eg(GaAs) - 1.5837x + 0.475x^2.$$

Then, the conduction band offset ΔE_c and the valence band offset ΔE_v are determined by

$$\begin{aligned} \Delta E_c &= 0.7\Delta Eg, \\ \Delta E_v &= 0.3\Delta Eg, \end{aligned}$$

where $\Delta Eg = Eg(AlGaAs) - Eg(InGaAs)$.

Bibliography

1. *Physics of Group IV Elements and III-V Compounds*, edited by O. Madelung, M. Schulz, and H. Weiss, Landort-Börnstein Numerical Data and Relationships, New Series, Group III, Vol. 17a (Springer, Berlin, 1982).

2. S. Adachi, J. Appl. Phys. **58**, R1 (1985).

3. S. H. Pan, H. Shen, Z. Hang, F. H. Pollak, W. Zhuang, Q. Xu, A. P. Roth, R. A. Masut, C. Lacelle, and D. Morris, Phys. Rev. B**38**, 3375 (1988).

4. G. Arnaud, J. Allegre, P. Lefebvre, H. Mathieu, L. K. Howard, D. J. Dunstan, Phys. Rev. B**46**, 15290 (1992).

5. J. Leymarie, C. Monier, A. Vasson, A.-M. Vasson, M. Leroux, B. Courboules, N. Grandjean, C. Deparis, and J. Massies, Phys. Rev. B**51**, 13274 (1995).

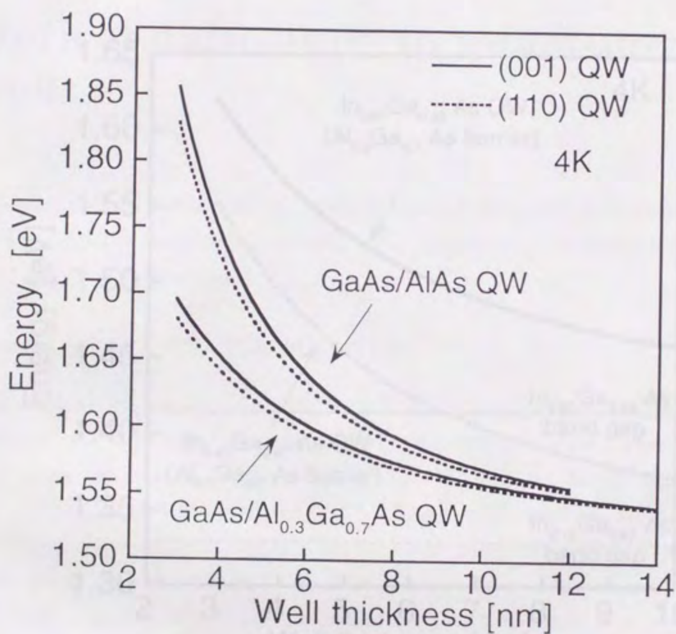

Figure B.1: The energy levels of GaAs quantum wells calculated under the effective mass approximation. The barrier layers are of $Al_{0.3}Ga_{0.7}As$ or AlAs.

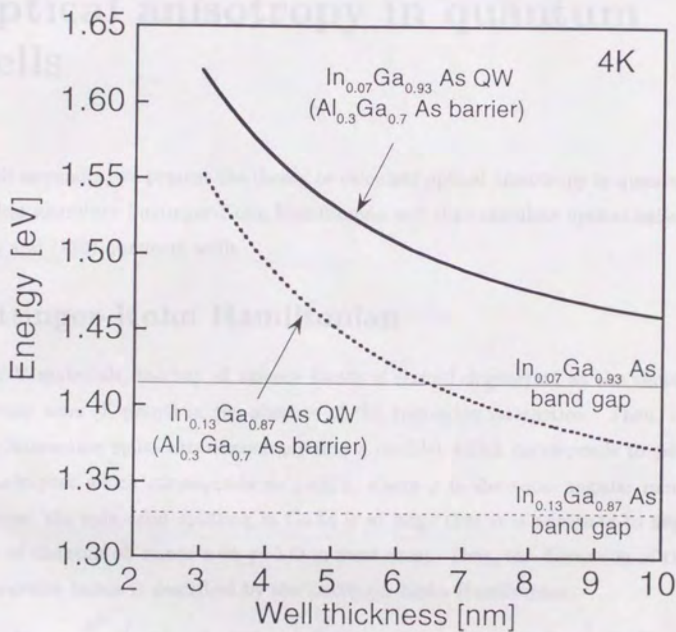

Figure B.2: The energy levels of InGaAs quantum wells calculated under the effective mass approximation. The barrier layers are of $Al_{0.3}Ga_{0.7}As$.

Appendix C

Optical anisotropy in quantum wells

In this appendix, we present the theory to calculate optical anisotropy in quantum wells. We first introduce Luttinger-Kohn Hamiltonian and then calculate optical anisotropy in (001) and (110) quantum wells.

Luttinger-Kohn Hamiltonian

In III-V materials, the top of valence bands is sixfold degenerate at the center of the Brillouin zone (Γ point) in the absence of the spin-orbit interaction. Then, the spin-orbit interaction splits this degeneracy into a doublet which corresponds to j=1/2 and a quadrupret which corresponds to j=3/2, where j is the total angular momentum. However, the spin-orbit splitting in GaAs is so large that it is adequate to neglect the effect of the spin-off bands with j=1/2 in most cases. Thus, the dispersion of the upper four valence bands is described by the Luttinger-Kohn Hamiltonian;

$$H = -\frac{\hbar^2}{2m_0}\left\{\gamma_1 k^2 - 2\gamma_2[(J_x^2 - \frac{1}{3}J^2)k_x^2 + (J_y^2 - \frac{1}{3}J^2)k_y^2 + (J_z^2 - \frac{1}{3}J^2)k_z^2] \right.$$
$$\left. -4\gamma_3[\{J_xJ_y\}\{k_xk_y\} + \{J_yJ_z\}\{k_yk_z\} + \{J_zJ_x\}\{k_zk_x\}]\right\}, \quad \text{(C.1)}$$

where m_0 is the free electron mass, coefficients γ_1, γ_2, and γ_3 are Luttinger parameters,

$$k^2 = k_x^2 + k_y^2 + k_z^2, \quad \text{(C.2)}$$

$$J^2 = J_x^2 + J_y^2 + J_z^2, \quad \text{(C.3)}$$

$$\{J_xJ_y\} = J_xJ_y - J_yJ_x. \quad \text{(C.4)}$$

(001) quantum wells

We choose such coodinates as $x//[100]$, $y//[010]$, and $z//[001]$. Then, we express J_x, J_y, and J_z for the total angular momentum j=3/2 in the matrix formulation as

$$J_x = \begin{bmatrix} 0 & i\sqrt{3}/2 & 0 & 0 \\ -i\sqrt{3}/2 & 0 & i & 0 \\ 0 & -i & 0 & i\sqrt{3}/2 \\ 0 & 0 & -i\sqrt{3}/2 & 0 \end{bmatrix}, \tag{C.5}$$

$$J_y = \begin{bmatrix} 0 & \sqrt{3}/2 & 0 & 0 \\ \sqrt{3}/2 & 0 & 1 & 0 \\ 0 & 1 & 0 & \sqrt{3}/2 \\ 0 & 0 & \sqrt{3}/2 & 0 \end{bmatrix}, \tag{C.6}$$

$$J_z = \begin{bmatrix} 3/2 & 0 & 0 & 0 \\ 0 & 1/2 & 0 & 0 \\ 0 & 0 & -1/2 & 0 \\ 0 & 0 & 0 & -3/2 \end{bmatrix}, \tag{C.7}$$

where bases $|j, m_j\rangle$ for j=3/2 are taken as

$$|\frac{3}{2}, +\frac{3}{2}\rangle = -\frac{1}{\sqrt{2}}|(X+iY)\uparrow\rangle, \tag{C.8}$$

$$|\frac{3}{2}, +\frac{1}{2}\rangle = -\frac{1}{\sqrt{6}}|(X+iY)\downarrow\rangle + \sqrt{\frac{2}{3}}|Z\uparrow\rangle, \tag{C.9}$$

$$|\frac{3}{2}, -\frac{1}{2}\rangle = \frac{1}{\sqrt{6}}|(X-iY)\uparrow\rangle + \sqrt{\frac{2}{3}}|Z\downarrow\rangle, \tag{C.10}$$

$$|\frac{3}{2}, -\frac{3}{2}\rangle = \frac{1}{\sqrt{2}}|(X-iY)\downarrow\rangle. \tag{C.11}$$

In such a case, Luttinger-Kohn Hamiltonian is expressed as

$$H = \begin{bmatrix} \frac{1}{2}P & L & M & 0 \\ L^* & \frac{1}{6}P + \frac{2}{3}Q & 0 & M \\ M^* & 0 & \frac{1}{6}P + \frac{2}{3}Q & -L \\ 0 & M^* & -L^* & \frac{1}{2}P \end{bmatrix}, \tag{C.12}$$

where

$$P = \frac{\hbar^2}{m}[(\gamma_1+\gamma_2)(k_x^2+k_y^2) + (\gamma_1 - 2\gamma_2)k_z^2], \tag{C.13}$$

$$Q = \frac{\hbar^2}{2m}[(\gamma_1-2\gamma_2)(k_x^2+k_y^2) + (\gamma_1 + 4\gamma_2)k_z^2], \tag{C.14}$$

$$L = -\frac{\sqrt{3}\hbar^2}{2m}\gamma_3(k_x - ik_y)k_z, \tag{C.15}$$

$$M = -\frac{\sqrt{3}\hbar^2}{2m}[\gamma_2(k_x^2-k_y^2) - 2i\gamma_3 k_x k_y]. \tag{C.16}$$

Setting $k_x = k_y = 0$ and $k_z = -i\frac{d}{dz}$, the effective mass equation at the center of the Brillouin zone is written as

$$-\frac{\hbar^2}{2m_0}\begin{bmatrix} \gamma_1 - 2\gamma_2 & 0 & 0 & 0 \\ 0 & \gamma_1 + 2\gamma_2 & 0 & 0 \\ 0 & 0 & \gamma_1 + 2\gamma_2 & 0 \\ 0 & 0 & 0 & \gamma_1 - 2\gamma_2 \end{bmatrix}\frac{d^2}{dz^2}\phi = E\phi. \tag{C.17}$$

The eigenfunctions $|hh^{\pm}_{(001)}\rangle$ and $|lh^{\pm}_{(001)}\rangle$ of Eq. C.16 are given by

$$|hh^{\pm}_{(001)}\rangle = |\frac{3}{2}, \pm\frac{3}{2}\rangle, \tag{C.18}$$

$$|lh^{\pm}_{(001)}\rangle = |\frac{3}{2}, \pm\frac{1}{2}\rangle. \tag{C.19}$$

The squared optical matrix elements for transition between the conduction band and the valence band takes the form

$$|M|^2 = |\langle s|\boldsymbol{e}\cdot\boldsymbol{p}|hh\rangle|^2, \tag{C.20}$$

$$|M|^2 = |\langle s|\boldsymbol{e}\cdot\boldsymbol{p}|lh\rangle|^2. \tag{C.21}$$

Using such relations as

$$\langle s|p_x|X\rangle = \langle s|p_y|Y\rangle = \langle s|p_z|Z\rangle = P, \tag{C.22}$$

$$P = \sqrt{3}|M_b|, \tag{C.23}$$

where $|M_b|$ is the optical matrix elements in bulk, we obtained $|M|^2$ for (001) quantum wells as shown in Table C.1.

(110) quantum wells

We change coodinates from the old ones $x//[100]$, $y//[010]$, and $z//[001]$ to the new ones $a//[\bar{1}10]$, $b//[001]$, and $c//[110]$. In such a transformation, the wavevector k and the angular momentum J are given by

$$k_x = -\frac{1}{\sqrt{2}}k_a + \frac{1}{\sqrt{2}}k_c, \tag{C.24}$$

$$k_y = \frac{1}{\sqrt{2}}k_a + \frac{1}{\sqrt{2}}k_c, \tag{C.25}$$

$$k_z = -k_b, \tag{C.26}$$

$$J_x = -\frac{1}{\sqrt{2}}J_a + \frac{1}{\sqrt{2}}J_c, \tag{C.27}$$

$$J_y = \frac{1}{\sqrt{2}}J_a + \frac{1}{\sqrt{2}}J_c, \tag{C.28}$$

$$J_z = -J_b, \tag{C.29}$$

where we use new matrix J_a, J_b, and J_c such as

$$J_a = \begin{bmatrix} 0 & i\sqrt{3}/2 & 0 & 0 \\ -i\sqrt{3}/2 & 0 & i & 0 \\ 0 & -i & 0 & i\sqrt{3}/2 \\ 0 & 0 & -i\sqrt{3}/2 & 0 \end{bmatrix}, \tag{C.30}$$

$$J_b = \begin{bmatrix} 0 & \sqrt{3}/2 & 0 & 0 \\ \sqrt{3}/2 & 0 & 1 & 0 \\ 0 & 1 & 0 & \sqrt{3}/2 \\ 0 & 0 & \sqrt{3}/2 & 0 \end{bmatrix}, \tag{C.31}$$

$$J_c = \begin{bmatrix} 3/2 & 0 & 0 & 0 \\ 0 & 1/2 & 0 & 0 \\ 0 & 0 & -1/2 & 0 \\ 0 & 0 & 0 & -3/2 \end{bmatrix}. \tag{C.32}$$

Then, we obtained Luttinger-Kohn Hamiltonian in the matrix formulation;

$$H = -\frac{\hbar^2}{2m}\begin{bmatrix} R & S & T & 0 \\ S^* & -R & 0 & -T \\ T^* & 0 & -R & S \\ 0 & -T^* & S^* & R \end{bmatrix}, \tag{C.33}$$

where

$$R = \gamma_1 k^2 + \left(\frac{1}{4}\gamma_2 + \frac{3}{4}\gamma_3\right)(k_+k_- + 2k_z^2) + \frac{3}{8}(\gamma_3 - \gamma_2)(k_+^2 + k_-^2), \tag{C.34}$$

$$S = \sqrt{3}[(\gamma_2 + \gamma_3)k_+ + (\gamma_2 - \gamma_3)k_-]k_z, \tag{C.35}$$

$$T = \frac{\sqrt{3}}{4}\left[(\gamma_2 - \gamma_3)(k_+k_- + 2k_z^2) - \left(\frac{3}{2}\gamma_2 + \frac{1}{2}\gamma_3\right)(k_+^2 + k_-^2) + 2\gamma_3(k_+^2 - k_-^2)\right], \tag{C.36}$$

$$k^2 = k_x^2 + k_y^2 + k_z^2, \tag{C.37}$$

$$k_\pm = k_x \pm ik_y. \tag{C.38}$$

Setting $k_a = k_b = 0$ and $k_c = -i\frac{d}{dc}$, the effective mass equation at the center of the Brillouin zone is given by

$$-\frac{\hbar^2}{2m_0}\begin{bmatrix} \gamma_1-\frac{1}{2}\gamma_2-\frac{3}{2}\gamma_3 & 0 & -\frac{\sqrt{3}}{2}(\gamma_2-\gamma_3) & 0 \\ 0 & \gamma_1+\frac{1}{2}\gamma_2+\frac{3}{2}\gamma_3 & 0 & -\frac{\sqrt{3}}{2}(\gamma_2-\gamma_3) \\ -\frac{\sqrt{3}}{2}(\gamma_2-\gamma_3) & 0 & \gamma_1+\frac{1}{2}\gamma_2+\frac{3}{2}\gamma_3 & 0 \\ 0 & -\frac{\sqrt{3}}{2}(\gamma_2-\gamma_3) & 0 & \gamma_1-\frac{1}{2}\gamma_2-\frac{3}{2}\gamma_3 \end{bmatrix}\frac{d^2}{dc^2}\phi = E\phi. \tag{C.39}$$

The eigenfunctions $|hh^{\pm}_{(110)}\rangle$ and $|lh^{\pm}_{(110)}\rangle$ of Eq. C.38 are written as

$$|hh^{\pm}_{(110)}\rangle = \frac{1}{\sqrt{2}}\sqrt{1+\frac{\frac{1}{2}\gamma_2+\frac{3}{2}\gamma_3}{\sqrt{\gamma_2^2+3\gamma_3^2}}}|\frac{3}{2},\mp\frac{3}{2}\rangle - \frac{1}{\sqrt{2}}\sqrt{1-\frac{\frac{1}{2}\gamma_2+\frac{3}{2}\gamma_3}{\sqrt{\gamma_2^2+3\gamma_3^2}}}|\frac{3}{2},\pm\frac{1}{2}\rangle, \tag{C.40}$$

$$= \pm\sqrt{\frac{1}{3}\left(1-\frac{\frac{1}{2}\gamma_2-\frac{3}{2}\gamma_3}{\sqrt{\gamma_2^2+3\gamma_3^2}}\right)}|A\rangle \pm \sqrt{\frac{1}{3}\left(1+\frac{\gamma_2}{\sqrt{\gamma_2^2+3\gamma_3^2}}\right)}|B\rangle \tag{C.41}$$

$$\pm\sqrt{\frac{1}{3}\left(1-\frac{\frac{1}{2}\gamma_2+\frac{3}{2}\gamma_3}{\sqrt{\gamma_2^2+3\gamma_3^2}}\right)}|C\rangle,$$

$$|lh^{\pm}_{(110)}\rangle = \frac{1}{\sqrt{2}}\sqrt{1-\frac{\frac{1}{2}\gamma_2+\frac{3}{2}\gamma_3}{\gamma_2^2+3\gamma_3^2}}|\frac{3}{2},\mp\frac{3}{2}\rangle - \frac{1}{\sqrt{2}}\sqrt{1+\frac{\frac{1}{2}\gamma_2+\frac{3}{2}\gamma_3}{\gamma_2^2+3\gamma_3^2}}|\frac{3}{2},\pm\frac{1}{2}\rangle, \tag{C.42}$$

$$= \pm\sqrt{\frac{1}{3}\left(1+\frac{\frac{1}{2}\gamma_2-\frac{3}{2}\gamma_3}{\sqrt{\gamma_2^2+3\gamma_3^2}}\right)}|A\rangle \pm \sqrt{\frac{1}{3}\left(1-\frac{\gamma_2}{\sqrt{\gamma_2^2+3\gamma_3^2}}\right)}|B\rangle \tag{C.43}$$

$$\pm\sqrt{\frac{1}{3}\left(1+\frac{\frac{1}{2}\gamma_2+\frac{3}{2}\gamma_3}{\sqrt{\gamma_2^2+3\gamma_3^2}}\right)}|C\rangle.$$

As a reuslt, we obtained $|M|^2$ for (110) quantum wells as shown in Table C.1.

	(001) QW		(110) QW	
	HH	LH	HH	LH
$\frac{\lvert M_{[\bar{1}10]}\rvert^2}{\lvert M_b\rvert^2}$	1.5	0.5	1.606	0.394
$\frac{\lvert M_{[110]}\rvert^2}{\lvert M_b\rvert^2}$	1.5	0.5	0.08	1.992
$\frac{\lvert M_{[001]}\rvert^2}{\lvert M_b\rvert^2}$	0	2	1.386	0.614

Table C.1: Squared optical matrix elements for (001) and (110) quantum wells.

Bibliography

1. L. I. Schiff, *Quantum Mechanics* (McGraw-Hill International Editions, New York, 1968).
2. G. Bastard, *Wave Mechanics Applied to Semiconductor Heterostructures* (Halsted Press, New York, 1988).
3. Y. Kajikawa, Thesis (in Japanese) (1996).
4. J. M. Luttinger and W. Kohn, Phys. Rev. B**97**, 869 (1955).

Appendix D

Effective mass equation under a magnetic field

In this appendix, we first present an effective mass equation of excitons under a magnetic field and, then, calculate the effective areas of excitons and diamagnetic coefficients β in several typical cases.

Theoretical formula

The effective mass equation of excitons is written as

$$\left[\frac{1}{2m_e}\{\boldsymbol{p}_e + e\boldsymbol{A}(\boldsymbol{r}_e)\}^2 + \frac{1}{2m_h}\{\boldsymbol{p}_h - e\boldsymbol{A}(\boldsymbol{r}_h)\}^2 - \frac{e^2}{\varepsilon|\boldsymbol{r}_e - \boldsymbol{r}_h|} + V_e(\boldsymbol{r}_e) + V_h(\boldsymbol{r}_h)\right]\psi = \varepsilon\psi, \tag{D.1}$$

where $\boldsymbol{r}_e$ and $\boldsymbol{r}_h$ are the coodinates of electrons and holes, respectively, $\boldsymbol{p}$ is the momentum operator, $\boldsymbol{A}$ is the vector potential, V is the confinement potential, ε is the static dielectric constant, and e (> 0) is the electron charge. First, we transform Eq. D.1 to the relative coordinates $\boldsymbol{r}$ and center-of-mass coordinates $\boldsymbol{R}$, using

$$\boldsymbol{r} = \boldsymbol{r}_e - \boldsymbol{r}_h \tag{D.2}$$

and

$$\boldsymbol{R} = \frac{m_e\boldsymbol{r}_e - m_h\boldsymbol{r}_h}{m_e + m_h}, \tag{D.3}$$

respectively. Second, we choose the wave functions as

$$\psi(\boldsymbol{R}, \boldsymbol{r}) = \exp\left\{i\left[\boldsymbol{K} + \frac{e}{\hbar}\boldsymbol{A}(\boldsymbol{r})\right]\cdot\boldsymbol{R}\right\}\phi. \tag{D.4}$$

Then, taking the vector potential as

$$A(r) = \frac{1}{2} B_0 \times r, \tag{D.5}$$

inserting Eqs. D.2 - D.5 into Eq. D.1 yields

$$\begin{aligned}\left[-\frac{\hbar^2}{2\mu}\nabla^2 - \frac{e^2}{\varepsilon r} - \frac{e}{2}\left(\frac{1}{m_e} - \frac{1}{m_h}\right) B_0 \cdot L \right. &+ \left. \frac{e^2(x^2+y^2)}{8\mu} B_0^2 - \left\{\frac{\hbar K}{m_e + m_h} \times B_0\right\} \cdot r \right] \phi \\ &= \left[E - \frac{\hbar^2 K^2}{2(m_e + m_h)}\right] \phi, \end{aligned} \tag{D.6}$$

where $\mu = (1/m_e - 1/m_h)^{-1}$ is the exciton reduced mass and $L = r \times (\hbar/i)\nabla$ is the angular momentum operator.

The third term of the Hamiltonian in Eq. D.6 represnts the Zeeman effect. The forth term is so called the diamagnetic term, which is expressed as βB_0^2 with diamagnetic coefficient β being equal to

$$\beta = \frac{e^2 \langle x^2 + y^2 \rangle}{8\mu}. \tag{D.7}$$

In the following, we will calculate the diamagnetic coefficients β or effective areas $\langle x^2 + y^2 \rangle$ in the several typical cases.

The bulk case

In the bulk material without confinement potential, the wave function is obtained by solving

$$\left[-\frac{\hbar^2}{2\mu}\nabla^2 - \frac{e^2}{\varepsilon r}\right] \phi(r) = E\phi(r), \tag{D.8}$$

which is refered to as the Wannier equation; it is the Schrödinger equation for excitonic envelope function describing the relative motion of the electron-hole pairs. For an $n = 1$ exciton, the eigenfunction is given by

$$\phi_{1s}(r) = \frac{1}{\sqrt{\pi a_B^3}} e^{-r/a_B}, \tag{D.9}$$

where

$$a_B = \frac{\varepsilon \hbar^2}{\mu e^2} \tag{D.10}$$

is the exciton Bohr radius. In GaAs, the exciton Bohr radius a_B is 12 nm, if the following matarial parameters are used; m_e=0.067m_0, m_h=0.38m_0, and ε=13.1ε_0. Then, using ϕ_{1s}, the effective area of excitons is given as

$$\begin{aligned}&\langle x^2+y^2\rangle\\&= \int r^2 \sin^2\theta \left[\frac{1}{\sqrt{\pi a_B^3}} e^{-r/a_B}\right]^2 \sin^2\theta dr d\varphi d\theta\\&= 2a_B^2.\end{aligned} \tag{D.11}$$

Thus, the diamagnetic coefficient of excitons in bulk becomes

$$\beta = \frac{e^2 a_B^2}{4\mu}, \tag{D.12}$$

which is 107 μeV/T^2 in GaAs.

The thin limit of quantum wells

We will study two-dimenaional excitons confined in quantum wells. In the thin limit of well width ($L_w \sim 0$), the envelop functions of excitons are eigenfunctions of the following Schrödinger equation;

$$\left[-\frac{\hbar^2}{2\mu}\left(\frac{\partial^2}{\partial x^2}+\frac{\partial^2}{\partial y^2}\right) - \frac{e^2}{\varepsilon\sqrt{x^2+y^2}}\right]\phi = E\phi. \tag{D.13}$$

The wave function in the ground state of excitons is given by

$$\phi_{00} = \sqrt{\frac{8}{\pi a_B^2}} \exp\left(-\frac{2r}{a_B}\right). \tag{D.14}$$

Then, using ϕ_{00}, the effective area of excitons is given by

$$\begin{aligned}&\langle x^2+y^2\rangle\\&= \int r^2 \left[\sqrt{\frac{8}{\pi a_B^2}} \exp\left(-\frac{2r}{a_B}\right)\right]^2 dr d\theta\\&= \frac{3}{8}a_B^2.\end{aligned} \tag{D.15}$$

Thus, the diamagnetic coefficient of two-dimensional excitons in the thin limit of well width becomes

$$\beta = \frac{3}{16}\left(\frac{e^2 a_B^2}{4\mu}\right), \tag{D.16}$$

which is 20 μeV/T^2 in GaAs quantum wells.

Quantum wells with finite width

We have studied on two-dimensional excitons confined in quantum wells in the thin limit of well width ($L_w \sim 0$), where the wave functions are analytically obtained. Next, we will consider excitons in quantum wells whose well width L is not zero but finite. Here, we assume the exciton wave function of

$$\phi = N \cos\frac{\pi z_e}{L} \cos\frac{\pi z_h}{L} \exp\left(-\frac{x^2+y^2}{\lambda}\right), \tag{D.17}$$

where N is the normalization constant and λ is the trial parameter. Using such a wave function, the effective areas of excitons are given by

$$\begin{aligned} \langle x^2+y^2\rangle &= \frac{3}{2}\lambda^2, & \text{(D.18)}\\ \langle y^2+z^2\rangle &= \frac{3}{4}\lambda^2 + \left(\frac{1}{6}-\frac{1}{\pi^2}\right)L^2, & \text{(D.19)}\\ \langle z^2+x^2\rangle &= \frac{3}{4}\lambda^2 + \left(\frac{1}{6}-\frac{1}{\pi^2}\right)L^2. & \text{(D.20)} \end{aligned}$$

Square quantum wires

If one considers square quantum wires whose cross sectional dimensions are L_x by L_y with infinite barriers, it is adequate to assume the exciton wave function of

$$\phi = N \cos\frac{\pi z_e}{L_x} \cos\frac{\pi z_h}{L_x} \cos\frac{\pi z_e}{L_y} \cos\frac{\pi z_h}{L_y} \exp\left(-\frac{|r|}{\kappa}\right), \tag{D.21}$$

where N is the normalization constant and κ is the trial parameter. Then, we obtain the effective areas of excitons as

$$\begin{aligned} \langle x^2+y^2\rangle &= \left(\frac{1}{6}-\frac{1}{\pi^2}\right)(L_x^2+L_y^2), & \text{(D.22)}\\ \langle y^2+z^2\rangle &= \left(\frac{1}{6}-\frac{1}{\pi^2}\right)L_x^2 + \frac{1}{2}\kappa^2, & \text{(D.23)}\\ \langle z^2+x^2\rangle &= \left(\frac{1}{6}-\frac{1}{\pi^2}\right)L_y^2 + \frac{1}{2}\kappa^2. & \text{(D.24)} \end{aligned}$$

Bibliography

1. J. O. Dimmock, *Semiconductors and Semimetals* (Academic Press, New York, 1967).

2. R. S. Knox, *Theory of Excitons* (Academic Press, New York, 1963).

Publication List

1. Publications related to this work

1. T. Someya, H. Akiyama, and H. Sakaki, "Laterally squeezed excitonic wave function in quantum wires", Physical Review Letters. 74, 3664-3667 (1995).

2. T. Someya, H. Akiyama, M. Yamauchi, H. Sugawara, and H. Sakaki, "Effect of lateral confinement on excitonic wavefunction in edge quantum wires", Solid State Electronics 42, 245-249 (1995).

3. T. Someya, H. Akiyama, and H. Sakaki, "Tightly-confined one-dimensional states in T-shaped edge quantum wires", Applied Physics Letters 66, 3672-3673 (1995).

4. T. Someya, H. Akiyama, and H. Sakaki, "Laterally squeezed excitonic wavefunction in T-shaped GaAs edge quantum wires", Technical Digest of Quantum Electronics and Laser Science, The OSA Technical Digest Series, 30-31 (1995).

5. T. Someya, H. Akiyama, and H. Sakaki, "Spatially resolved photoluminescence study on T-shaped quantum wires fabricated by cleaved edge overgrowth method", Journal of Applied Physics 79, 2522-2528 (1996).

6. T. Someya, H. Akiyama, and H. Sakaki, "Enhanced binding energy of one-dimensional excitons in quantum wires", Physical Review Letters 76, 2965-2968 (1996).

7. H. Akiyama, T. Someya, and H. Sakaki, "Optical anisotropy in 5-nm-scale T-shaped GaAs quantum wires fabricated by cleaved edge overgrowth method", Physical Review B53, R4229-R4232 (1996).

8. H. Akiyama, T. Someya, and H. Sakaki, "Microscopic photoluminescence spectroscopy of 5-nm-scale T-shaped quantum wires fabricated by cleaved edge overgrowth method", Technical Digest of International Quantum Electronics Conference, Technical Digest Series 9 (1996).

9. H. Akiyama, T. Someya, and H. Sakaki, "Dimensional crossover and confinement-induced optical anisotropy in GaAs T-shaped quantum wires", Physical Review B53, 10520-10523 (1996).

10. T. Someya, H. Akiyama, and H. Sakaki, "Molecular beam epitaxial growth of $In_{0.15}Ga_{0.85}As$ quantum wells on GaAs (110) surfaces", Japanese Journal of Applied Physics 35, 2544-2547 (1996).

11. T. Someya, H. Akiyama, and H. Sakaki, "Enhancement of binding energy and lateral confinement of one-dimensional excitons in 5-nm-scale T-shaped quantum wires ", Proceedings of 23rd International Conference on the Physics of Semiconductors, edited by D. Bimberg et al. (World Scientific Publishing, Singapore, 1996), 1165-1168.

12. H. Akiyama, T. Someya, and H. Sakaki, "Concentrated oscillator strength of one-dimensional excitons in quantum wires observed with photoluminescence excitation spectroscopy", Physical Review B53, R16160-R16163 (1996).

2. Other publications

1. T. Someya, H. Akiyama, Y. Kadoya, T. Noda, T. Matsusue, H. Noge, and H. Sakaki, "Detection of oxygen incorporated in MBE-grown GaAs-on-AlAs interfaces and AlAs layers by secondary ion mass spectrometry", Applied Physics Letters 63, 1924-1926 (1993).

2. T. Someya, H. Akiyama, Y. Kadoya, H. Noge, and H. Sakaki, "Oxygen incorporation at GaAs/AlGaAs interfaces grown by molecular beam epitaxy", Proceedings of 1st International Symposium on Control of Semiconductor Interfaces, edited by I. Ohdomari et al. (Elsevier Sciences, Switzerland, 1993) 93-96.

3. Y. Kadoya, T. Yoshida, T. Someya, H. Akiyama, H. Noge, and H. Sakaki, "Etching of InAs in HCl gas and selective removal of InAs layer on GaAs in ultrahigh-vacuum processing system", Japanese Journal of Applied Physics 32, L1496-L1499 (1993).

4. H. Akiyama, T. Someya, H. Sakaki, S. Koshiba, H. Noge, T. Inoshita, Y. Nakamura, and A. Shimizu, "Thermalization effect in radiative decay of 1D excitons in ridge quantum wires", Technical Digest of Quantum Electronics and Laser Science, the OSA Technical Digest Series 17, 20-21 (1993).

5. T. Someya, H. Akiyama, Y. Kadoya, and H. Sakaki, "Quantitative study of oxygen incorporation on MBE-grown AlAs surfaces and its effect on nonradiative recombination in GaAs/AlAs quantum wells", International Conference Series No. 136, edited by G. Weimann et al. (IOP Publishing, Bristol and Philadelphia, 1994) 517-522.

6. S. Koshiba, H. Noge, Y. Nakamura, H. Akiyama, T. Inoshita, T. Someya, A. Shimizu, and H. Sakaki, "MBE growth of GaAs nanometer-scale ridge quantum wire structures and their structural and optical characterizations", Solid State Electronics 37, 729-732 (1994).

7. H. Akiyama, S. Koshiba, T. Someya, K. Wada, H. Noge, Y. Nakamura, T. Inoshita, A. Shimizu, and H. Sakaki, "Thermalization effect on radiative decay of excitons in ridge quantum wires", Physical Review Letters 72, 924-927 (1994).

8. Y. Ohno, Y. Nakamura, M. Foley, T. Someya, T. Noda, and H. Sakaki, "Magnetoresistance oscillations in 50-nm-wide GaAs/AlGaAs multi-edge quantum wires", Physical Review B 52, 11619-11622 (1995).

9. H. Noge, Y. Nakamura, S. Koshiba, Y. Kadoya, T. Someya, Y. Ohno, R. Hull, and H. Sakaki, "Selective epitaxy for ridge and edge quantum wire structures: morphology and purity issues", NATO ASI Series 298, edited by K. Eberl et al. (Kluwer Academic Publishers, 1995) 271-282.

10. G. Yusa, H. Noge, Y. Kadoya, T. Someya, P. Petroff, and H. Sakaki, "Fabrication of 10-nanometer-scale GaAs dot structures by in-situ selective gas etching with self-assembling InAs dot as mask", Japanese Journal of Applied Physics 34, L1198-L1201 (1995).

11. H. Sakaki, G. Yusa, T. Someya, Y. Ohno, T. Noda, H. Akiyama, Y. Kadoya, and H. Noge, "Transport properties of two-dimensional electron gas in AlGaAs/GaAs selectively doped heterojunctions with embedded InAs quantum dots", Applied Physics Letters 67, 3444-3446 (1995).

12. G. Yusa, H. Noge, Y. Kadoya, T. Someya, T. Suga, P. Petroff, and H. Sakaki, "10-nanometer-scale GaAs dot structures fabricated using in-situ gas etching technique with InAs dots as mask", International Conference Series, Proceedings of 22nd International Symposium on Compounds Semiconductors (IOP Publishing, Bristol and Philadelphia, 1996) 955-960.

13. S. Koshiba, I. Tanaka, Y. Nakamura, I. Kamiya, T. Someya, T. Ngo, and H. Sakaki, "UHV-AFM study of MBE-grown 10-nm-scale ridge quantum wires", Proceedings of International Conference on Molecular Beam Epitaxy (1996).

3. Presentations related to this work

1. T. Someya, H. Akiyama, and H. Sakaki, "Effect of lateral confinement on excitonic wave-function in edge quantum wires", 7th International Conference on Modulated Semiconductor Structures, Madrid (Spain), July 1995.

2. T. Someya, H. Akiyama, and H. Sakaki, "Laterally squeezed excitonic wavefunction in T-shaped GaAs edge quantum wires", Quantum Electronics and Laser Science, Baltimore (USA), May 1995.

3. H. Akiyama, T. Someya, and H. Sakaki, "Optical characterization of 1D excitons in cleaved edge overgrowth T-shaped quantum wires", 3rd Workshop on Optical Properties of Mesoscopic Semiconductor Structures, Utah (USA), May 1996.

4. H. Akiyama, T. Someya, and H. Sakaki, "Microscopic photoluminescence spectroscopy of 5nm-scale T-shaped quantum wires fabricated by cleaved edge overgrowth method", International Quantum Electronics Conference, Sydney (Australia), July 1996.

5. H. Sakaki and T. Someya, "Recent progresses in quantum stuructures", 9th International Conference on Superlattices, Microstructures, and Microdevices, Liége (Belgium), July 1996.

6. T. Someya, H. Akiyama, and H. Sakaki, "Enhancement of binding energy and lateral confinement of one-dimensional excitons in 5nm-scale T-shaped quantum wires ", 23rd International Conference on the Physics of Semiconductors, Berlin (Germany), July 1996.

7. T. Someya, H. Akiyama, and H. Sakaki, "One-dimensional properties of excitons confined in T-shaped quantum wires", Conference on Lasers and Electro-Optics, Chiba (Japan), July 1997.

4. Other presentations

1. H. Akiyama, T. Someya, H. Sakaki, S. Koshiba, H. Noge, T. Inoshita, Y. Nakamura, and A. Shimizu, "Thermalization effect in radiative decay of 1D excitons in ridge quantum wires", Quantum Electronics and Laser Science, Baltimore (USA), May 1993.

2. S. Koshiba, H. Noge, Y. Nakamura, H. Akiyama, T. Inoshita, T. Someya, A. Shimizu, and H. Sakaki, "MBE grown GaAs nanometer-scale structures on top of (001)-(111)B facet and their structural and optical properties", Sixth International Conference on Modulated Semiconductor Structures, Garmish-Partenkirchen (Germany), August 1993.

3. T. Someya, H. Akiyama, Y. Kadoya, and H. Sakaki, "Quantitative study of oxygen incorporation on MBE-grown AlAs surfaces and its effect on nonradiative recombination in GaAs/AlAs quantum wells", 20th International Symposium of Gallium Arsenide and Related Compounds, Freiburg (Germany), September 1993.

4. T. Someya, H. Akiyama, Y. Kadoya, H. Noge, and H. Sakaki, "Oxygen incorporation at GaAs/AlGaAs interfaces grown by molecular beam epitaxy", 1st International Symposium on Control of Semiconductor Interfaces, Karuizawa (Japan), November 1993.

5. J. Cerne, M. S. Sherwin, H. Akiyama, T. Someya, S. Koshiba, and H. Sakaki, "Anisotropic absorption of far infrared radiation by photoexcited carriers in quantum wires", The March Meeting of the American Physical Society, St. Louis (USA), March 1995.

6. Y. Ohno, Y. Nakamura, M. Foley, T. Someya, T. Noda, and H. Sakaki, "Observation of large oscillation in magnetoresistances of 50-nm-wide GaAs AlGaAs multiple edge quantum wires", The International Workshop on Mesoscopic Physics and Electronics, Tokyo (Japan), March 1995.

7. H. Noge, Y. Nakamura, S. Koshiba, Y. Kadoya, T. Someya, Y. Ohno, and H. Sakaki, "Selective epitaxy for ridge and edge quantum wire structures: morphology and purity issues", NATO Advanced Workshop, Ringberg (Germany), November 1995.

8. G. Yusa, H. Noge, Y. Kadoya, T. Someya, T. Suga, P. Petroff, and H. Sakaki, "10-nanometer-scale GaAs dot structures fabricated using in-situ gas etching technique with InAs dots as mask", 22nd International Symposium on Compounds Semiconductors, Checjun (Korea), August 1995.

9. S. Koshiba, I. Tanaka, Y. Nakamura, I. Kamiya, T. Someya, T. Ngo, and H. Sakaki, "UHV-AFM study of MBE-grown 10-nm-scale ridge quantum wires", International Conference on Molecular Beam Epitaxy, Malibu (USA), August 1996.

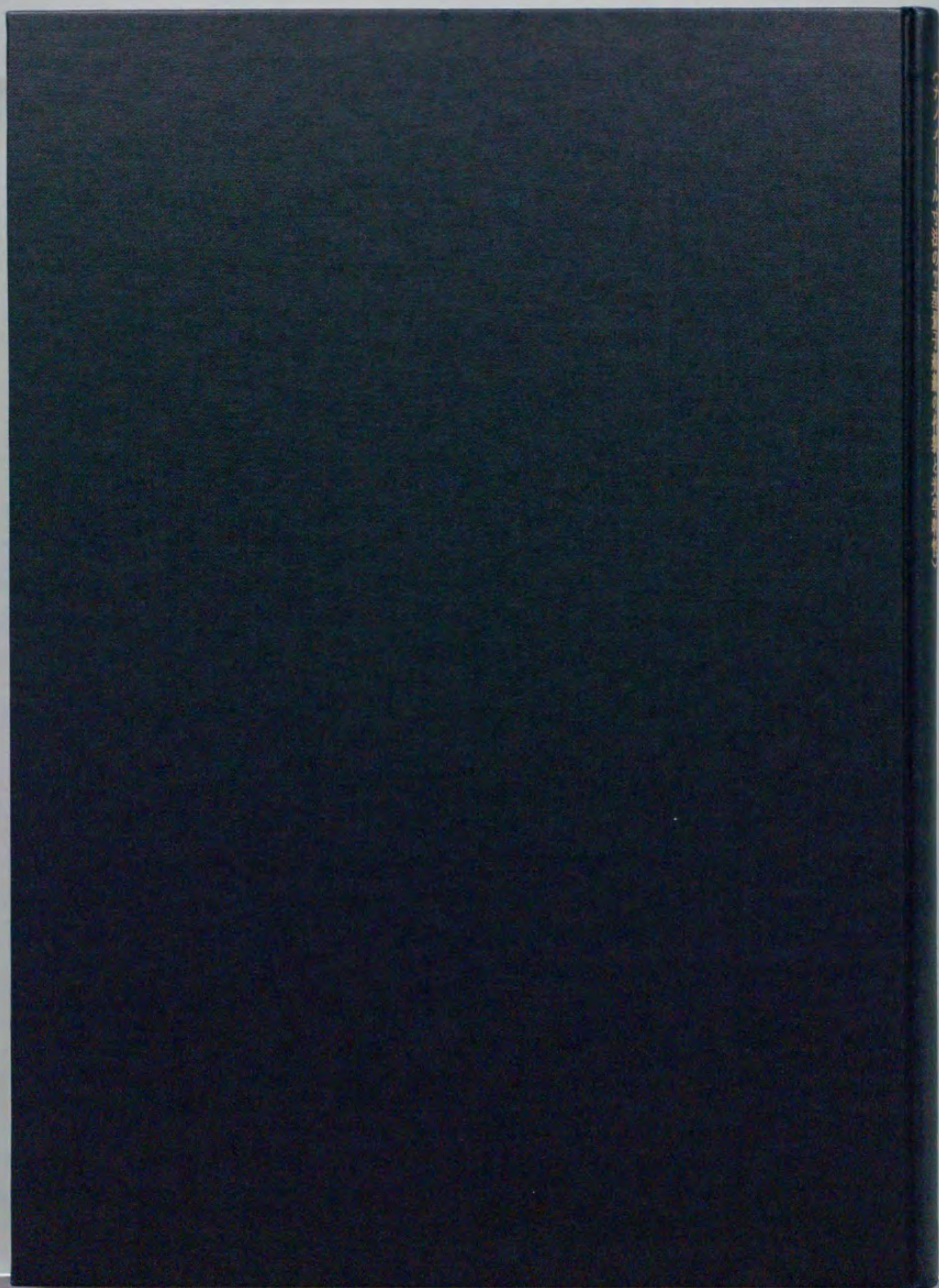

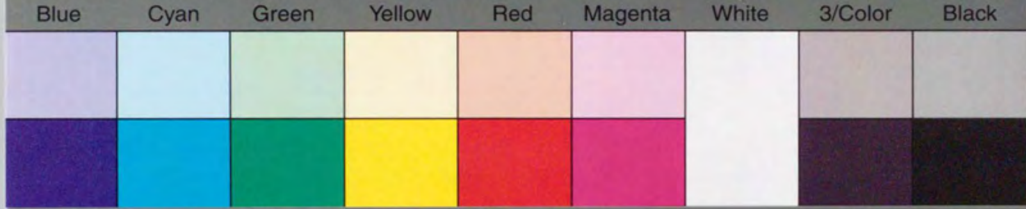
inches
cm
Kodak Color Control Patches
© Kodak, 2007 TM: Kodak
Blue Cyan Green Yellow Red Magenta White 3/Color Black

C Y M

Kodak Gray Scale
© Kodak, 2007 TM: Kodak
A 1 2 3 4 5 6 M 8 9 10 11 12 13 14 15 B 17 18 19